

Universidade de São Paulo  
Instituto de Física

Avaliação de doses em órgãos em procedimentos  
de tomografia computadorizada utilizando  
dosímetros TL e OSL

Louise Maria Giansante Martins

Orientador: Prof. Dr. Paulo Roberto Costa

Dissertação de mestrado apresentada ao Instituto  
de Física para a obtenção do título de Mestre em  
Ciências.

Banca Examinadora:

Prof. Dr. Paulo Roberto Costa (IFUSP)  
Prof. Dr. Manuel Arreola (Universidade da Flórida)  
Profa. Dra. Eloisa Gebrim (FMUSP)

São Paulo  
2017

**FICHA CATALOGRÁFICA**  
**Preparada pelo Serviço de Biblioteca e Informação**  
**do Instituto de Física da Universidade de São Paulo**

Martins, Louise Maria Giansante

Avaliação de doses em órgãos em procedimentos de tomografia computadorizada utilizando dosímetros TL e OSL / Organ doses evaluation for computed tomography procedures using TL and OSL dosimeters.

São Paulo, 2017.

Dissertação (Mestrado) – Universidade de São Paulo. Instituto de Física.  
Depto. Física Nuclear

Orientador: Prof. Dr. Paulo Roberto Costa

Área de Concentração: Física Médica

Unitermos: 1.Tomografia computadorizada por raios x; 2.Radiologia; 3.Física médica; 4. Dosimetria TL e OSL; 5. Doses em órgãos.

USP/IF/SBI-056/2017

University of São Paulo  
Institute of Physics

# Organ doses evaluation for computed tomography procedures using TL and OSL dosimeters

Louise Maria Giansante Martins

Supervisor: Prof. Dr. Paulo Roberto Costa

Dissertation submitted to the Institute of Physics  
of the University of São Paulo for the Master of  
Science degree.

Examination Committee:

Prof. Dr. Paulo Roberto Costa (IFUSP)  
Prof. Dr. Manuel Arreola (Universidade da Flórida)  
Profa. Dra. Eloisa Gebrim (FMUSP)

São Paulo  
2017

To my mother and brother, for their love and support. To my boyfriend Thiago, for never stop believing me. To my friends, for staying by my side.

“It always seems impossible until it’s done.”

(Nelson Mandela)

## ACKNOWLEDGMENTS

I am most thankful to my supervisor Paulo for trusting a stranger such a beautiful work. I thank Paulo for introducing me to this topic and for encouraging me to take this step, which is just the first one. I deeply thank him for his patience and support during all these years.

I want to thank CNPq for the financial support, under the project 132554/2015-1.

I also thank the employees and professors from IFUSP. I thank Andrea and Éber for their kindness and for all their help during these years. I thank Prof. Vito Vanin for all the times he helped me with Statistics.

I want to thank all the workers from the mechanical workshop of IFUSP, especially Mr. Marcos Santos de Souza for doing such a great work when manufacturing the dosimeter holders used in this study.

I thank the secretaries from the Nuclear Physics Department, especially Gilda, for their kindness.

I thank Nancy for all the times she patiently assisted me with Risø, particularly in the beginning of my studies, when I was afraid of breaking everything. I also thank Nancy for all the questions she solved about my OSL measurements.

I thank Ricardo for being so gentle and for all the times he helped me with so many measurements, abstracts, and papers.

I deeply thank Prof. Beth, Prof. Emico, and Prof. Ana Regina for their sweetness. I am really thankful for having the opportunity of sharing my days with such amazing women and scientists.

I am deeply thankful to Denise, as her assistance was crucial to the development of this work. I thank Denise for staying with me at the hospital, carrying all that heavy stuff, and mounting the phantoms, even if it was already too late.

I thank InRad for providing me with the instruments and data I needed to develop this study.

I thank Dr. Marcio Sawamura for the numerous times he helped me with this study. I thank Marcio for all the assistance with the patient data collection, with the image segmentation and for always being available to solve all my doubts.

I thank the dear Prof. Alessandra Tomal for all the valuable assistance with MatLab codes.

I want to thank Dr. Manuel Arreola and Izabella Lipnharski for gently receiving me when I visited the University of Florida and for clarifying my doubts about my OSL measurements.

I am thankful to Dr. Choonsik Lee for all the assistance with the NCICT software and for gently answering so many questions about Monte Carlo simulations. I also thank Dr. Richard Kramer and Dr. Helen Khoury for their assistance with the CalDose\_XCT software. All their help was essential for understanding the main results of this investigation.

I thank the IAEA staff for their valuable assistance, since this Master project was carried out as part of the IAEA Coordinated Research Project E2.40.20 entitled “Evaluation and Optimization of Paediatric Imaging”.

I especially thank Prof. Kwan-Hoong Ng for always supporting and encouraging me. I thank Prof. Kwan for every lesson he keeps teaching me, which goes far beyond Physics.

I will always be thankful for the great friends I made in the laboratory during these years. I especially thank Josi, Lorena, Alejandro, and Eduardo for all the wine and laughs we shared. I thank Juliana for being so sweet and for always helping me, even far away. I thank Josi for being a nice companion to work with up until 10pm on a Friday. I fully thank Lorena for being such a good friend when we travelled to Italy, sharing laughs and tears. I also thank Josi for her partnership when we went to Munich and turned Ju's house into a mess. Likewise, I thank Ju and Henrique for being such patient and friendly hosts. I also thank Victor for his partnership during this trip and also at our office, tolerating my bad mood and anxiety. I thank Leandro for all the coffee times and for walking with me to the bus stop because it was too late to go by myself.

I also thank all the employees and teachers from Beethoven Music School, where I found relief in most stressful days. I thank Prof. João and Prof. Lobato for being so friendly and for making me laugh. I especially thank my piano teacher and friend Yramaia for her sweetness. I thank Yramaia for never giving up on me and for understanding the numerous weeks I was not able to study because I needed to stay at the laboratory.

I thank so many friends for staying by my side when I most needed and for understanding my absence. I thank Jorge for the caring, I thank my dear friend Bru Maldonado for being such a great friend and for always being there for me, even when I didn't deserve it. I thank Knorre and Matheus for their valuable friendship. I deeply thank Marcela for supporting me like a sister in every moment of my life since we met. I will always be thankful to Ale, Lucas and Renato for making me laugh when I most needed it. None of this would have been possible if I couldn't have counted on you.

I thank my second family, Simone, Luiz, and Bianca, for their support and for understanding my absence. I thank Simone for all the times she helped me dealing with my anxiety, Luiz for always being so calm and patient and Bianca for being much more a friend than a sister-in-law.

I thank my step-father, Gilberto, for always encouraging me and for all the advices during these years. I thank him for always being worried about me and supporting all my decisions and also for celebrating with me every achievement I get.

I especially thank my lovely boyfriend Thiago for loving me in every single moment of my life, especially when I know I didn't deserve it. As he once told me, our story goes far beyond this work, but he sure has an enormous influence on it. I thank him for always being so proud of me, for having so much faith and trust, and for supporting me whatever I do. My life is easier because I have you by my side, sharing the same wishes and dreams.

At last, I am thankful to my brother and my mother, for being the best family I could possibly choose. I would be nothing without their love and support and I would never be where I am now. I deeply thank my brother Marcinho for believing in me more than I can do myself. I thank him for being my best friend, for helping me deal with my anxiety and (trying to) avoid all the times I got insane. I thank my beautiful mother Sônia for being the strongest woman I have ever known, thus teaching me to be persistent and to never give up on my goals. I thank her for pushing me up during these years when things appeared to be so difficult. If I am where I am now, it is because I could hold your hand whenever I felt down.

## RESUMO

Desde o desenvolvimento do primeiro equipamento de Tomografia Computadorizada (TC) no começo dos anos 1970, essa modalidade de diagnóstico por imagem passou por diversas melhorias. Produção de imagens de alta qualidade e exclusivamente digitais sem a superposição de estruturas anatômicas, exames com a duração de até cinco segundos e a capacidade de detectar patologias importantes sem a necessidade de cirurgias exploratórias são algumas das grandes vantagens obtidas quando essa técnica é utilizada. Como consequência, o papel dessa modalidade diagnóstica tem crescido amplamente ao redor do mundo. Nos Estados Unidos, por exemplo, 2,2 milhões de exames de TC foram realizados em 1980, apenas 10 anos após sua implementação. Esse número cresceu para 78,7 milhões no ano de 2015. Como resultado, a dose de radiação absorvida por pacientes devido ao uso dessa técnica tem se tornado uma preocupação entre radiologistas, pesquisadores e fabricantes, levando ao desenvolvimento de diferentes metodologias para estima-la. Câmaras de ionização, dosimetria termoluminescente (TL) e, mais recentemente, dosimetria luminescente opticamente estimulada (OSL), por exemplo, têm sido amplamente aplicados para se estimar dose em órgãos *in vivo*, em cadáveres e em objetos simuladores (*phantoms*). Outra abordagem extensivamente utilizada é a computacional, baseada em simulações Monte Carlo, que pode ser utilizada na comparação com resultados experimentais. Nesse trabalho, uma abordagem experimental utilizando TLDs e OSLDs em objetos simuladores adulto e pediátrico foi utilizada. Diversas análises foram realizadas com o objetivo de estabelecer o melhor caminho para conseguir os principais resultados alcançados e a metodologia desenvolvida foi eficiente para a finalidade proposta. As características dos OSLDs foram analisadas para verificar sua aplicabilidade no estudo de doses provenientes de procedimentos de TC. As respostas dos dosímetros demonstraram homogeneidade, linearidade com o kerma no ar incidente, reprodutibilidade, possibilidade de reutilização e dependência energética. Esses dosímetros foram utilizados em objetos simuladores adulto e pediátrico para o estudo de doses provenientes de protocolos clínicos de TC selecionados após uma análise de banco de dados de pacientes coletados do Instituto de Radiologia da Faculdade de Medicina da Universidade de São Paulo. As doses em órgãos medidas com os dosímetros foram comparadas com simulações Monte Carlo. Para órgãos contidos na região de exame, as diferenças entre doses medidas e simuladas estão no intervalo de  $\pm 20\%$ . Esses resultados demonstraram, ainda, que o alinhamento e posicionamento incorretos do paciente antes do exame podem ocasionar um aumento maior do que 100% na dose de um órgão.

**Palavras-Chave:** Tomografia Computadorizada; Radiologia; Dosimetria TL e OSL; Doses em órgãos.

## ABSTRACT

Since the development of the first Computed Tomography (CT) equipment in the early 1970s, this diagnostic imaging modality has gone through several improvements. Exclusively digital and high quality images production without superposition of anatomical structures, examinations as fast as five seconds, and the capability of diagnosing important pathologies with no need of exploratory surgeries are some of the great advantages when using this technique. As a consequence, the role of this diagnostic procedure has been widely increasing worldwide. In the US, for instance, 2.2 million CT exams were performed in 1980, only 10 years after its implementation. This number increased to 78.7 million in 2015. As a result, absorbed dose by patients due to this technique has become a concern among radiologists, researchers and manufacturers, leading to the development of different methodologies to evaluate it. Ionization chambers, thermoluminescence (TL) and, more recently, optically stimulated luminescence (OSL) dosimetry, for instance, have been widely applied in order to estimate *in vivo* organ doses, in post-mortem subjects and in phantoms. Another approach that has been extensively used are the Monte Carlo simulations, which can be applied in comparison with experimental results. An experimental approach to evaluate organ doses in pediatric and adult anthropomorphic phantoms by using TLDs and OSLDs was employed in the present study. Several analyses were performed in order to establish the best way to achieve the main results in this investigation and the methodology proved to be efficient. The characteristics of the OSLDs were analyzed to verify their applicability for evaluating doses from CT procedures. The characterization included homogeneity, linearity with the incident air kerma, reproducibility, reusability and an energy-dependent response to distinct effective energies evaluation. These dosimeters were applied along with TLDs in an adult and a pediatric anthropomorphic phantoms to evaluate organ doses due to clinical CT protocols. These protocols were selected after an analysis of patient data collected from the Institute of Radiology of the School of Medicine of the University of São Paulo (*Instituto de Radiologia da Faculdade de Medicina da Universidade de São Paulo*). Organ doses measured with dosimeters were compared with Monte Carlo simulations. Differences between measured and simulated absorbed organ doses were within  $\pm 20\%$ . Moreover, these results showed that a misalignment and incorrect positioning of the patient in the couch can increase an organ dose by more than 100%.

**Keywords:** Computed Tomography; Radiology; TL and OSL dosimetry; Organ doses.

## LIST OF FIGURES

Figure 2.1 – Historical overview of the four generations of CT scanners. The first generation operated with a translation/rotation principle and a pencil beam. The second generation operated with the same translation/rotation principle, but a partial fan beam substituted the pencil beam. In the third generation, the x-ray tube and the detectors rotated around the patient. In the fourth generation, only the x-ray tube rotated around the patients. Note: Reprinted from Kalender (2011).	25
Figure 2.2 – Basic components of a third-generation CT system gantry. The gantry rotates rapidly around the patient and contains the x-ray circuit, the x-ray tube, the radiation detectors, the high-voltage generator and mechanical supports. Note: Reprinted from Ulzheimer & Flohr (2009).	28
Figure 2.3 – Positioning and alignment of the patient in the gantry. The x-y plane is the axial plane, the x-z plane is the coronal plane and the y-z plane is the sagittal plane. Note: Reprinted from IMPACT (2001).	29
Figure 2.4 – Components of an x-ray tube. Note: Reprinted from Fosbinder & Orth (2011).	29
Figure 2.5 – Left: Schematic representation of the Siemens Straton x-ray tube with its anode directly attached to the tube envelope. Right: The compact design of the Straton x-ray tube allows two acquisition systems within one scanner for dual source and dual energy CT scanners. The Straton tube is 120 mm in diameter. Note: Reprinted from Dehm & Reinsberger (2012).	30
Figure 2.6 – Left: detector arrays are mounted on electronics module with power supplies for amplifiers, amplification circuits for the detector module, and systems to convert the analog signal to digital. Right: A photograph of a detector module from a commercial CT scanner. Note: Reprinted from Bushberg et al. (2011).	31
Figure 2.7 – A bow tie filter is used on body CT scanners and it is placed in the x-ray tube assembly. As a result, it attenuates the x-ray beam in the periphery of the field, reducing patient dose with no image quality loss. Note: Reprinted from Bushberg et al. (2011).	32
Figure 2.8 – Examples of survey radiograph images. Left: AP projection scanogram. Right: LAT projection scanogram. Note: Reprinted from Hsieh (2009).	33
Figure 2.9 – Axial or sequential scanning mode is the basic step-and-shoot mode of the CT scanner. The x-ray beam is deactivated while the patient is being translated to another z-position for the next acquisition. This cycle repeats until the entire anatomical region of interest is scanned. Note: Reprinted from Bushberg et al. (2011).	34
Figure 2.10 – In the Helical CT acquisition, the x-ray tube rotates while the patient table support is translated at constant speed, so that the x-ray beam forms a helix around the patient. Note: Reprinted from Bushberg et al. (2011).	35
Figure 2.11 – The intensity $I$ of radiation is measured in CT. Three simple cases are presented, considering monoenergetic and polyenergetic x-ray beams crossing homogeneous or inhomogeneous objects. For inhomogeneous objects tomographic imaging is necessary to determine the distribution $\mu(x,y)$ . Note: Reprinted from Kalender (2011).	37
Figure 2.12 – Head (16-cm diameter) and body (32-cm diameter) PMMA phantoms used to measure CTDI. Note: Reprinted from < <a href="http://www.universalmedicalinc.com/ct-dose-phantom.html">http://www.universalmedicalinc.com/ct-dose-phantom.html</a> >.	41
Figure 2.13 – Energy level representation of the TL and OSL processes. i. Trapping of the electrons and holes within the crystal lattice due to the exposure to ionizing radiation, where L and T are the hole and electron defects, respectively. ii. Electrons and holes trapped in a metastable state. iii. Thermal or optical stimulation results in the release of the trapped electrons, which can recombine with holes at the recombination centers and emit light. Note: Adapted from Aitken (1998).	48

Figure 3.1 – Left: The slices of the RANDO phantom (The Phantom Laboratory, 2012). Right: The phantom prepared to be irradiated, with all the slices arranged. ....	51
Figure 3.2 - Left: The 10 <sup>th</sup> slice of the CIRS ATOM pediatric phantom, presenting the different tissue equivalent materials used in its manufacture. Right: The phantom prepared to be irradiated. ....	52
Figure 3.3 – Left: The Risø TL/OSL Reader model DA-20 (DTU Nutech. Inc., Roskilde, Denmark). Note: Reprinted from DTU Nutech (2015). Right: 48-position sample carousel. ....	53
Figure 3.4 – Example of a TL curve obtained with the irradiation of one TLD-100 chip (Harshaw Chemical Company, OH, USA) with a 64-slice CT Scanner. ....	55
Figure 3.5 - Left: OSL tape. Right: Fractionated dosimeters (3 mm in diameter and 0.3 mm in thickness). ....	55
Figure 3.6 - Left: a batch of OSLD disks placed in an aluminum recipient. Right: 5 samples of OSLD disks along with a ruler to visualize their shape and size. ....	56
Figure 3.7 – Left: Technical draft (in mm) of the dosimeter holder designed for the RANDO phantom (Martins, 2015). Right: a picture of the dosimeter holder designed for the CIRS ATOM phantom along with a TLD chip and a 3 mm OSLD. ....	57
Figure 3.8 - Example of an OSL curve obtained after the irradiation of one Al <sub>2</sub> O <sub>3</sub> :C OSL Landauer Luxel™ dosimeter (Landauer, Inc., Glenwood, USA) with an x-ray tube. ....	58
Figure 3.9 - Left: Constant potential x-ray tube MCN 421 (Philips, Germany). Right: Dosimeters and ionization chamber were positioned 5 meters away from the x-ray tube. ....	60
Figure 3.10 - Left: The ionization chamber at the isocenter of the gantry of the 64-slice Philips Brilliance 64 CT Scanner (Philips, Germany). Right: The 0.6 cc ionization chamber, model 10X5-0.6, placed on the acrylic holder. Air kerma was measured at this position and then each group of TLD and OSLD was positioned at the same place. ....	60
Figure 3.11 – Example of the application of the thresholding algorithm to a CT image of the CIRS ATOM pediatric phantom. The lung tissue is represented in black and all the other structures are grouped in the white pixels. ....	68
Figure 3.12 - Left: OSL and TL dosimeters placed on the eye lenses of the pediatric anthropomorphic phantom. This picture also demonstrates the laser system used to perform the alignment of the phantom in the isocenter of the gantry. Center: The 8 <sup>th</sup> slice of the anthropomorphic phantom with the dosimeters placed in the location of the thyroid. Right: The 13 <sup>th</sup> slice of the phantom with the 8 groups of dosimeters placed inside the lungs of the phantom. ....	70
Figure 3.13 - Left: OSL and TL dosimeters placed in the thyroid of the adult anthropomorphic phantom, located inside the 9 <sup>th</sup> slice. Center: The 11 <sup>th</sup> slice of the anthropomorphic phantom with the dosimeters placed inside the lungs. Right: The 20 <sup>th</sup> slice of the phantom with the dosimeters placed inside the liver. ....	70
Figure 4.1 - Distribution of the OSLD responses. 452 unused dosimeters were irradiated at the same time with the same technique. Standard deviation corresponded to 5% of the average. ....	79
Figure 4.2 - Energy responses obtained for 8 different x-ray beam qualities. The mean OSL signal obtained for each quality was normalized to the mean OSL signal obtained for the RQT 9 x-ray beam quality. The other two symbols correspond to the energy responses for the Al <sub>2</sub> O <sub>3</sub> :C Luxel dosimeters obtained in distinct works. These data were normalized to the data obtained in this work for comparison and presented similar energy-dependent response. ....	80
Figure 4.3 - Example of the linearity of the OSL response to the air kerma measured by a 30 cc ionization chamber and the MCN 421 x-ray tube with RQT 9 quality. ....	80
Figure 4.4 - Comparison of the linearity responses of the OSLDs (left) and TLDs (right) to the air kerma measured by a 0.6 cc ionization chamber in the MCN 421 x-ray tube and in the CT scanner. ....	

extracting the OSL signal, each OSLD was irradiated with beta radiation in the Risø reader and their responses to beta radiation were used to normalize the OSL signal. TL value is given by the integral of the TL curve from 0°C to 350°C.....	81
Figure 4.5 - Reproducibility test for the three groups. Results were normalized to highlight the standard deviation ( $k=1$ ) of the measurements inside each group. It is possible to notice that the variations are significantly lower when OSL signals were normalized to the dosimeters responses to beta radiation. ....	82
Figure 4.6 – Reusability test performed with dosimeters from the three groups. CV of four readings per dosimeter are presented. Horizontal lines indicate the mean CVs of each group. ....	83
Figure 4.7 – Dosimeter responses per irradiation for groups 1 and 2 and normalized OSL signal for group 3. For each data set, whiskers present the variation range (minimum and maximum values), box contains 50% of data (75% - 25%), the horizontal line inside the box represents the median value of the responses and the square represents the mean value of the data. Groups 1 and 2 presented outliers. ...	84
Figure 4.8 – Left: ten most applied CT examinations performed in pediatric patients at the Institute of Radiology of the School of Medicine of the University of São Paulo (InRad/FMUSP) in 2015. Head CT corresponds to 42% of the total examinations and Thorax CT is the 5 <sup>th</sup> most applied protocol, corresponding to 5% of the total examinations. Right: Five most applied CT procedures during 2014-2016.....	85
Figure 4.9 – Left: ten most applied CT examinations performed in adult patients at the Institute of Radiology of the School of Medicine of the University of São Paulo (InRad/FMUSP) in 2015. Head CT corresponds to 22% of the total examinations and Thorax CT is the 4 <sup>th</sup> most applied protocol, corresponding to 12% of the total examinations. Right: five most applied CT procedures during 2014-2016.....	85
Figure 4.10 - Organ and dosimeter holes localization as proposed by Golikov & Nikitin (1989). Note: Reprinted from Golikov & Nikitin (1989). ....	87
Figure 4.11 – Box plots for $CTDI_{vol}$ and DLP obtained from patient data collected from 2014 to 2016 for Head CT performed at InRad. For each data set, whiskers present the variation range (minimum and maximum values), box contains 50% of data (75% - 25%), the horizontal line inside the box represents the median value and the square represents the mean value of the data. International DRL from three surveys are also presented. $CTDI_{vol}$ for 0-1 y age range and DLP values for 0-1 y and 2-5 y age ranges present outliers. On the horizontal axes, age ranges are presented. ....	94
Figure 4.12 – Box plots for $CTDI_{vol}$ and DLP obtained from patient data collected from 2014 to 2016 for Thorax CT performed at InRad. For each data set, whiskers present the variation range (minimum and maximum values), box contains 50% of data (75% - 25%), the horizontal line inside the box represents the median value and the square represents the mean value. International DRL from three surveys are also presented. $CTDI_{vol}$ for 6-10 y age range and DLP values for 2-5 y age ranges present outliers. On the horizontal axes, age ranges are presented.....	95
Figure 5.1 – a) NCICT (Lee et al., 2015) and b) Caldose_XCT (Kramer et al., 2008) used to simulate organ absorbed doses and compare with experimental results.....	108

## LIST OF TABLES

Table 2.1 – Most relevant events in the history of CT (Buzug, 2008; Kalender, 2011; Seeram, 2015). .....	23
Table 2.2 – Performance characteristics of CT from 1972 to 2010 (Kalender, 2011). .....	26
Table 3.1 – X-ray beam qualities RQR and RQT series used to evaluate the energy response of the dosimeters. X-ray tube voltage (kV), external copper filtration (mm Cu), nominal first HVL (mm Al) and determined effective energy are presented for each radiation quality. ....	63
Table 3.2 - Parameters used to assess OSLD linearity of responses in distinct situations. At the laboratory, the dosimeters and the ionization chamber were placed one meter away from the x-ray tube focal spot. At the hospital, the dosimeters and the ionization chamber were placed in the center of the gantry of the Philips Brilliance 64 CT scanner. ....	64
Table 3.3 - OSL groups considered for the reproducibility and reusability tests .....	65
Table 3.4 - Displacement of dosimeter groups inside the slices of the CIRS ATOM pediatric anthropomorphic phantom along with the organ mass fraction inside each slice for all protocols. ....	72
Table 3.5 – CT acquisition parameters used in the three protocols applied to the CIRS ATOM pediatric anthropomorphic phantom. ....	73
Table 3.6 - Displacement of dosimeter groups inside the slices of the of the RANDO phantom along with the organ mass fraction inside each slice, as determined by Huda & Sandison (1984) and Golikov & Nikitin (1989), for all protocols. ....	75
Table 3.7 - CT acquisition parameters used in the protocols applied to the RANDO anthropomorphic phantom.....	76
Table 3.8 – Mass-energy absorption coefficient obtained for each compound and applied in order to estimate the organ doses (effective energy of 56.1 keV). ....	77
Table 4.1 - Linearity response parameters obtained for distinct situations. ....	81
Table 4.2 - Lung and liver mass fraction, $f_i$ , inside each slice $i$ of the adult anthropomorphic RANDO phantom (Golikov & Nikitin, 1989; Huda & Sandison, 1984). ....	86
Table 4.3 – Liver volume per 25 mm interval ( $\text{cm}^3$ ) obtained for five patients with the software iSite Radiology (Philips, Germany). These quantities were used as an approximate estimative of the fractions of this organ inside each slice of the anthropomorphic physical phantom. Each interval corresponds to a 25 mm section of the patient containing the liver, corresponding to the 5 physical phantom slices that contains the liver according to Inkoom et al. (2015).....	88
Table 4.4 – Lung and liver mass fraction, $f_i$ , inside each slice $i$ of the CIRS ATOM pediatric anthropomorphic phantom estimated with a threshold algorithm (lung) and with the iSite Radiology software along with their uncertainties. Confidence level considered is 68.3% ( $k = 1$ ). ....	88
Table 4.5 – Calibration curves, organ doses and dosimetric quantities for the Thorax for children protocol applied to the CIRS ATOM pediatric phantom. ....	90
Table 4.6 – Calibration curves, organ doses and dosimetric quantities for the Thorax, abdomen and pelvis protocol applied to the RANDO adult phantom and to the CIRS ATOM pediatric phantom. ....	91
Table 4.7 - Calibration curves, organ doses and dosimetric quantities for the Head/Head and Neck protocol applied to the RANDO adult phantom and to the CIRS ATOM pediatric phantom. ....	92
Table 4.8 – $\text{CTDI}_{\text{vol}}$ and DLP median values for Head CT examinations obtained with patient data collected in the present work. DRL from three different surveys are presented for comparison.....	93

Table 4.9 - CTDI<sub>vol</sub> and DLP median values for Thorax CT examinations obtained with patient data collected in the present work. DRL from three different surveys are presented for comparison.....95

Table 5.1 - Absorbed doses (mGy) calculated for both TLD and OSLD and simulated values obtained with NCICT and CalDose for the Thorax for children protocol. Percent deviation ( $\Delta$ ) values between experimental and simulated values for the CIRS ATOM phantom are also presented.....109

Table 5.2 - Absorbed doses (mGy) calculated for both TLD and OSLD and software NCICT and CalDose for the Thorax, abdomen and pelvis protocol. Percent deviation ( $\Delta$ ) values between experimental and simulated values for the CIRS ATOM phantom and for the RANDO phantom are also presented. ....110

Table 5.3 - Absorbed doses (mGy) calculated for both TLD and OSLD and software NCICT and CalDose for the Head and Head and Neck protocol. Percent deviation ( $\Delta$ ) values between experimental and simulated values for the CIRS ATOM phantom and for the RANDO phantom are also presented. ....110

## ACRONYMS

AAPM – American Association of Physicists in Medicine  
AEC – Automatic Exposure Control  
ALARA – As Low As Reasonably Achievable  
AP – Anterior-Posterior  
ART – Algebraic Reconstruction Technique  
ATCM – Automatic Tube Current Modulation  
CB – Conduction Band  
CBCT – Cone Beam CT  
CIRS – Computerized Imaging Reference Systems  
CRP – Coordinated Research Project  
CT – Computed Tomography  
CTA – Computed Tomography Angiography  
CTDI – Computed Tomography Dose Index  
CV – Coefficient of Variation  
CW-OSL – Continuous Wave Optically Stimulated Luminescence  
DICOM – Digital Imaging and Communication in Medicine  
DLP – Dose Length Product  
DRL – Diagnostic Reference Levels  
EF – Effective Diameter  
FOV – Field of View  
HU – Hounsfield Unit  
HVL – Half Value Layer  
IAEA – International Atomic Energy Agency  
IC – Ionization Chamber  
ICRP – International Commission on Radiation Protection  
LAT – Lateral  
LDCT – Low Dose CT  
LED – Light Emitting Diode  
MC – Monte Carlo  
MDCT – Multi-Detector Computed Tomography  
MRI – Magnetic Resonance Imagin

MSCT – Multi-Slice Computed Tomography  
NCICT – National Cancer Institute Dosimetry System for CT  
NIST – National Institute of Standards and Technology  
OSL – Optically Stimulated Luminescence  
OSLD – Optically Stimulated Luminescent Dosimeter  
PA – Posterior-Anterior  
PACS – Picture Archiving and Communication System  
PET/CT – Positron Emission Tomography/ Computed Tomography  
PMMA – Poly(methyl methacrylate) Acrylic  
PMT – Photomultiplier Tube  
PVC – Polyvinyl Chloride  
QA – Quality Assurance  
QC – Quality Control  
RIS – Radiology Information System  
SSDE – Size Specific Dose Estimates  
SSDL – Secondary Standard Dosimetry Laboratories  
TCM – Tube Current Modulation  
TL – Thermoluminescence  
TLD – Thermoluminescent Dosimeter  
ULDC – Ultra-Low Dose Computed Tomography  
VB – Valence Band

## CONTENTS

<b>RESUMO.....</b>	<b>VIII</b>
<b>ABSTRACT .....</b>	<b>IX</b>
<b>LIST OF FIGURES.....</b>	<b>X</b>
<b>LIST OF TABLES.....</b>	<b>XIII</b>
<b>ACRONYMS.....</b>	<b>XV</b>
<b>1. INTRODUCTION.....</b>	<b>20</b>
<b>2. THEORY.....</b>	<b>22</b>
2.1. COMPUTED TOMOGRAPHY: A HISTORICAL OVERVIEW .....	22
2.1.1. The Seventies: From Head to Whole Body Scanning .....	24
2.1.2. The Eighties: Fast Scanning of Single Slices .....	25
2.1.3. The Nineties: Fast Volume Scanning .....	25
2.1.4. The 2000s: Diversity and Faster Volume Scanning .....	26
2.1.5. The 2010s: Dose reduction in CT .....	27
2.2. THE PHYSICS OF THE COMPUTED TOMOGRAPHY SCANNERS .....	27
2.2.1. Gantry and Patient Support Table .....	27
2.2.2. X-ray Electrical Circuit .....	29
2.2.3. X-ray Tube.....	29
2.2.4. Radiation detectors .....	31
2.2.5. Filters .....	31
2.2.6. Further Components .....	32
2.3. COMPUTED TOMOGRAPHY ACQUISITION MODES .....	32
2.3.1. Survey Radiograph .....	33
2.3.2. Axial/Sequential Acquisition.....	33
2.3.3. Spiral/Helical Acquisition .....	34
2.3.4. Volume scanning: Cone-beam Acquisition.....	35
2.4. IMAGING.....	36
2.4.1. CT number and Hounsfield Unit .....	39
2.5. TUBE CURRENT MODULATION (TCM) IN COMPUTED TOMOGRAPHY ...	39
2.6. DOSIMETRY IN COMPUTED TOMOGRAPHY .....	40
2.6.1. Computed Tomography Dose Index (CTDI) and Dose Length Product (DLP).40	
2.6.2. Size Specific Dose Estimates (SSDE).....	43
2.6.3. Diagnostic Reference Level (DRL).....	44

2.6.4.	Evaluation of Organ Doses.....	45
2.7.	THERMOLUMINESCENT AND OPTICALLY STIMULATED LUMINESCENT DOSIMETRY .....	46
<b>3.</b>	<b>MATERIALS AND METHODS .....</b>	<b>50</b>
3.1.	MATERIALS.....	50
3.1.1.	Anthropomorphic phantoms.....	50
3.1.2.	Risø TL/OSL reader .....	52
3.1.3.	Dosimeters .....	53
3.1.4.	Irradiation instruments.....	58
3.2.	METHODS .....	59
3.2.1.	OSLD Characterization .....	59
3.2.2.	Selection of CT Scanning Protocols.....	65
3.2.3.	Organ Volumes Determination for Adult and Pediatric Phantoms.....	66
3.2.4.	Phantom Irradiations .....	69
3.2.5.	Organ Doses Evaluation .....	76
3.2.6.	Comparison of patient data with international DRL .....	78
<b>4.</b>	<b>RESULTS.....</b>	<b>79</b>
4.1.	OSLD CHARACTERIZATION.....	79
4.2.	SELECTION OF CT SCANNING PROTOCOLS .....	84
4.3.	ORGAN VOLUMES DETERMINATION FOR ADULT AND PEDIATRIC PHANTOMS .....	86
4.3.1.	The RANDO Phantom .....	86
4.3.2.	The CIRS ATOM Model 705 Phantom.....	87
4.4.	ORGAN DOSES EVALUATION.....	89
4.4.1.	Thorax.....	89
4.4.2.	Thorax, abdomen and pelvis.....	90
4.4.3.	Head/Head and Neck .....	91
4.5.	COMPARISON OF PEDIATRIC PATIENT DATA WITH INTERNATIONAL DRL 93	
<b>5.</b>	<b>DISCUSSION .....</b>	<b>96</b>
5.1.	OSLD CHARACTERIZATION.....	96
5.2.	SELECTION OF CT SCANNING PROTOCOLS .....	100
5.3.	ORGAN VOLUMES DETERMINATION FOR ADULT AND PEDIATRIC PHANTOMS .....	102
5.4.	ORGAN DOSES EVALUATION.....	103

5.4.1.	Thorax: CIRS ATOM Phantom.....	103
5.4.2.	Thorax, abdomen and pelvis: CIRS ATOM Phantom and RANDO Phantom	104
5.4.3.	Head/Head and Neck: CIRS ATOM Phantom and RANDO Phantom.....	105
5.4.4.	Comparative evaluation between measured and simulated organ doses.....	107
5.5.	COMPARISON OF PATIENT DATA WITH INTERNATIONAL DRL .....	111
<b>6.</b>	<b>CONCLUSIONS .....</b>	<b>115</b>
	<b>REFERENCES .....</b>	<b>117</b>
	<b>APPENDIX A.....</b>	<b>125</b>
	<b>APPENDIX B.....</b>	<b>126</b>
	<b>APPENDIX C.....</b>	<b>128</b>
	<b>APPENDIX D.....</b>	<b>130</b>

## 1. INTRODUCTION

Computed Tomography (CT) became clinically available in the beginning of the 1970s, innovating the practice of Medicine by substantially decreasing the need of exploratory surgery (Bushberg, Seibert, Leidholdt Jr, & Boone, 2011). CT images result from passing x-ray through the body by rotating the x-ray tube around the patient, while a detector array placed opposite to the tube acquires the projection data at different angles. The word *tomograph* is referred to a picture (*graph*) of a slice (*tomo*) (Bushberg et al., 2011).

CT was the first medical imaging modality that produced digital images of body sections without superposition (Bushberg et al., 2011; Kalender, 2011). Such imaging modality presents a volume representation by combining single slices, and providing 3-dimensional representation of the anatomy of interest (Bushberg et al., 2011). Recently, modern CT scanners can acquire about 800 high quality images with up to 0.62 mm in thickness in only 5 seconds, revealing malignancies, such as cancers, aneurysms, and many other pathologies (Bushberg et al., 2011).

Since the development of the first CT equipment, this diagnostic imaging modality has been rapidly expanding, mainly due to the speed of acquisition, and high quality images (ICRP, 2000). Surveys, such as the conducted in the United States in 1987, estimated that in 1980, only few years after its implementation, 2.2 million CT procedures were performed in general hospitals (Bunge & Herman, 1987). In 2007, it was estimated that more than 62 million CT procedures had been realized per year, from which at least 4 million were pediatric procedures (Brenner & Hall, 2007). In 2015, around 78.7 million CT procedures were performed in the US, representing a 3% decrease compared with 2014, when 81.2 million procedures were performed. Such apparent decrease might have been influenced by the change in the US reimbursement policy from medical centers (International Marketing Ventures, 2015).

A similar growth is found in England. In 2014, for instance, from the 42.9 million imaging examinations performed from April 2013 to March 2014, 23.1 million were radiographs, 10.0 million were ultrasound, 5.2 million were CTs, and 4.6 million included MRI, fluoroscopy, and radio-isotopes. Compared to the previous period, CT examinations presented a 10% increase. Over the last 10 years, the volume of CT scans performed has increased by 160%, representing an average growth of 10.1% per year (NHS England, 2014).

The situation is also similar in Brazil. In 2016, approximately 4.4 million CT procedures were performed only in the Brazilian Public Health System (*Sistema Único de Saúde*, in

Portuguese), against 4 million procedures in 2015, 3.6 million in 2014 and 1.6 million in 2008 (Ministério da Saúde (Brasil), 2016).

As a consequence of the increasing number of CT procedures, radiation dose absorbed by patients due to this technique has become a concern among radiologists, researchers, and manufacturers (Brenner & Hall, 2007; IAEA, 2014). Currently, there are still many challenging methods associated with the wide use of CT, with emphasis on optimization, and justification, which needs to be developed. (Rehani, 2015; World Health Organization & IAEA, 2013).

The present study aims to evaluate organ doses due to clinical CT protocols routinely applied at a partner hospital, by using Lithium Fluoride doped with Magnesium and Titanium (LiF:Mg, Ti) thermoluminescent dosimeters (TLDs) chips and Aluminum Oxide doped with Carbon (Al<sub>2</sub>O<sub>3</sub>:C) optically stimulated luminescent dosimeters (OSLDs) in adult and pediatric anthropomorphic phantoms. To do so, OSLDs characteristics were extensively assessed to verify their applicability in measuring CT doses. Additionally, this study aims to evaluate protocols frequently applied to pediatric patients, looking for tools to optimize non-adequate practices. After this analysis, three different clinical protocols were selected and adopted in experimental measurements. In order to present the methodology applied and results obtained, this work is divided in six chapters.

- Chapter 1 introduces the motivation and justification of this study.
- Chapter 2 presents the theoretical aspects related to the investigation conducted in the present work.
- Chapter 3 describes the instruments used and the methods adopted to perform the characterization of OSLDs, to select the protocols, to irradiate phantoms and to estimate organ doses.
- Chapter 4 presents the most relevant results found in the present study: OSLD characteristics, evaluation of patient data collected and measured organ doses.
- Chapter 5 discusses the results, based on similar studies published by other authors, and by comparing measured organ doses with Monte Carlo simulations.
- Chapter 6 presents the main conclusions and suggestions for future investigations.

## **2. THEORY**

### **2.1. COMPUTED TOMOGRAPHY: A HISTORICAL OVERVIEW**

The application of computed tomography (CT) as a diagnostic procedure has become essential in clinical routine since its development in the beginning of the 1970s. It was the first non-invasive method to acquire images of inside the human body that were not affected by superposition of the anatomical structures, which happens in a two-dimensional imaging modality such as projection radiograph. The implementation of the first CT equipment was a result of Allan MacLeod Cormack and Godfrey Newbold Hounsfield work during the 1960s and the beginning of the 1970s. In 1972, the EMI Mark I was launched as the first CT scanner and Hounsfield's invention gave the British company EMI Ltd. the monopoly in the CT market (Kalender, 2011). The great impact of this technique was the reason why A.M. Cormack and G.N. Hounsfield were jointly awarded the 1979 Nobel Prize in Physiology or Medicine in recognition of their important accomplishment (Bushberg et al., 2011; Buzug, 2008; Kalender, 2011). Table 2.1 summarizes the most relevant events in CT.

Table 2.1 – Most relevant events in the history of CT (Buzug, 2008; Kalender, 2011; Seeram, 2015).

Year	Event
1985	Discovery of the x-rays by W.C. Roentgen.
1917	Development of a reconstruction algorithm of cross-sectional images from transmission measurements by J.H. Radon.
1937	Development of a tomographic technique in which the sections were transverse sections by W. Watson. These images lacked enough detail and clarity to be used for diagnostic purposes.
1958	Development of an x-ray scanner with an attempt to measure thin slices through a patient, with analogue reconstruction principles, by Korenblyum.
1963	Development of a technique for calculating the absorption distribution in the human body by A.M. Cormack.
1972	Conduction of the first clinical CT examinations by G.N. Hounsfield and J. Ambrose.
1975	Introduction of a first whole-body CT scanner in clinical use.
1979	Hounsfield and Cormack were awarded the Nobel Prize in Physiology or Medicine
1989	First clinical examinations with spiral CT by W.A. Kalender and P.Vock
1998	Introduction of multi-slice CT scanners, with four slices.
2004	Introduction of 64-slice CT scanners.
2006	Introduction of dual-energy CT.
2010	More than 50,000 whole-body CT scanners installed worldwide.

Over the past 40 years, CT scanner technology and image quality has been rapidly improving. The first images acquired in the 1970s consisted of an  $80 \times 80$  pixels and 3 bit matrix. Furthermore, a single rotation could last 4-5 minutes. Nowadays, images have evolved to a  $512 \times 512$  pixels matrix and rotation time can be less than half of a second. Such improvements led this procedure to be extensively used in the clinical routine all over the world, despite the technological developments in other radiological methods (Bushberg et al., 2011; Kalender, 2011).

CT scanners are usually classified in generations according to the evolution of their technology. However, this classification is not a consensus among the authors. Some authors define four generations of CT scanners until 2010 (Bushberg et al., 2011; Buzug, 2008). The arrangement proposed by W. A. Kalender (2011) was formulated considering the development achieved in each decade since the implementation of the first CT equipment and is adopted in the present work.

### *2.1.1. The Seventies: From Head to Whole Body Scanning*

Hounsfield designed the first experimental CT scanner model, which is commonly referred to as the “first generation” equipment, in the late 1960s. This equipment operated with a pencil beam geometry, in which every ray of the beam are parallel to each other, and a translation-rotation principle, in which the radiation source and the detector perform a linear translatory motion successively after a small rotational increment. In the first examinations, in 1969, tests were performed with phantoms and a radioactive source. Scan times reported were approximately nine days per image. The first commercial CT scanner, referred to as the “second generation equipment”, differed from the Hounsfield’s model on the amount of detectors employed, working with a small fan beam geometry. In this geometry, the beam rays in a given projection diverge and appears as a fan. With such technology, scan times were reported to be five minutes and a single examination time was approximately thirty-five minutes, which represented an impressive performance at that moment.

In 1976, the 20-second scan time per image goal was achieved when a fan beam and a larger detector arc were introduced to simultaneously measure a complete projection. Whole-body scans during an individual breathhold became possible (Kalender, 2011). The translational motion became obsolete and the new system only used the rotatory motion (“third generation”), in which both x-ray tube and the detector rotated around the patient, requiring higher technical efforts but improving image quality. In the so-called “forth generation” of CT scanners, a ring-like stationary system of detector fully encircling the patient was established. At that moment, the translation-rotation systems were almost expired and the development of multi-row detectors to reduce scan times was the current ambition. The four generations of CT scanners described are presented in Figure 2.1.

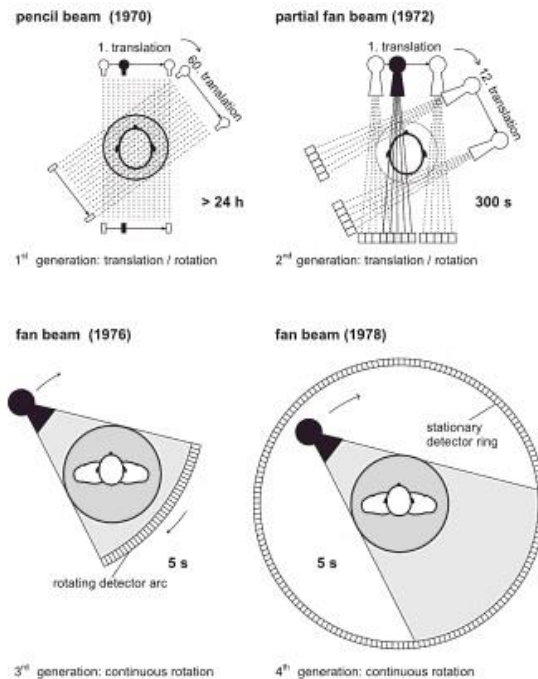


Figure 2.1 – Historical overview of the four generations of CT scanners. The first generation operated with a translation/rotation principle and a pencil beam. The second generation operated with the same translation/rotation principle, but a partial fan beam substituted the pencil beam. In the third generation, the x-ray tube and the detectors rotated around the patient. In the fourth generation, only the x-ray tube rotated around the patients. Note: Reprinted from Kalender (2011).

### 2.1.2. The Eighties: Fast Scanning of Single Slices

In the beginning of the 1980s, the electrical energy system used to feed the x-ray tube prevented a fast and continuous rotation, since it was performed by high-voltage cables. Such system provided scan times per image around two seconds, which were not sufficiently fast for some clinical demands. The most promising approach adopted to reduce scan times was achieved by Siemens Medical Systems and Toshiba Medical Systems, with the introduction of continuously rotating CT systems in 1987, by applying the slip ring technology. A slip ring is a circular electric contact that enables the transmission of energy via sliding contacts situated between the outside of the gantry and the rotating sample (Ulzheimer & Flohr, 2009). This technology enables the system to function with continuous data acquisition (Bushberg et al., 2011; Buzug, 2008), reducing scan times to approximately one second. It was the basis for the development of the spiral CT.

### 2.1.3. The Nineties: Fast Volume Scanning

In 1990, the Siemens SOMATOM PLUS was the only model of spiral CT commercially available, used for the first experimental and clinical trials. Some years later, in 1992, most of

the major CT manufacturers launched spiral CT scanners with the slip ring technology. By that moment, CT technology experienced great improvements. In 1994, a dual-row detector system was introduced. In 1998, a four-slice CT scan, with scan times of 500 milliseconds, was introduced with significantly reduced scan times.

The end of the fourth generation of CT scanner (scanners with stationary rings) was marked by the introduction of multi-row detector systems, called multi-detector CT (MDCT) or multi-slice CT (MSCT). Nowadays, the latest and most modern CT scanners commercially available are adapted from the third generation (scanners with rotating detector arrays).

#### 2.1.4. The 2000s: Diversity and Faster Volume Scanning

The trends shown in the 1990s continued in the first decade of the 2000s. With the introduction of wider cone beams, volume scans were performed even faster than previously reported. Dual source CT, dual energy CT and several forms of flat-detector CT were other important approaches during this decade.

As a summary of the rapid and remarkable development of the CT technology, Table 2.2 presents the performance characteristics of CT in the course of time (Kalender, 2011). Image quality and artifact behavior have been improved steadily since the 1980s.

Table 2.2 – Performance characteristics<sup>a</sup> of CT from 1972 to 2010 (Kalender, 2011).

	1972	1980	1990	2000	2010
<b>Rot. Time per 360°</b>	300 s	5 - 10 s	1 - 2 s	0.33 - 0.5 s	0.27 - 0.35 s
<b>Min. eff. scan time<sup>b</sup></b>	300 s	3 s	0.7 s	0.2 - 0.3 s	0.075 - 0.2 s
<b>Data per 360° scan</b>	57.6 kB	0.2 - 1 MB	1 - 2 MB	5 - 20 MB	0.1 - 1 GB
<b>Data per spiral scan</b>	-	-	12 - 24 MB	0.1 - 1 GB	1 - 100 GB
<b>Image matrix<sup>c</sup></b>	80 × 80	256 × 256	512 × 512	512 × 512	512 × 512
<b>Power</b>	2 kW	10 kW	40 kW	60 - 100 kW	80 - 120 kW
<b>Slice thickness</b>	13 mm	2 - 10 mm	1 - 10 mm	0.5 - 1 mm	0.4 - 0.6 mm
<b>Spatial resolution</b>	3 Lp/cm	8-12 Lp/cm	10-15 Lp/cm	12-15 Lp/cm	12-25 Lp/cm
	5 mm/	3 mm/	3 mm/	3 mm/	3 mm/
<b>Contrast resolution</b>	5 HU/	3 HU/	3 HU/	3 HU/	3 HU/
	50 mGy	30 mGy	30 mGy	30 mGy	30 mGy

<sup>a</sup> Typical values for high performance CT scanners.

<sup>b</sup> Less than 100 ms only available in dual source CT.

<sup>c</sup> Values refer to the calculated matrix.

### 2.1.5. *The 2010s: Dose reduction in CT*

Dose reduction and image quality improvements are the most important advances experienced over this decade. Recently, dose reduction has become a concern among scientists and manufacturers, who are investing in safety of their equipment so that tools for dose reduction are featured on new machines (Kalender, 2014). Some examples include iterative reconstruction techniques, automatic exposure control (AEC), safety cut-offs to prevent high doses, prompts for matching protocols to patient sizes, organ-specific modulation, optimization of x-ray spectra and x-ray beam adaptive collimation (Amis, 2011; Kalender, 2014).

Iterative reconstruction algorithms can generate images with significantly lower noise. As a consequence, a reduced exposure setting on the CT scanner, such as tube current-time product, can be lowered to reduce patient exposure (Mayo-Smith, Hara, Mahesh, Sahani, & Pavlicek, 2014). Such approach has been evaluated in terms of their advantages and limitations up until today. Dodge et al. (2016), for instance, evaluated the performance of two iterative reconstruction algorithms for achieving potential patient dose reduction, by imaging a Catphan 600 modular phantom. Tube current modulation (TCM), applied in many ways in different AEC systems, can reduce the delivered radiation dose by 35%-60% (Reina, 2014; Söderberg & Gunnarsson, 2010). Gharbi et al., (2017) for instance, performed a study with an anthropomorphic phantom and a 128-slice CT scanner by including TCM to a standard chest protocol. These authors reported a 48.8% of dose reduction when TCM was included.

## 2.2. THE PHYSICS OF THE COMPUTED TOMOGRAPHY SCANNERS

In simple terms, a CT scanner consists of a 360-degree rotation gantry, a patient support table, a computer system and an operator's console. The gantry is a rotating system containing the x-ray assembly and the radiation detectors. Along with the patient support table, they are the two largest components of a CT machine, so-called examination unit. The gantry and the patient support table are similar in design for most CT units, while the other essential components are specific to each manufacturer (Bushberg et al., 2011; Fosbinder & Orth, 2011; Kalender, 2011).

### 2.2.1. *Gantry and Patient Support Table*

The gantry is the rotating structure of the CT scanner. It weighs 400-1,000 kg and has a 50-80 cm aperture for the patient to pass through in an examination (Fosbinder & Orth, 2011). The gantry contains the x-ray circuit, the x-ray tube, the radiation detectors, the filters, the high-

voltage generator and mechanical supports. The electrical energy transfer to the x-ray tube and to the other components of the rotating part of the gantry and the data transfer from the detectors back to the stationary part of the gantry is performed by slip rings in the modern CT scanners. Figure 2.2 presents a view from the inside of the gantry, showing its main components (Ulzheimer & Flohr, 2009).

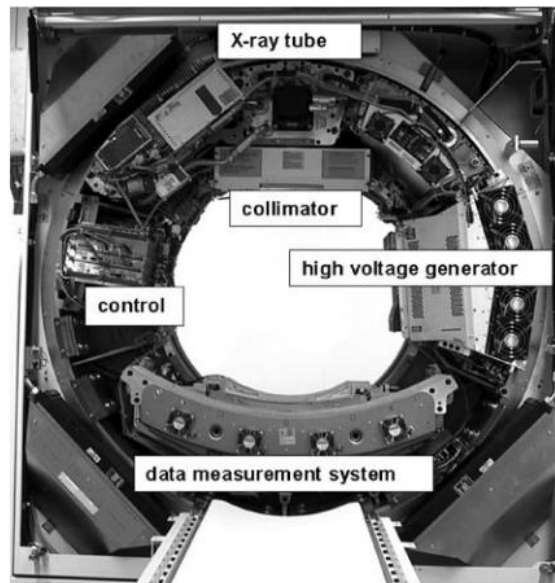


Figure 2.2 – Basic components of a third-generation CT system gantry. The gantry rotates rapidly around the patient and contains the x-ray circuit, the x-ray tube, the radiation detectors, the high-voltage generator and mechanical supports. Note: Reprinted from Ulzheimer & Flohr (2009).

The patient support table is manufactured with low atomic number carbon graphite fiber in order to reduce the attenuation of the x-ray beam. It can be moved into the gantry aperture and moved up and down to facilitate patient transferring and positioning (Fosbinder & Orth, 2011). The proper patient alignment and positioning in the gantry is performed with a laser system, which is represented in Figure 2.3. The x-y plane is the axial plane, the x-z plane is the coronal plane and the y-z plane is the sagittal plane (IMPACT, 2001).

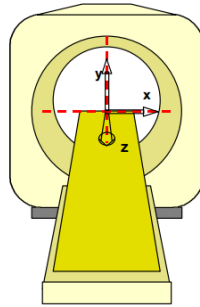


Figure 2.3 – Positioning and alignment of the patient in the gantry. The x-y plane is the axial plane, the x-z plane is the coronal plane and the y-z plane is the sagittal plane. Note: Reprinted from IMPACT (2001).

### 2.2.2. X-ray Electrical Circuit

Two types of x-ray electrical circuits were used in CT units: low frequency (approximately 60 Hz), and high frequency (approximately 3,000 Hz). Because of its big size, the low frequency circuit was located outside the gantry, in the CT examination room, and was connected to the rotating x-ray tube by high-voltage cables. Such cables prevented the tube from rotating continuously (Fosbinder & Orth, 2011). Currently, CT scanners utilize high-frequency circuits, which can be mounted with the rotating x-ray tube inside the gantry and both rotate together around the patient. Cables were replaced by slip rings that enable the circuit and the x-ray tube to have a constant motion (DeMaio, 2010; Fosbinder & Orth, 2011).

### 2.2.3. X-ray Tube

An x-ray tube is composed by two electrodes (cathode and anode) inside a vacuum glass tube, which enables electrons to flow from the cathode to the anode providing an efficient production of x-rays (Fosbinder & Orth, 2011). The components of a typical radiographic x-ray tube are presented in Figure 2.4.

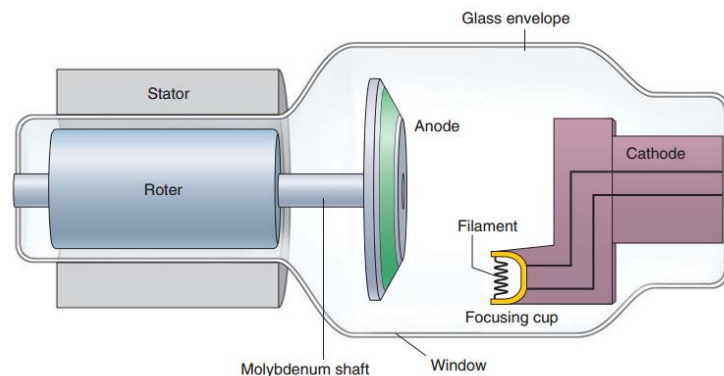


Figure 2.4 – Components of an x-ray tube. Note: Reprinted from Fosbinder & Orth (2011).

The cathode is the negative electrode of the x-ray tube. It contains the filament, which is responsible to provide projection electrons for acceleration into the positive electrode, the anode. The electrons are accelerated from the cathode, acquiring kinetic energy, to the anode by the voltage applied between these electrodes. On the impact of the electrons to the anode target, the kinetic energy is converted to other forms of energy (Bushberg et al., 2011; Fosbinder & Orth, 2011). The focal spot, where the electrons stop after being accelerated, is located in the anode. Since it can reach high temperature during an x-ray exposure, the anode material must be made of a high melting point. Usually, Tungsten is the material of choice (Fosbinder & Orth, 2011).

In conventional x-ray tubes, only the anode rotates. This design limits their usage in some diagnostic procedures since, for instance, the anode mass in CT tubes has increased over the years to provide higher heat storage capacity. An important innovation in the x-ray tubes design was presented by Siemens in the beginning of the 2000s with the launch of the Straton tube, which is the “rotating envelope vacuum vessel” technology developed by Siemens, in which both the cathode and the anode rotate (Dehm & Reinsberger, 2012; Schardt et al., 2004). The anode disk is enclosed by a cooling oil (Figure 2.5) that directly cools the anode (Dehm & Reinsberger, 2012). As a consequence, cooling times were reduced, enabling the design of smaller and lighter tubes, which can achieve rotation speeds lower than 0.3 second (Dehm & Reinsberger, 2012; Kalender, 2011).

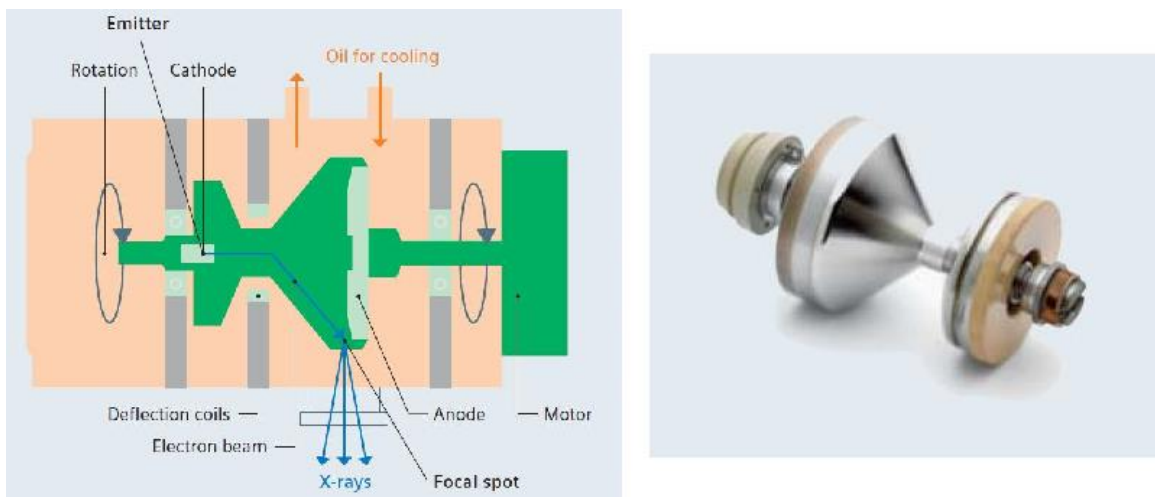


Figure 2.5 – Left: Schematic representation of the Siemens Straton x-ray tube with its anode directly attached to the tube envelope. Right: The compact design of the Straton x-ray tube allows two acquisition systems within one scanner for dual source and dual energy CT scanners. The Straton tube is 120 mm in diameter. Note: Reprinted from Dehm & Reinsberger (2012).

#### 2.2.4. Radiation detectors

Radiation detectors in modern CT scanners are similar to the ones in the third generation of the equipment. In this configuration the detector arc rotates 360 degrees around the patient, opposite to the x-ray tube, measuring the radiation transmitted through the patient at different angles. Rotating detector systems use enough detectors to intercept the entire fan beam (Fosbinder & Orth, 2011).

Two detector types have been mostly applied in CT scanners: ionization chambers filled with gas xenon under high pressure and scintillating solid state detectors in the form of crystals, such as cesium iodide or cadmium tungstate, and ceramic materials, such as gadolinium oxysulfide (Kalender, 2011). Modern commercial helical CT and MDCT scanners use scintillating solid state detectors. Figure 2.6 presents an illustration of a detector system along with a picture of a detector module from a commercial CT scanner.

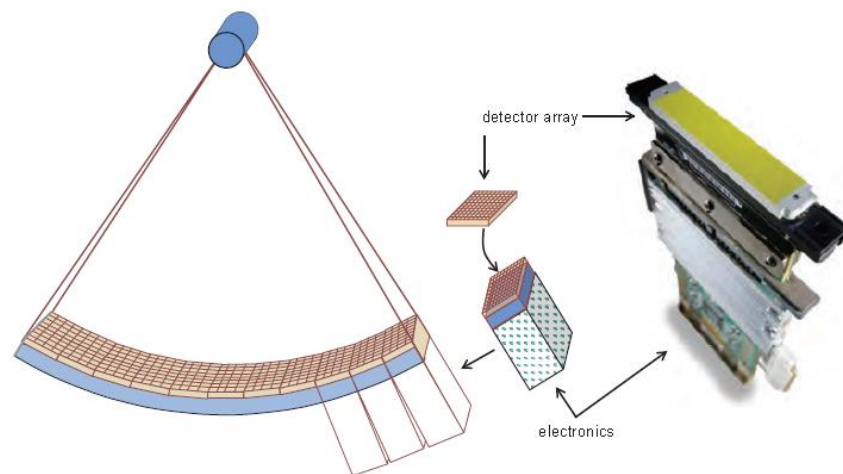


Figure 2.6 – Left: detector arrays are mounted on electronics module with power supplies for amplifiers, amplification circuits for the detector module, and systems to convert the analog signal to digital. Right: A photograph of a detector module from a commercial CT scanner. Note: Reprinted from Bushberg et al. (2011).

#### 2.2.5. Filters

Bow-tie filters are applied in computed tomography systems (Figure 2.7). This filter reduces the intensity of the incident x-ray beam in the periphery of the x-ray field, where the attenuation path through the patient is usually thinner. As a result, the x-ray fluence that reaches the detector array is equalized (Bushberg et al., 2011). Therefore, it is a useful tool due to its capability of reducing the radiation dose delivered to the patient with no image quality loss. All commercial scanners include at least two bow-tie filters: head and body bow-tie filters. Head bow-tie filter is also used in pediatric examinations in most CT scanners (Bushberg et al., 2011).

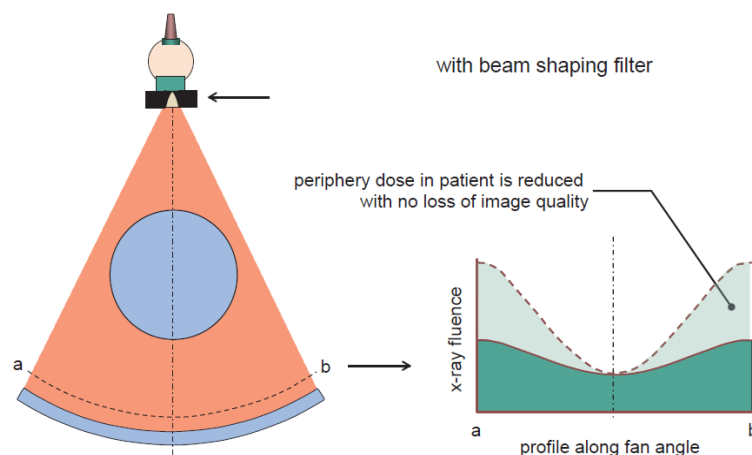


Figure 2.7 – A bow tie filter is used on body CT scanners and it is placed in the x-ray tube assembly. As a result, it attenuates the x-ray beam in the periphery of the field, reducing patient dose with no image quality loss. Note: Reprinted from Bushberg et al. (2011).

### 2.2.6. Further Components

The CT computer must have a processor speed and memory high enough to solve as many as 30,000 calculations simultaneously. The CT computer is designed to control data acquisition, processing, display, and storage. The computer system calculates the attenuation of each voxel with the x-ray exit radiation data collected while the tube rotates around the patient, producing images that can be visualized right after the examination (Fosbinder & Orth, 2011). In the operator's console it is possible to control all scan parameters, including technical factors such as tube voltage (kV) and tube current (mA), movement of the gantry, and position and movement of the patient table. It is also possible to choose reconstruction and transfer of image data (Fosbinder & Orth, 2011).

## 2.3. COMPUTED TOMOGRAPHY ACQUISITION MODES

As a result of the improvement of the CT technique, several acquisition modes have been implemented, including, for instance, axial, helical and cone beam acquisition modes. The routine use of a CT scanner requires only a few scan modes, which can be operated with a wide range of technical parameters settings. In a routine examination, a survey radiograph is taken for orientation over the anatomy of interest and scanning this region in sequential (axial) or in spiral (helical) CT mode (Bushberg et al., 2011; Kalender, 2011).

### 2.3.1. Survey Radiograph

The first step in planning a CT examination is the acquisition of an overview scan, a survey radiograph that is similar to a conventional radiograph. This image is called scanogram, topogram, scout view, localizer or surview test, according to the CT scanner manufacturer (AAPM, 2011a). For this purpose, the x-ray tube and detector array are kept stationary in a fixed angular position while the patient is translated through the field of measurement at low speed and the radiation is emitted continuously. These acquisitions can be in anterior-posterior (AP) direction, posterior-anterior (PA) direction or lateral (LAT) (Figure 2.8).

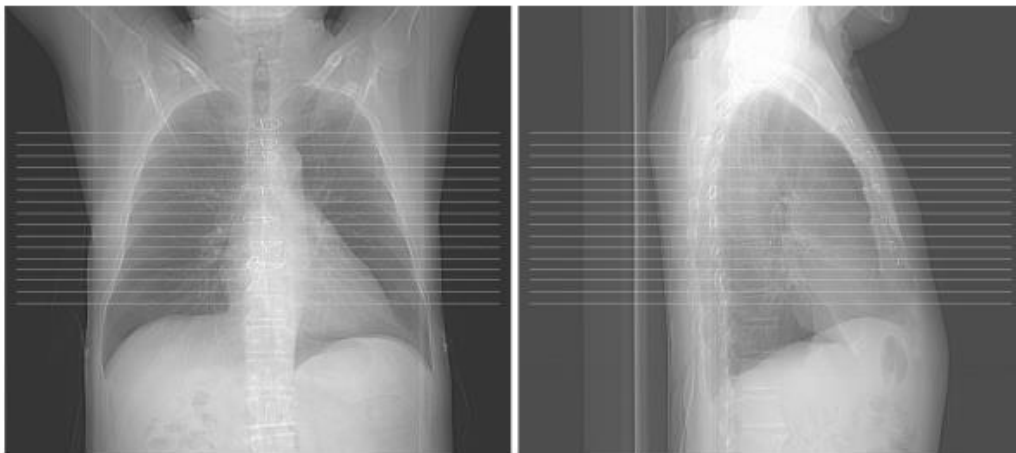


Figure 2.8 – Examples of survey radiograph images. Left: AP projection scanogram. Right: LAT projection scanogram. Note: Reprinted from Hsieh (2009).

Using the CT survey radiograph, all the CT scan parameters such as tube voltage, tube current, gantry rotation time, type of scan (axial or helical), direction of scan, and pitch are selected. Additionally, with the AP overview scan it is possible to plan and program a particular slice plane, slice thickness, number of slices or the scanning volume. With the LAT overview scan it is also possible to program special slice orientations by properly inclining the entire gantry. This is useful in skull radiographs and spinograms to exclude from the scan radiosensitive organs, such as the eye lenses (Buzug, 2008; Hsieh, 2009).

### 2.3.2. Axial/Sequential Acquisition

The axial, also called sequential acquisition, follows a step-and-shoot mode of a CT scanner. The x-ray tube rotates around the patient to collect data for one slice, while the table is positioned into the gantry at a fixed distance (Fosbinder & Orth, 2011). The tube rotates one

more time to collect data for the next slice and this process repeats until the entire region of interest is scanned (Figure 2.9) (Bushberg et al., 2011).

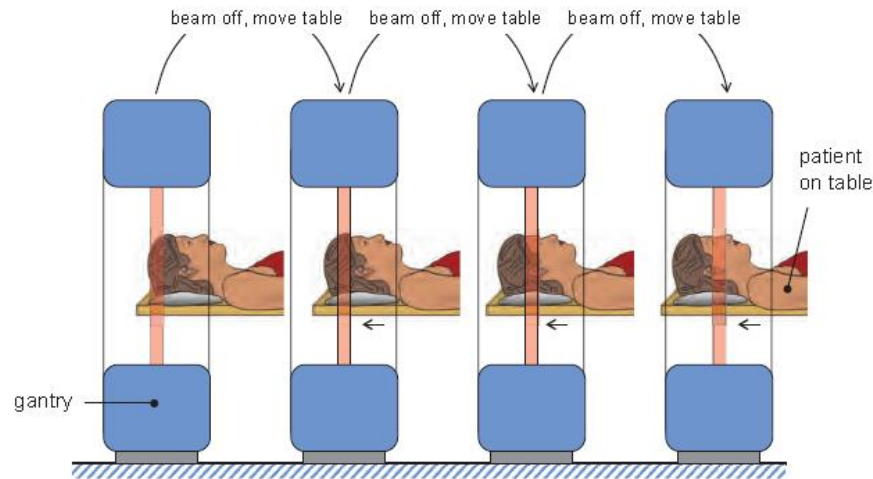


Figure 2.9 – Axial or sequential scanning mode is the basic step-and-shoot mode of the CT scanner. The x-ray beam is deactivated while the patient is being translated to another z-position for the next acquisition. This cycle repeats until the entire anatomical region of interest is scanned. Note: Reprinted from Bushberg et al. (2011).

Because the x-ray tube is deactivated between each sequence, axial CT requires more acquisition time than helical scanning. With the advent of MDCT, this type of acquisition has remained in use for a few clinical applications, such as head scanning, high resolution lung scanning, perfusion CT and interventional applications (Ulzheimer & Flohr, 2009).

### 2.3.3. *Spiral/Helical Acquisition*

Helical CT is the fast and contiguous scanning of complete volumes. This technique replaced the sequential scanning of single or multiple slices, which provides only discrete acquisitions along the z-axis (Kalender, 2011). It became possible with the introduction of the slip ring technology in continuously rotating CT scanners. The acquisition is performed with the table moving at constant speed while the gantry rotates around the patient (Figure 2.10). As a result of this geometry, the x-ray beam forms a helix around the patient. One of the greatest advantages of this kind of acquisition is its speed, by eliminating the start and stop of the x-ray tube in the axial mode (Bushberg et al., 2011; Hsieh, 2009; Kalender, 2011).

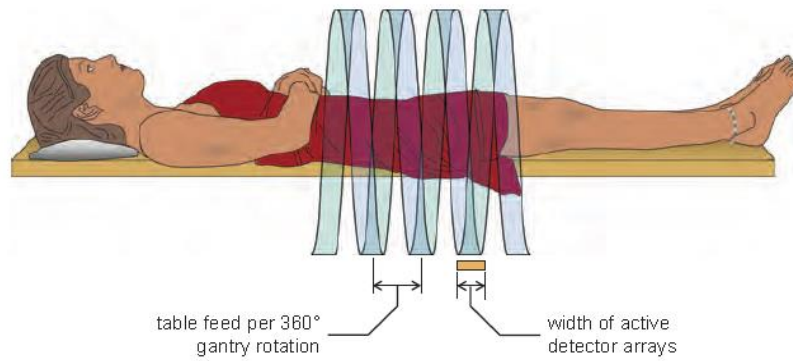


Figure 2.10 – In the Helical CT acquisition, the x-ray tube rotates while the patient table support is translated at constant speed, so that the x-ray beam forms a helix around the patient. Note: Reprinted from Bushberg et al. (2011).

An important parameter to characterize a helical CT acquisition is the pitch ( $p$ ), which describes the relative advancement of the CT patient support table per rotation of the gantry. The pitch is defined as

$$p = \frac{F_{table}}{nT} \quad (2.1)$$

where  $F_{table}$  is the table feed distance per complete rotation of the gantry and  $nT$  is the nominal collimated beam width. In a 64-slice CT scanner ( $n = 64$ ) with width 0.625 mm ( $T = 0.625$  mm), the nominal collimated width in z-axis,  $nT$ , is 40 mm. If the gantry rotation time is 0.5 second, a pitch value of unity ( $p = 1.0$ ) would be achieved if the table constant velocity is 80 mm/s. For most CT scanners, the pitch ranges from 0.75 to 1.5. A pitch lower than 1.0 results in overscanning the patient and higher radiation dose, while a pitch higher than 1.0 results in underscanning and the radiation dose to the patient is lower (Bushberg et al., 2011; Hsieh, 2009). Therefore,

$$dose \propto \frac{1}{pitch} \quad (2.2)$$

#### 2.3.4. Volume scanning: Cone-beam Acquisition

The transition from fan beam to cone-beam geometry happened with the transition from scanning only one slice for the development of an array with 16 to 64 detectors. The main problem with this geometry is that the details in the object are projected onto different detector rows for different projection angles. As a result, data recorded for a 360 degree rotation no longer represent a planar slice as it was the case for a single slice or a few rows. Therefore, the reconstruction of these images requires special algorithms (Araújo, 2008; Costa & Araújo,

2010; Kalender, 2011). Some manufacturers use, for instance, a 3D filtered back projection, with which the rays are back-projected into a 3D volume along the lines of measurement, accounting for their cone-beam geometry (Ulzheimer & Flohr, 2009).

Most CT scanners commercially available consists of 64 or 128 detector rows. Some manufacturers develop a 320-detector array system with 0.5 mm detectors. With the advent of such wide cone beam geometry, it is possible to image a whole organ without table motion with high temporal resolution, which is interesting for CT angiography (CTA) or perfusion, where the anatomical coverage is sufficient for most organs such as kidneys and heart. (Bushberg et al., 2011).

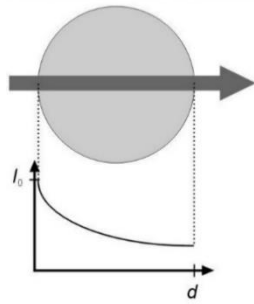
#### 2.4. IMAGING

In simple terms, CT procedures aim at measuring the spatial distribution of a physical quantity to be examined from different directions and without image superposition from these data (Kalender, 2011). CT acquisitions record the relative distribution of the x-ray intensity by using a gray value pattern to derive a diagnostic, as it is performed in classical radiographs. The primary intensity  $I_0$  has to be measured in CT in order to determine the attenuation value along each ray from the source to the detector, in addition to the intensity  $I$  attenuated by the object (Kalender, 2011). The attenuation of the beam is described by Equation 2.3.

$$I = I_0 e^{-\mu d} \quad (2.3)$$

where  $\mu$  is the linear attenuation coefficient and  $d$  is the absorber thickness. Some simple cases are presented in Figure 2.11.

Case 1: homogeneous object, monochromatic radiation.

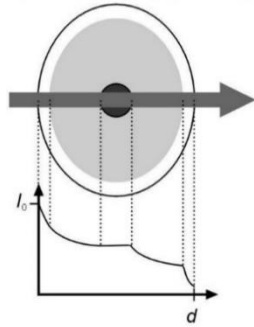


$$I = I_0 \cdot e^{-\mu \cdot d}$$

$$P = \ln \frac{I_0}{I} = \mu \cdot d$$

$$\mu = \frac{1}{d} \cdot \ln \frac{I_0}{I}$$

Case 2: inhomogeneous object, monochromatic radiation.

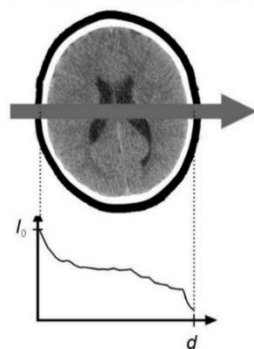


$$I = I_0 \cdot e^{-\mu_1 \cdot d_1 - \mu_2 \cdot d_2 - \mu_3 \cdot d_3 - \dots} = I_0 \cdot e^{-\left[\sum_{i=1}^n \mu_i d_i\right]} = I_0 \cdot e^{-\int_0^d \mu ds}$$

$$P = \ln \frac{I_0}{I} = \sum \mu_i d_i$$

$$\mu_i = ?$$

Case 3: inhomogeneous object, polychromatic radiation.



$$I = \int_0^{E_{\max}} I_0(E) \cdot e^{-\int_0^d \mu(E) ds} dE$$

$$P = \ln \frac{I_0}{I}$$

$$\mu(x, y) = ?$$

KA 2000

Figure 2.11 – The intensity  $I$  of radiation is measured in CT. Three simple cases are presented, considering monoenergetic and polyenergetic x-ray beams crossing homogeneous or inhomogeneous objects. For inhomogeneous objects tomographic imaging is necessary to determine the distribution  $\mu(x,y)$ . Note: Reprinted from Kalender (2011).

The simplest case consists of measuring a homogeneous object with monochromatic radiation (case 1 in Figure 2.11). In this case, the intensity falls off exponentially with absorber thickness. Attenuation is defined as the natural logarithm of the ratio of the primary intensity,  $I_0$ , to the attenuated intensity,  $I$ , and in this case it is simply related to the product of the linear attenuation coefficient  $\mu$  and the absorber thickness  $d$ . If the absorber thickness is known, the linear attenuation coefficient can be directly determined.

Case 2 in Figure 2.11 represents an inhomogeneous object crossed by a monoenergetic x-ray beam. The attenuation during irradiation depends on the local value of the linear attenuation coefficient  $\mu_i$ . The sum over the path intervals can be expressed as the integral over

$\mu$  along the ray path. CT goal is to determine these line integrals exactly. A finite number of measurements of the attenuation coefficient distribution,  $\mu(x,y)$ , is sufficient to compute an image to a good approximation.

When measuring intensities, which is done automatically in modern CT systems, the integral is also computed over all energy intervals as it happens when a polyenergetic beam crosses an inhomogeneous object like the one in case 3 of Figure 2.11 and, as a consequence, the linear attenuation coefficient is energy dependent,  $\mu(E)$ .

In order to compute a good image quality following the theory proposed by Radon (1917), it is necessary to record a high number of attenuation line integral values. Measurements need to be performed in all directions, at least over an angular range of  $180^\circ$  with several narrowly spaced data points for each projection (Kalender, 2011). Modern CT scanners typically measure a fan-beam geometry over an angular range of  $360^\circ$ , aiming to improve image quality.

The set of projection values, so-called the Radon transform of the image, gives the information about the yet unknown distribution of attenuation coefficients,  $\mu(x,y)$ . In order to determine this distribution, it is necessary to carry out an inverse transformation, for which many different approaches are available (Kalender, 2011). Consider, for instance, algebraic reconstruction techniques (ART), usually applied in the first CT scanners. Such techniques consider an  $N \times N$  matrix with  $N^2$  unknown values to be determined by solving  $N_x$  equations, consisting of the measured projections. This is possible if  $N_x$  is equal or larger than  $N^2$ . The simplest case consists of a four-pixel image matrix ( $2 \times 2$ ), two measurements of two projections lead to a four-equation with four unknown values system, which can easily be solved. Similarly, a  $3 \times 3$  matrix with nine unknown values can be solved with twelve measured values (Kalender, 2011).

Modern CT scanners need to deal with much larger matrices. The most utilized reconstruction nowadays is the convolution-backprojection. The starting point is an empty matrix, with pixel values of zero, and each projection value is added to all the picture elements in the computer memory, along with the direction it was measured. However, since each detail in the object contribute to the entire image, the result is an unsharp image. To avoid this, each projection needs to be convolved before back-projection, by applying a proper high pass filter to improve spatial resolution and image noise (Kalender, 2011).

Another approach that can be adopted for CT image reconstruction using cone beam geometry is the FDK (Feldkamp-Davis-Kress) algorithm, which was the first practical

algorithm for three-dimensional reconstruction for cone beam projections from a circular x-ray trajectory (Araújo, 2008; Turbell, 2001). Iterative reconstruction methods are also gaining attention, since all major CT manufacturers have implemented such techniques on their CT scanners as an optional feature. This technique has demonstrated potential dose reduction and better image quality. (Bushberg et al., 2011; Kalender, 2011).

#### 2.4.1. CT number and Hounsfield Unit

As previously explained, the purpose of the CT is to measure and compute the spatial distribution of the linear attenuation coefficient,  $\mu(x,y)$ . Since this quantity is not totally descriptive and strongly dependent on the spectral energy used, it is difficult to compare the results among different CT machines (Kalender, 2011). Therefore, the computed attenuation coefficient is displayed as CT value or CT number, relative to the attenuation of water, which are expressed in Hounsfield units (HU), to honor the CT inventor. For an arbitrary tissue  $T$  with attenuation coefficient  $\mu_T$ , CT value is defined as follows (Kalender, 2011):

$$CT\ value = \frac{\mu_T - \mu_{water}}{\mu_{water}} \times 1000\ HU \quad (2.4)$$

On this scale, water and water-equivalent tissues have the value 0 HU. Air corresponds to -1000 HU since  $\mu_T = \mu_{air}$  equals to zero for a good approximation. These are the fixed points for the CT value scale.

The Hounsfield scale has no upper limit. For medical scanners, a CT number range from - 1024 HU to + 3071 HU is typically provided. As a consequence, 4096 different values are available and 12 bits per pixel are required.

## 2.5. TUBE CURRENT MODULATION (TCM) IN COMPUTED TOMOGRAPHY

The use of CT as a diagnostic procedure is increasing worldwide. As a consequence, radiologists and medical physicists have been concerned about the radiation dose delivered to patients. The goal is to establish adequate image quality with the lowest radiation exposure, according to the ALARA (As Low As Reasonably Achievable) principle (Söderberg & Gunnarsson, 2010).

An important scanning parameter is the tube current, often adjusted by technologists in order to acquire a high quality image. Variations in this adjustment between different CT scanners are related to variation in radiation dose. Automatic exposure control (AEC) or

automatic tube current modulation (ATCM) technique is often applied under this circumstance in order to homogenize scanning techniques and optimize radiation dose. Most of the modern scanners have this technique operating in three dimensions, with the main principle of managing image quality and radiation dose by adapting the tube current to patient's size, shape and attenuation (Kalra, Naz, Rizzo, & Blake, 2005; Reina, 2014; Söderberg & Gunnarsson, 2010).

In the angular modulation (x-y plane), tube current is adjusted during each gantry rotation based on the differences in the attenuation between lateral and anterior-posterior projections. It is useful to be applied in asymmetric body regions, such as the shoulders, where the x-ray beam is less attenuated in the anterior-posterior direction than in the lateral direction. As a consequence, unnecessary x-rays in the anterior-posterior projection are decreased without decreasing image quality (Kalra et al., 2005; Martin & Sookpeng, 2016; Söderberg & Gunnarsson, 2010).

In the longitudinal modulation (z-axis), tube current is adjusted along the scanning direction of the patient for each slice position. This is performed with a single localizer (scanogram) image, from which the system calculates the tube current needed to acquire images with a pre-selected noise level. Unlike the angular modulation, longitudinal modulation adapt the tube current to maintain a user-specified quantum noise in the images along the z-axis. Such modulation aims to manage a similar noise in all images regardless of patient size and anatomy. In the combined modulation, the tube current is adjusted both during the gantry rotation for each slice position (Kalra et al., 2005; Söderberg & Gunnarsson, 2010).

## 2.6. DOSIMETRY IN COMPUTED TOMOGRAPHY

Dosimetry in CT has been the subject of many studies. With the development of the CT technology, scanners have become more complicated and more capable, challenging the accuracy of traditional dosimetry methods (Bushberg et al., 2011). This section provides an overview of different methods and quantities for CT dosimetry.

### 2.6.1. *Computed Tomography Dose Index (CTDI) and Dose Length Product (DLP)*

Computed Tomography Dose Index, so-called CTDI, was first introduced in 1981 by Shope et al. (1981) as a metric to quantify the radiation amount from a CT examination due to adjacent CT scans. It was originally designed as an “index” to distinguish this quantity from the radiation dose absorbed by a patient. This method created an index to reflect the average dose to a cylindrical phantom in the central region of a series of scans (Bushberg et al., 2011;

McCollough et al., 2011). Since its implementation, several enhancements and modifications to this concept have been applied to make it a more accurate dosimetry method. Some variations from the original concept include the  $CTDI_{100}$ ,  $CTDI_w$ ,  $CTDI_{vol}$ , which are measured in mGy, and the Dose-Length Product, so called DLP, which is measured in mGy.cm (AAPM, 2008; Bushberg et al., 2011).

CTDI is measured with a pencil ionization chamber placed in the central hole of a 16-cm diameter head phantom or a 32-cm diameter body phantom, which are constructed with polymethyl methacrylate (PMMA) (Figure 2.12). It is calculated according to

$$CTDI = \frac{1}{NT} \int_{-\infty}^{+\infty} D(z) dz, \quad (2.5)$$

where  $D(z)$  is the radiation dose profile along the z-axis,  $N$  is the number of tomographic images in a single axial scan, which is equal to the number of data channels used in the scan,  $T$  is the width of the tomographic section along the z-axis and  $NT$  is the collimation width.



Figure 2.12 – Head (16-cm diameter) and body (32-cm diameter) PMMA phantoms used to measure CTDI. Note: Reprinted from <<http://www.universalmedicalinc.com/ct-dose-phantom.html>>.

$CTDI_{100}$  represents the accumulated dose at the center of a 100-mm scan, underestimating doses for longer scan lengths. In this case, the integration of the radiation dose profile is performed over 100 mm integration limits, from -50 mm to +50 mm, which corresponds to a 100-mm length of the commercially available pencil ionization chamber. The value measured by the ionization chamber represents the air kerma over the chamber length and, therefore,  $CTDI_{100}$  is calculated according to (AAPM, 2008):

$$CTDI_{100} = \frac{f \times 100 \text{ mm} \times R}{NT} \quad (2.6)$$

where  $f$  is a calibration factor to convert the reading of the ionization chamber to air kerma (mGy),  $R$  is the reading of the ionization chamber and 100 mm is the length of the integral along z-axis.

CTDI varies across the field of view (FOV). For body CT imaging, for instance, the CTDI is higher at the surface (periphery) than at the center (central) of the FOV. Therefore, the average CTDI across the FOV is estimated by the weighted CTDI ( $CTDI_w$ ) (Leitz, Axelsson, & Szendro, 1995):

$$CTDI_w = \frac{1}{3}CTDI_{100,c} + \frac{2}{3}CTDI_{100,p} \quad (2.7)$$

To represent dose for a specific protocol that consists of a series of scans, it is necessary to consider gaps or overlaps between the x-ray beams from consecutive rotations of the x-ray source. This is possible with an index known as Volume CTDI<sub>w</sub> ( $CTDI_{vol}$ ), which is defined as (AAPM, 2008):

$$CTDI_{vol} = \frac{1}{pitch} \times CTDI_w \quad (2.8)$$

$CTDI_{vol}$  is the estimate of the average absorbed radiation dose over the x, y, and z directions standardized with respect to the integration limits  $\pm 50$  mm. This index provides a single CT dose parameter based on a quantity that represents the average dose within the scan volume for a standardized phantom.  $CTDI_{vol}$  is a useful tool because it takes into account protocol-specific information such as pitch. Most of the modern CT scanners display the  $CTDI_{vol}$  value in the end of the examination (AAPM, 2008).

It is important to note that  $CTDI_{vol}$  does not represent the average dose for objects of different size, shape or attenuation. Furthermore, it does not indicate the total energy deposited into the scan volume, since it is independent of the scan length, which means that the  $CTDI_{vol}$  value remains unchanged whether the scan coverage is 10 cm or 100 cm (AAPM, 2008; Boone, 2007).

To provide a better estimative of the overall energy delivered by a given scan protocol, the Dose-Length Product (DLP) quantity is used, which is the absorbed dose integrated along the scan length (AAPM, 2008; Jessen et al., 2000):

$$DLP(mGy.cm) = CTDI_{vol}(mGy) \times scan\ length\ (cm) \quad (2.9)$$

Despite not providing a dose value, DLP is a useful quantity of interest. It is notably useful to compare dose levels and it became accepted through the establishment of diagnostic reference levels (DRL) (AAPM, 2008; Jessen et al., 2000; Kalender, 2011, 2014).

### 2.6.2. Size Specific Dose Estimates (SSDE)

As an attempt to consider the patient size in the dose indexes previously described, the American Association of Physicist in Medicine (AAPM) proposed the quantity size-specific dose estimates (SSDE) after the work of a task group organized by a number of researchers (AAPM, 2011b). The objective of this task group was to provide conversion factors according to the patient anatomy to be applied to the  $CTDI_{vol}$  associated to a patient-specific exam. This is particularly important for pediatric and small adult patients since, by the dependence of dose levels on phantom diameters, doses will be lower for larger patients than the  $CTDI_{vol}$  value measured in a 32 cm diameter phantom and higher for small patients (AAPM, 2011b; Kalender, 2014).

As it is detailed described in the AAPM Task Group Report 204, SSDE is estimated with the anthropometric parameter ‘patient effective diameter’ (Kalender, 2014). The patient effective diameter represents the diameter of the patient at a given location along the z-axis of the patient, assuming the patient has a circular cross section. Then, the effective diameter ( $EF$ ) is calculated as follows:

$$EF = \sqrt{AP \times LAT} \quad (2.10)$$

Based on the effective diameter of the patient, conversion factors ( $f$ ) to adapt the  $CTDI_{vol}$  value to SSDE were determined. This was performed by combining several works developed by a number of authors, including Monte Carlo voxelized phantoms, Monte Carlo Mathematical cylinders, physical anthropomorphic phantoms and cylindrical PMMA phantoms (AAPM,

2011b), which resulted in a table of conversion factors to be applied for each CTDI PMMA phantom (head or body). Thus:

$$SSDE = f \times CTDI_{vol}. \quad (2.11)$$

Despite still having deficiencies, especially related to the determination of patient diameters and body size (Kalender, 2014; Karmazyn, Ai, Klahr, Ouyang, & Jennings, 2016), the concept of SSDE is becoming increasingly accepted as a CT scan dose estimate parameter (Franck et al., 2016; Karmazyn et al., 2016; Leng et al., 2015; Strauss, 2014b).

### 2.6.3. Diagnostic Reference Level (DRL)

Diagnostic Reference Levels, so-called DRL, were first proposed in the 1990s by the International Commission on Radiological Protection (ICRP, 2000) as a form of investigation level using easily measured dose quantities. The following points should be highlighted concerning the definition and application of DRLs (IAEA, 2014).

- The use of DRL is mandatory, but a given DRL value is not a dose limit.
- DRLs are intended to identify high levels of radiation dose to patients.
- DRLs are given in easily and reproducible dose metrics.
- The selection of National DRL is performed by professional or governmental bodies and it is specific to a country or region.
- The objective of DRL is the comparison between the numerical value of the DRL, derived from relevant regional or national data, and the mean value observed in practice for a suitable reference group of patients (ICRP, 2000).
- DRLs are not fixed. They are expected to change over a period of time according to technological advances and optimization.
- DRLs for CT are mainly indicated by the dose descriptors DLP and  $CTDI_{vol}$ , according to the standard value provided by CT machines (Vassileva et al., 2015).

The List of Quality Criteria provided by the set of European guidelines on Quality Criteria for Computed Tomography (Jessen et al., 2000) intend to avoid unnecessary exposure. This document states that DRLs are indicated for general types of examination to promote strategies for optimizing patient protection. Therefore, DRLs should not be applied locally on an individual patient, but to the mean doses reported for representative groups of patients (Jessen et al., 2000). The European Guidelines on DRL for Pediatric Imaging (European Society

of Radiology, 2015), for instance, highlight that the comparison of patient data with DRLs should be performed by considering at least 10 patients for each age or weight group from a group or institution.

#### *2.6.4. Evaluation of Organ Doses*

Although CTDI and DLP metrics are well established nowadays, these quantities provide the information about how the machine was operated (McCollough et al., 2011). Such technical dose information is generally available and required by law, but it is much more complicated to obtain information on the patient dose from any arbitrary examination since it depends on a number of parameters, besides information of patient size and anatomical region scanned (Kalender, 2011). Therefore, CTDI values are not patient dose estimates (Kalender, 2011).

Effective dose is another parameter commonly used as a tool for quantifying radiation doses from diagnostic procedures. This quantity is proposed on the ICRP Publication 103 (2007) and it is based on multiplicative weight factors, derived from a large number of individuals, applied to fundamental quantities such as absorbed dose. This same publication states that the effective dose is determined for a reference person instead of an individual. In addition, ICRP Publication 116 (2010) states that the weighted sum to obtain the effective dose should not be used for individuals, but for population of patients. Aiming to clarify the concept and use of this quantity, Costa et al. (2016) performed a review and presented arguments to determine the correct use and implementation of the effective dose, which, therefore, cannot be used as patient-specific dose estimate.

Estimation of organ dose values is not a trivial task. In general, three approaches have been adopted over the past decades: direct measurements with different kinds of dosimeters, anthropomorphic phantoms and postmortem subjects, calculations using Monte Carlo methods and biological dosimetry based on blood samples (Kalender, 2011). All of these techniques provide advantages and disadvantages and a number of papers can be found in the literature.

Zhang et al. (2013), for instance, proposed an experimental methodology for acquiring densely sampled organ dose map for CT applications by applying optically stimulated luminescent (OSL) dosimeters in an adult anthropomorphic phantom. These authors aimed to experimentally acquire dose maps in organs in order to obtain detailed and accurate dose distribution information within the scanned volume due to a routine chest protocol. The authors evaluated the influence of tube current modulation in the organ dose distribution.

In a similar approach, dosimeters can be placed inside post-mortem subjects. An advantage of this method is the possibility of evaluating organ doses in several anatomical configurations, which is more difficult when using anthropomorphic phantoms. However, this method is difficult to perform and it is hard to measure the dose for complete organs, necessary to determine the average values (Kalender, 2011). Griglock et al. (2015) and Sinclair et al. (2015) proposed an experimental methodology that allows direct measurements of organ doses from CT examinations of postmortem subjects. To do so, a routine chest-abdomen-pelvis protocol was applied to eight female postmortem subjects and organ doses were evaluated. Additionally, the authors determined the relationship among the measured organ doses, body mass index, effective diameter and  $CTDI_{vol}$ . As a result, the measured organ doses provided more accurate estimates than other metrics such as the SSDE.

Dose calculations by Monte Carlo methods are more flexible, demand less effort and can provide accurate 3D dose distributions (Kalender, 2011). Software developed for such calculations are based on exact models of the CT scanners, CT scan technique and on mathematical phantoms or the actual CT image data sets, so-called voxelized phantoms. They simulate the radiation transport through the patient, which allows precise and specific estimates that generate an enormous database. All data are later presented to the user as a graphical interface to calculate organ doses and effective doses, such as the ImPACT spreadsheets (ImPACT CT Patient Dosimetry Calculator) (Lewis, 2004), CTExpo (Stamm & Nagel, 2002), and, more recently, the National Cancer Institute Dosimetry System for CT, so-called NCICT (Lee, Kim, Bolch, Moroz, & Folio, 2015).

## 2.7. THERMOLUMINESCENT AND OPTICALLY STIMULATED LUMINESCENT DOSIMETRY

Thermoluminescent dosimeters have been widely used in many different applications, such as medical dosimetry, geological age determination and solid-state defect structure analysis. The first application of this technique to dosimetry was in 1953, when Lithium Fluoride (LiF) thermoluminescent pallets were used at the Hospital of Oak Ridge Institute of Nuclear Studies to estimate the internal radiation dose delivered to patients due to a cancer treatment (Daniels, Boyd, & Saunders, 1953). This material has been routinely applied in medical dosimetry because of its properties. Its effective atomic number ( $Z_{eff} = 8.14$ ) is similar to the soft tissue value ( $Z_{eff} = 7.42$ ), which makes this material almost tissue-equivalent.

Therefore, it is not necessary to correct for the energy dependence in the energy range of radiology and radiotherapy (Daniels et al., 1953; McKeever, 1988).

Optically Stimulated Luminescent dosimeters were first suggested as a radiation dosimetry tool in the 1950s, but the acceptance of the OSL as a dosimetry tool began after the application of this technique in geological dating of sediments (Huntley, Godfrey-Smith, & Thewalt, 1985). In addition, in the 1990s a carbon doped aluminum oxide dosimeter,  $\text{Al}_2\text{O}_3:\text{C}$ , was initially developed to be used as thermoluminescent material (Akselrod, Kortov, Kravetsky, & Gotlib, 1990) but proved to be highly sensitive to light. Later, this material emerged as the most popular OSL radiation dosimeter and it is now commercialized by Landauer, Inc. (Landauer, Inc., Glenwood, USA)<sup>d</sup> (Yukihara & McKeever, 2011). This material, however, has an effective atomic number of 11.28 (Bos, 2001), which causes an over-response to low-energy x-rays, typically found in radiology, with respect to tissue (Mobit, Agyingi, & Sandison, 2006; Perks, Yahnke, & Million, 2008).

Thermoluminescence (TL) is a luminescence phenomenon that occurs when a semiconductor or an insulator is thermally stimulated. In simple terms, it is the thermally stimulated emission of light after the previous absorption of energy due to the exposure to ionizing radiation (Bos, 2006; McKeever, 1988). Optically Stimulated Luminescence (OSL) is another class of measurements known as stimulated phenomena. In simple terms, it is the luminescence emitted from a semiconductor or an insulator after its exposure to ionizing radiation, during exposure to light (Bøtter-Jensen, McKeever, & Wintle, 2003). Thus, such materials store the energy absorbed during the exposure to ionizing radiation, which can be released when the material is heated or optically stimulated. An important issue to highlight is that, once heated to emit light, TL material cannot exhibit thermoluminescence unless re-exposed to ionizing radiation (McKeever, 1988). Unlike TL materials, however, the high sensitivity of OSL detectors allows multiple reading, since sometimes it is not necessary to stimulate all the trapped charges to read a sufficient luminescence signal (Bøtter-Jensen et al., 2003).

TL and OSL properties can be explained with the energy band theory of solids, according to Figure 2.13. Ideally, in a semiconductor or insulator crystal (TL material), most of the electrons populate the valence band (VB). When this material absorbs an amount of ionizing radiation, the electrons are excited from the valence band to the conduction band (CB), leaving

---

<sup>d</sup> See [www.landauer.com](http://www.landauer.com).

holes in the VB. However, if any structural defects occur in the crystal, the electrons and the holes can be trapped in the forbidden energy band gap existing between VB and CB (Figure 2.13-i). These populations of trapped electron and holes represent a metastable state, which can exist for an indefinite period (Figure 2.13-ii). In these materials, the trapped electrons have a probability to be released back to the CB that depends on the temperature and on the activation energy<sup>e</sup>. Therefore, by thermal or optical stimulation of the sample, the electrons can be released to the CB with a probability of recombining with the holes at some sites, called the recombination centers. A recombination center is a luminescent center that is excited to a higher energy level in the event of the electron/hole recombination. When these excited luminescence centers return to the ground state, a light quanta, that is proportional to the radiation dose absorbed by the material, is emitted (Figure 2.13-iii) (Akselrod, Bøtter-Jensen, & McKeever, 2006; Bos, 2006; Bøtter-Jensen et al., 2003; Furetta, 2010; McKeever, 1988; Yukihiro & McKeever, 2011).

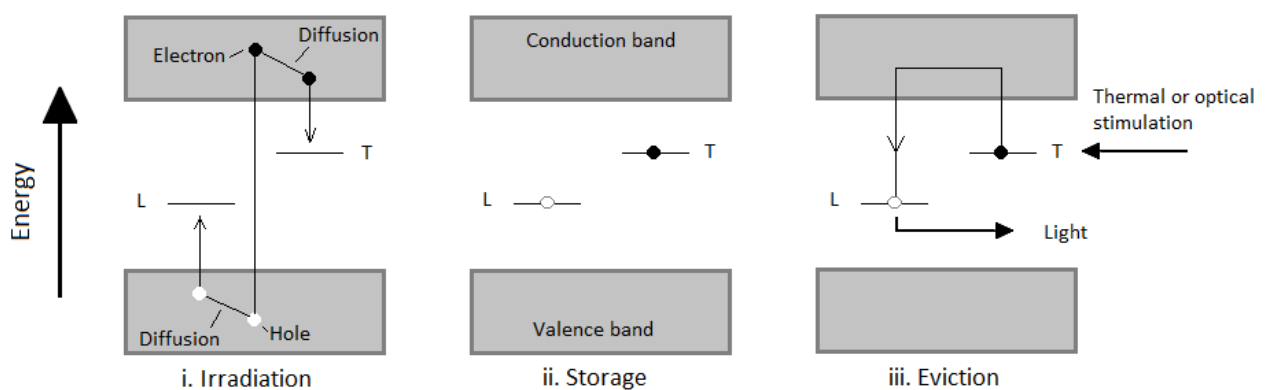


Figure 2.13 – Energy level representation of the TL and OSL processes. i. Trapping of the electrons and holes within the crystal lattice due to the exposure to ionizing radiation, where L and T are the hole and electron defects, respectively. ii. Electrons and holes trapped in a metastable state. iii. Thermal or optical stimulation results in the release of the trapped electrons, which can recombine with holes at the recombination centers and emit light. Note: Adapted from Aitken (1998).

In a simple model of the OSL process, it is demonstrated that the OSL intensity decays exponentially during stimulation. Consider  $n$  to be the concentration of trapped electrons and  $p$  the probability per unit time of the trapped electrons to be released back to the conduction band under optical stimulation. In this situation,  $n$  will change according to (Yukihiro & McKeever, 2011).

<sup>e</sup> The activation energy is the energy needed to release an electron from the trap into the conduction band (Bos, 2006).

$$\frac{dn}{dt} = -np. \quad (2.12)$$

The solution of this equation is an exponential function, which shows that the concentration of trapped electrons,  $n$ , decays exponentially with the stimulation time:

$$n(t) = n_0 e^{-pt}, \quad (2.13)$$

where  $n_0 = n(0)$  is the initial concentration of trapped charges. If all stimulated electrons recombine immediately, the intensity of light emitted is proportional to the rate of the trapped electrons release,  $\frac{dn}{dt}$ . Therefore:

$$I_{OSL}(t) \propto \left| \frac{dn}{dt} \right| = n_0 p e^{-pt}. \quad (2.14)$$

### 3. MATERIALS AND METHODS

#### 3.1. MATERIALS

##### 3.1.1. *Anthropomorphic phantoms*

Physical phantoms are mostly used for image quality assessment or radiation dosimetry studies. Many of these applications do not require any information concerning the anatomical properties of the human body. For other applications, such as the evaluation of the image quality and the organ doses evaluation, anatomical information is required (Xu & Eckerman, 2009). Anthropomorphic phantoms manufactured with tissue-equivalent materials have been extensively used to provide a physical representation of the human body's anatomy (Winslow, Hyer, Fisher, Tien, & Hintenlang, 2009).

There are two important requirements regarding the construction of these objects in order to accurately assess the organ doses in a clinical examination (Xu & Eckerman, 2009):

1. The correct positioning of the target organs inside the anthropomorphic phantom.
2. The precise reproduction of the attenuating and scattering radiation properties by choosing proper tissue-equivalent materials (ICRU, 1989; Xu & Eckerman, 2009).

Recently, anthropomorphic phantoms have been applied for dosimetry purposes in computed tomography procedures in a variety of applications using different kind of radiation detectors (Costa, 2014). In the present work, two anthropomorphic phantoms were used: the RANDO phantom (The Phantom Laboratory, NY, USA), which simulates the anatomical characteristics of the Reference Man (ICRP, 2002), and the CIRS ATOM® dosimetry verification phantom, model 705 (CIRS, Inc., VA, USA), which simulates a pediatric 5-year old patient. The main characteristics of these objects are described below.

##### 3.1.1.1. The RANDO Phantom

The RANDO phantom (The Phantom Laboratory, NY, USA) has been used for more than 30 years (Radiology Support Devices, 2014) and it is the most applied anatomical dosimetry phantom (Xu & Eckerman, 2009). Traditionally, it has been used for mapping dose distribution, which is useful, for instance, for evaluation of the patient radiotherapy treatment, quality assurance of planning systems and research (The Phantom Laboratory, 2012).

The RANDO phantom used in the present work represents a 175 cm tall and 73.5 kg adult man. It was constructed with human skeleton inserted in soft tissue-equivalent material, which simulates muscle tissue with randomly distributed fat (The Phantom Laboratory, 2012).

It is constructed with a durable material that has a density of  $0.985 \text{ g/cm}^3$  and effective atomic number ( $Z_{\text{eff}}$ ) of 7.30 (Archer, Glaze, North, & Bushong, 1977). The lungs are molded to fit the contours of the rib cage and they have the same effective atomic number as the soft tissue ( $Z_{\text{eff}} = 7.30$ ), with a density of  $0.32 \text{ g/cm}^3$ , which simulates the lungs in a median respiratory state (Archer et al., 1977; The Phantom Laboratory, 2012).

This phantom is sliced in 36 sections, numbered from 0 to 35 (Figure 3.1). Slices 0 to 34 are 25 mm in thickness and slice 35 is the pelvic floor, which is approximately 9 cm in thickness. In each slice there are drilled holes that enable the insertion of different types of dosimeters (The Phantom Laboratory, 2012).



Figure 3.1 – Left: The slices of the RANDO phantom (The Phantom Laboratory, 2012)<sup>f</sup>. Right: The phantom prepared to be irradiated, with all the slices arranged.

#### 3.1.1.2. The CIRS ATOM Family of dosimetry phantoms

The ATOM® phantoms manufactured by the *Computerized Imaging Reference System* (CIRS, Inc., VA, USA) are designed to investigate organ doses, whole body effective dose and the delivery of therapeutic radiation doses. ATOM is the only line of dosimetry phantoms that ranges in sizes from newborn to adult. Six models are available: newborn, 1-year, 5-year and 10 year old pediatric phantoms, and two adults (male and female phantoms) (CIRS, 2013).

In the present work, a pediatric phantom, model 705, was used. It represents a 5-year old, 110 cm tall and 19 kg pediatric patient. CIRS uses a synthetic bone material based on the appropriate bone composition typical of each age. The physical density of the bone material used in this phantom is  $1.52 \text{ g/cm}^3$ . The phantoms are constructed with CIRS proprietary tissue

<sup>f</sup> The Phantom Laboratory. RANDO® Phantom Sections. Available at: < [http://phantomlab.client-proof.com/images/photos/p\\_rando2\\_lg.jpg](http://phantomlab.client-proof.com/images/photos/p_rando2_lg.jpg)>. Accessed: Jan. 2017.

equivalent materials, used to represent soft tissue, bone, cartilage, spinal cord, spinal disks, lungs, and brain. The lung tissue is constructed with a low-density inhale formulation equivalent to  $0.21 \text{ g/cm}^3$  and effective atomic number ( $Z_{eff}$ ) of 7.38. The soft tissue has a density of  $1.055 \text{ g/cm}^3$  and effective atomic number of 7.15. (CIRS, 2013; Xu & Eckerman, 2009).

This phantom is sliced in 26 sections, numbered from 1 to 26, that are 25 mm in thickness (Figure 3.2). In each slice there are drilled holes that enable the insertion of dosimeters (CIRS, 2013).



Figure 3.2 - Left: The 10<sup>th</sup> slice of the CIRS ATOM pediatric phantom, presenting the different tissue equivalent materials used in its manufacture. Right: The phantom prepared to be irradiated.

### 3.1.2. *Risϕ TL/OSL reader*

An automated Risϕ TL/OSL reader model DA-20 (DTU Nutech. Inc., Roskilde, Denmark), was used to read the information stored in the dosimeters after each exposure (Figure 3.3). This equipment operates with a sample carousel with 48 stainless steel cups, which rests on a motor driven turntable that enables the carousel to rotate. This rotation is computer controlled, so that each sample is individually read according to a pre-set configuration (DTU Nutech, 2015). This reader works with detection and stimulation systems. The light detection system consists of a photomultiplier tube (PMT), which captures the light emitted by the dosimeters, along with filters, which keep the scattered light from reaching the PMT and define the detection spectral window. The luminescence stimulation system consists of both a heating element that is used for TL measurements and a light stimulation system that is used for OSL measurements (DTU Nutech, 2015).

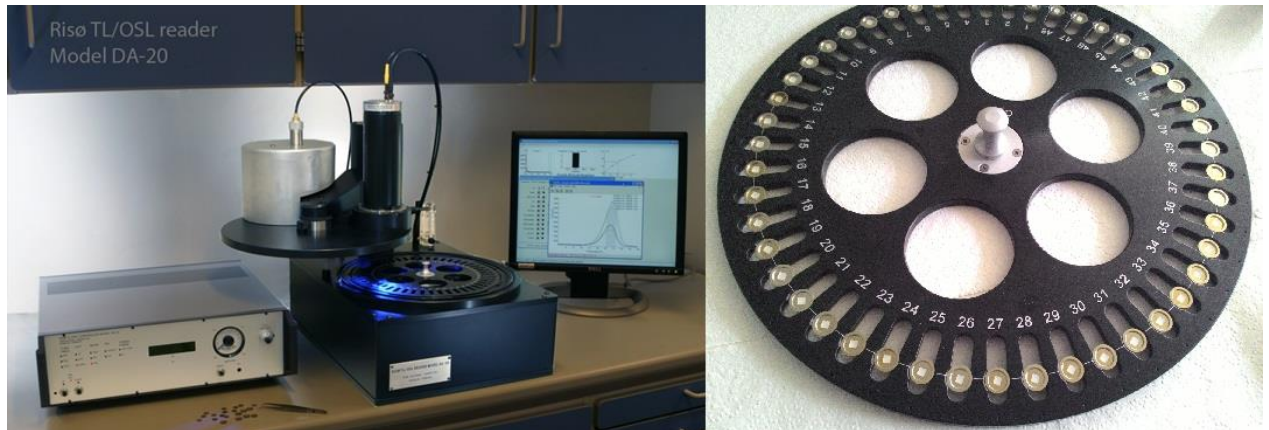


Figure 3.3 – Left: The Risø TL/OSL Reader model DA-20 (DTU Nutech. Inc., Roskilde, Denmark). Note: Reprinted from DTU Nutech (2015). Right: 48-position sample carousel.

In order to verify the reproducibility of the detection system, the reader includes a reference light source, which, according to the manufacturer, is the blue calibration LED (DTU Nutech, 2015). This reference source has two major purposes. The first one is to check the applicability of the filter in front of the PMT before starting the measurements, in order to prevent the PMT from possible damages. The other application is to control the stability of the detection system, especially when the blue filter is applied in TL measurements. It also provides evidence whether the detection filters or the interface quartz-filter were contaminated from one measurement to another (DTU Nutech, 2015).

Moreover, the reader includes a 1.48 GBq  $^{90}\text{Sr}/^{90}\text{Y}$  beta source, which emits beta particles with 2.27 MeV of maximum energy, to irradiate the samples. The irradiations are software controlled with a minimum of 1 second of irradiation per sample (DTU Nutech, 2015). This technique can be applied to the OSL dosimeters so that their responses to the beta radiation ( $S_{\beta}$ ) is used to individually normalize the OSL responses to the x-ray radiation ( $S_{x\text{-ray}}$ ) and, therefore, decrease the uncertainties (Yukihara & McKeever, 2008) ( $S = S_{\beta} / S_{x\text{-ray}}$  per dosimeter).

### 3.1.3. Dosimeters

#### 3.1.3.1. Thermoluminescent Dosimeters (TLDs)

Lithium Fluoride doped with Magnesium and Titanium (LiF:Mg, Ti) thermoluminescent dosimeters TLD-100 (Harshaw Chemical Company, OH, USA) were used in the present work. A batch of 481 dosimeters in the format of  $3 \times 3 \times 1 \text{ mm}^3$  was previously

selected considering the homogeneity of their responses to the same irradiation technique (Martins, 2015) and was applied in this study.

*a) TLD Annealing*

The procedure called annealing is a thermal treatment applied to thermoluminescent materials in order to erase the effects from previous irradiations. The annealing stabilizes sensitivity and background of the dosimeters so that their properties remain invariable along the usage (Furetta, 2008).

Therefore, before each exposure, the TLDs were thermally treated as follows: first, they were placed in an aluminum recipient inside an oven at constant temperature of 400°C for 60 minutes; after that, they were removed from the oven and left to cool at room temperature for 10 minutes; next, they were placed again inside the oven at constant temperature of 100°C for 120 minutes; finally, after cooling at room temperature, the dosimeters were ready to undergo a subsequent irradiation (Furetta, 2008).

*b) TLD Data Reading*

In order to read the information stored in the TLDs, the heating system of the automated Risø TL/OSL reader model DA-20, (DTU Nutech. Inc., Roskilde, Denmark), was used as the luminescence stimulator (Section 3.1.2). The filter applied in this measurement was the blue filter pack, which consists of the Schott BG-39 (2 mm in thickness and 45 mm in diameter) along with the Schott BG3 filters (3 mm in thickness and 45 mm in diameter) (DTU Nutech, 2015). Dosimeters were placed in the carousel and they were individually heated from 0°C to 350°C at a constant rate of 10°C per second.

As described in Section 3.1.2, light emitted by the dosimeter is captured by the PMT. This captured light is converted to a digital signal and an integrated software presents the user a plot of the photon counts captured by the PMT per temperature, which is called TL curve. Therefore, the TL signal is extracted by the numerical integration of the TL curve up until 350°C, which is directly proportional to the energy deposited by ionizing radiation in the dosimeter (Bushong, 2013). Figure 3.4 presents an example of a TL curve obtained in one set of measurements with the computed tomography scanner. This plot and the integrals of the curves were performed with the software Origin® 2016 (OriginLab Co., MA, USA).

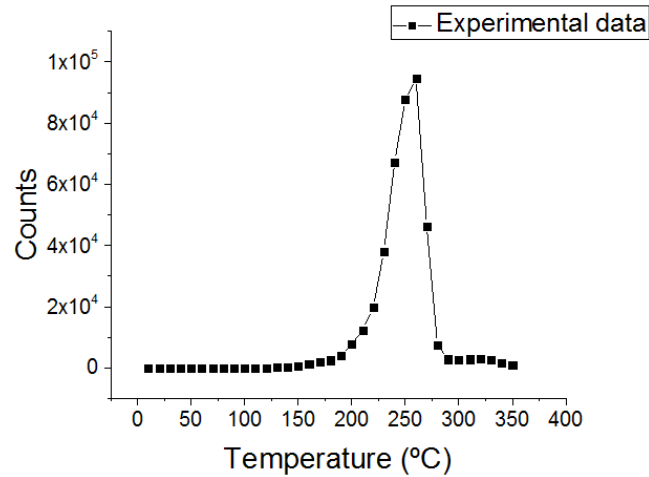


Figure 3.4 – Example of a TL curve obtained with the irradiation of one TLD-100 chip (Harshaw Chemical Company, OH, USA) with a 64-slice CT Scanner.

### 3.1.3.2. Optically Stimulated Luminescent Dosimeters (OSLD)

The commercial  $\text{Al}_2\text{O}_3:\text{C}$  OSL dosimeter (OSLD) Landauer Luxel<sup>TM</sup> tape (Landauer, Inc., Glenwood, USA) was used in the present work. This dosimeter is produced with carbon-doped aluminum oxide crystals that are converted into powder and used to produce long plastic tapes with 0.3 mm in thickness (Yukihara & McKeever, 2008). This tape can be fractionated in the desired size and shape.

In the present study the Landauer Luxel<sup>TM</sup> tape (Landauer, Inc., Glenwood, USA) was fractionated with a scissor and a circular-shape paper punch into disks measuring 3 mm in diameter, according to Figure 3.5.



Figure 3.5 - Left: OSL tape. Right: Fractionated dosimeters (3 mm in diameter and 0.3 mm in thickness).

A batch of dosimeters placed in an aluminum recipient, fractionated as previously described, and 5 samples along with a ruler (cm/mm) are presented in Figure 3.6 to illustrate the shape and size of the dosimeters.

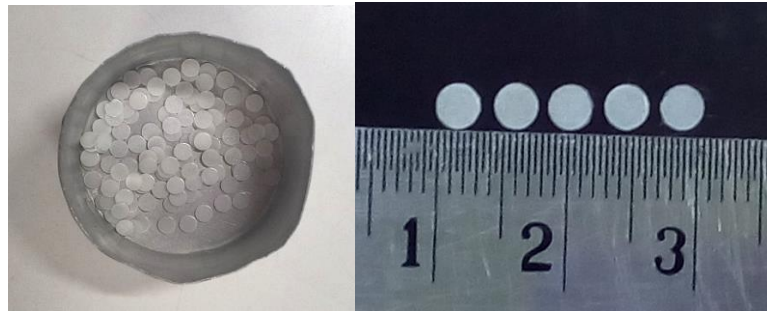


Figure 3.6 - Left: a batch of OSLD disks placed in an aluminum recipient. Right: 5 samples of OSLD disks along with a ruler to visualize their shape and size.

*a) TLD and OSLD holders*

A light-tight envelope made of Polyvinyl Chloride (PVC) was used in the present work. These envelopes could accommodate up to six dosimeters and were applied to perform the characterization of the OSLDs.

Another dosimeter holder was especially designed for this study in order to fit the drilled holes in the slices of the anthropomorphic phantoms. Martins (2015) developed this kind of holder in a previous work and they were manufactured at the Mechanical Workshop of the Institute of Physics of the University of São Paulo. The dosimeter holders are cylinders designed to accommodate up to five TLDs along with four OSLDs so that when inserted inside the slices of the phantoms, dosimeters are positioned in the midsection of the slices (Archer et al., 1977). The material used for manufacturing these holders is a light-tight Polyoxymethylene, which has an effective atomic number close to the effective atomic number of the soft tissue of the RANDO phantom (Martins, 2015).

Dosimeter holders designed for the CIRS ATOM pediatric phantom and for the RANDO phantom are different in their diameters: holders for the RANDO phantom are 5.9 mm in diameter, and for the CIRS ATOM phantom are 4.9 mm. The technical draft of the RANDO phantom dosimeter holder as previously developed by Martins (2015) and the picture of a CIRS ATOM phantom dosimeter holder are presented in Figure 3.7, along with a TLD chip and an OSLD disk.

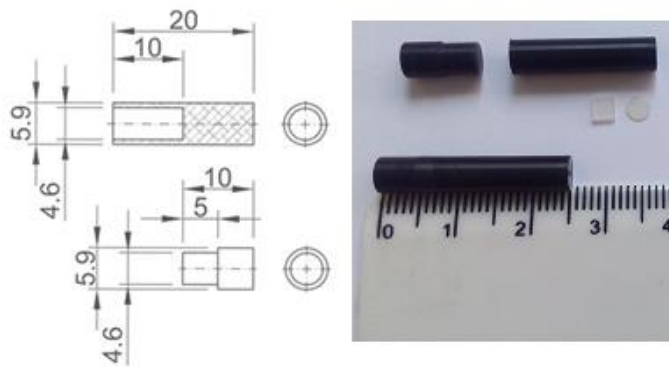


Figure 3.7 – Left: Technical draft (in mm) of the dosimeter holder designed for the RANDO phantom (Martins, 2015). Right: a picture of the dosimeter holder designed for the CIRS ATOM phantom along with a TLD chip and a 3 mm OSLD.

### *b) OSLD Bleaching*

Bleaching is an optical treatment applied to the OSLDs in order to erase the radiation dose stored in the dosimeter. The bleaching process is able to empty the main dosimetric traps, which are related to the main OSL signal (Yukihara & McKeever, 2011). Therefore, before each exposure, the OSL detectors were optically treated for eight hours under a fluorescent light consisting of four tungsten white light bulbs (ATEK Digilight, ATEK, Brazil).

### *c) OSLD Data Reading*

In order to extract the information stored in the OSLDs, the optical stimulation system of the automated Risø TL/OSL reader model DA-20, (DTU Nutech. Inc., Roskilde, Denmark) was used as the luminescence stimulator (Section 3.1.2). An ultra-violet transmitting broad-band pass filter (Hoya U-340, 7.5 mm in thickness and 45 mm in diameter) was applied in this study (DTU Nutech, 2015). A 10 mm aperture was applied in order to limit the amount of light arriving at the PMT. Dosimeters were placed on the 48-sample carousel and a constant blue light stimulation, with a peak emission at 470 nm, which depletes the electron traps and produces an exponentially decaying signal, was applied to each sample (continuous wave/ CW mode) (DTU Nutech, 2015). Stimulation was performed up until 70 s or 90 s,

The OSL curve is presented to the user as a histogram of the photon counts per time. The OSL signal can be extracted by the initial signal, which is the numerical integration up until the first second, for instance, or by the total OSL area, which is the numerical integration of the entire OSL curve. Figure 3.8 presents an example of an OSL curve resulting from a measurement with an x-ray tube. This plot was performed with the software Origin® 2016 (OriginLab Co., MA, USA).

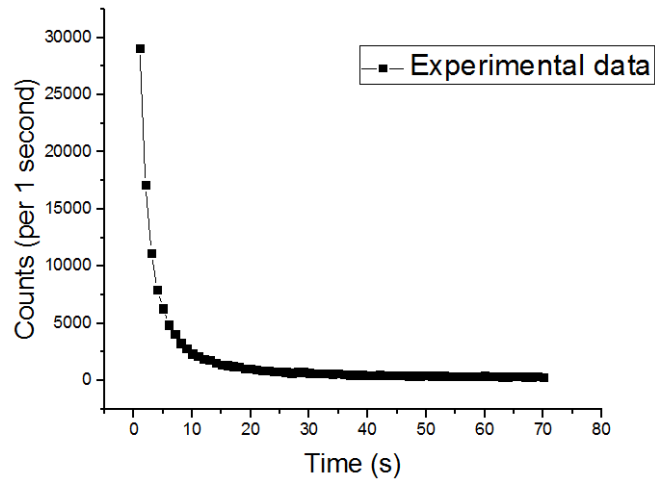


Figure 3.8 - Example of an OSL curve obtained after the irradiation of one Al<sub>2</sub>O<sub>3</sub>:C OSL Landauer Luxel™ dosimeter (Landauer, Inc., Glenwood, USA) with an x-ray tube.

After performing the readout of the dosimeters, they were irradiated with the <sup>90</sup>Sr/<sup>90</sup>Y beta radiation inside the reader for two seconds (Section 3.1.2). The reading process described above was then repeated, so that the dosimeter responses to beta radiation were used to individually normalize the OSL responses to the x-ray radiation, as described in Section 3.1.2. This procedure was applied to some set of measurements in order to assess the uncertainties associated with this method.

#### 3.1.4. Irradiation instruments

An industrial x-ray tube MCN 421 (Philips, Germany) with stationary Tungsten target was used to irradiate the dosimeters. This x-ray tube is powered by a constant-potential generator and operates with tube voltage that ranges from 40 to 150 kV (Lopez Gonzales, Tomal, & Costa, 2015). RQR and RQT x-ray standard beams (IAEA, 2007; IEC, 2005) were validated in this equipment and used during the procedures described in the present study. Ionization chambers were applied to measure the air kerma according to each test (Section 3.2.1): a 30 cc ionization chamber (IC), model 23361-0576, coupled to an electrometer Unidos E (PTW, Freiburg, Germany), and a 0.6 cc ionization chamber, model 10X5-0.6, coupled to an electrometer model 9010 (Radcal Corporation, Monrovia, CA, USA), both calibrated by an SSDL, were used in the measurements performed with this equipment.

A Philips Brilliance 64 CT scanner (Philips, Germany) was used to irradiate the phantoms and the dosimeters. Such equipment presents a 64-slice configuration and, thus, it is

faster than many similar machines. Its MRC x-ray tube was able to reduce time between sequences (Philips, 2004-2017). The CT scanner used in the present work is property of the Institute of Radiology of the School of Medicine of the University of São Paulo (InRad/FMUSP). The 0.6 cc ionization chamber model 10X5-0.6, coupled to an electrometer model 9010 (Radcal Corporation, Monrovia, CA, USA), was used in the measurements with this equipment. This chamber is adopted for dose measurements in multi-slice computed tomography scanners (AAPM, 2010; Radcal, 2013). Irradiation parameters are described in Section 3.2.4.

## 3.2. METHODS

### 3.2.1. OSLD Characterization

The following characteristics of OSLDs were investigated in the present study: batch homogeneity, energy response, linearity of dose response, reproducibility, reusability and effect of uncertainties with the normalization of OSL signals per their response to beta radiation. The material used was the Al<sub>2</sub>O<sub>3</sub>:C OSLD Landauer Luxel™ tape (Landauer, Inc., Glenwood, USA) fractionated into disks measuring 3 mm in diameter, as previously described (Section 3.1.3). A group of LiF:Mg,Ti TLD chips was simultaneously irradiated in a set of control measurements for comparison of results. Irradiations were performed using the constant potential x-ray tube MCN 421 (Philips, Germany) (Section 3.1.4). The clinical 64-slice CT scanner Brilliance 64 (Philips, Germany), from InRad/FMUSP (Section 3.1.4), was used in an additional set of measurements. Experimental setups are described below.

The 30 cc ionization chamber (IC), model 23361-0576, coupled to an electrometer Unidos E, was positioned alongside the OSLDs, five meters away from the focal spot of the MCN 421 x-ray tube (Figure 3.9). Uniformity of the x-ray field was tested at this distance by measuring the air kerma in distinct positions and calculating the coefficient of variation (CV)<sup>§</sup> of the measurements, which was 0.6%. Therefore, dosimeters placed at this distance from the focal spot of the x-ray tube were going to be irradiated under similar conditions.

---

<sup>§</sup> The coefficient of variation (CV) if defined as the ratio of the standard deviation ( $\sigma$ ) to the mean value ( $\mu$ ).

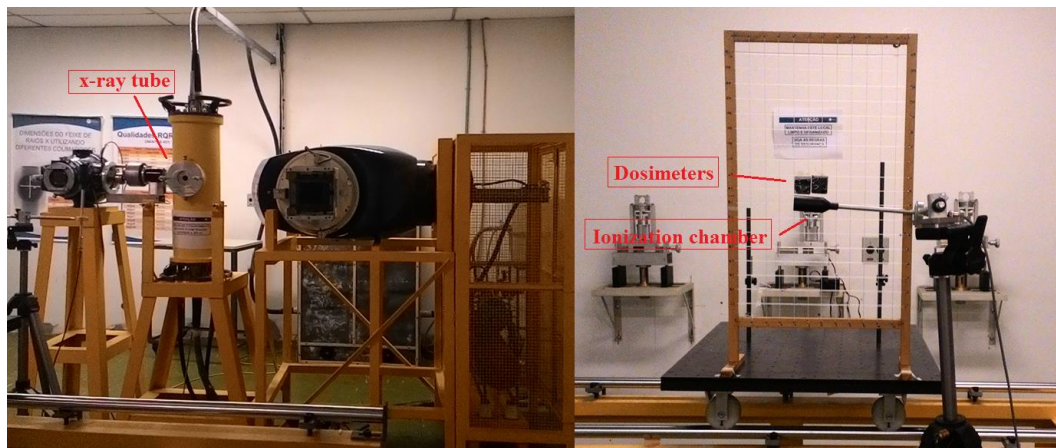


Figure 3.9 - Left: Constant potential x-ray tube MCN 421 (Philips, Germany). Right: Dosimeters and ionization chamber were positioned 5 meters away from the x-ray tube.

The 0.6 cc ionization chamber model 10X5-0.6, coupled to an electrometer model 9010, was used in another set of measurements. In this set of measurements, chamber and dosimeters were positioned one meter away from the focal spot of the x-ray tube. Uniformity of the x-ray field under these conditions was tested and CV was 0.4%.

The third set of measurements was performed using a clinical 64-slice CT scanner (model Philips Brilliance 64, Philips, Germany) at the Institute of Radiology of the School of Medicine of the University of São Paulo (InRad/FMUSP) and the 0.6 cc ionization chamber model 10X5-0.6, coupled to the electrometer model 9010 (Radcal Corporation, Monrovia, CA, USA). The ionization chamber was positioned in the center of the gantry on an acrylic holder attached to a support (Figure 3.10). Alignment was performed by the laser system of the equipment.

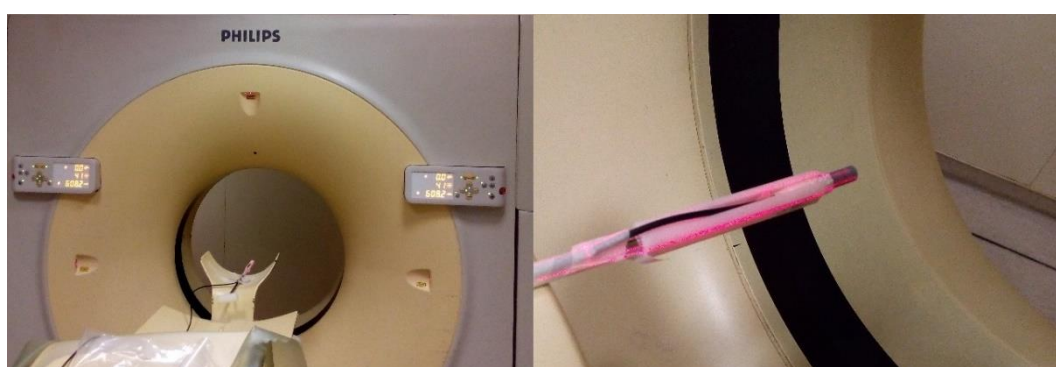


Figure 3.10 - Left: The ionization chamber at the isocenter of the gantry of the 64-slice Philips Brilliance 64 CT Scanner (Philips, Germany). Right: The 0.6 cc ionization chamber, model 10X5-0.6, placed on the acrylic holder. Air kerma was measured at this position and then each group of TLD and OSLD was positioned at the same place.

Since the measurement conditions were not the same as in the standard laboratories, some correction factors needed to be applied in order to convert the ionization chamber readings into air kerma ( $K_{air}$ ). During the measurements, for instance, some independent influence quantities, such as temperature and pressure, cannot be controlled, but can be corrected by applying the product of the appropriate correction factors ( $k_i$ ). (IAEA, 2007). Therefore, calibration factors were applied to each chamber reading according to their calibration certificate. For the 30 cc ionization chamber, uncertainties on air kerma values were expanded considering uncertainties in temperature, pressure and calibration coefficient. These values were adopted by the guidance on uncertainty levels as proposed by the International Atomic Energy Agency Code of Practice in Radiology (IAEA, 2007), which presents uncertainty estimates for different scenarios. For the present study, scenario 1 was considered (IAEA, 2007; Martins, 2015). For the 0.6 cc ionization chamber, correction factors for temperature ( $T$ ) and pressure ( $P$ ) were automatically applied during the irradiation. Calibration coefficient and its uncertainty are presented in the certificate of calibration of the chamber. Uncertainties on air kerma values were adopted considering the standard deviation of the mean of two measurements and the uncertainty of the calibration coefficient. Confidence level considered in both cases was 68.3% ( $k = 1$ ).

### 1. Batch Homogeneity

A group of 452 OSLDs was irradiated using the MCN 421 x-ray tube to evaluate the batch homogeneity of the OSLD response to the same beam quality. The RQT 9 x-ray beam quality was used, as it usually corresponds to the reference radiation quality for calibration of instruments used in computed tomography dosimetry (IAEA, 2007). The irradiation technique comprised 120 kV, 15 mA, and exposure time of 675 s. The air kerma measured with the 30 cc ionization chamber was  $20.4 \pm 0.3$  mGy.

### 2. Energy Response

OSL energy response was evaluated for eight standard x-ray beam qualities: RQR 2, RQR 4, RQR 5, RQR 6, RQR 8, RQT 8, RQT 9, and RQT 10. RQR series of radiation qualities represent the beam incident on the patient in general radiography, whereas RQT series simulate the unattenuated beam used in CT procedures (IAEA, 2007). Differences between each series are due to the x-ray tube voltage, total filtration, and, therefore, the effective energy of the x-ray beam. Once the RQR series were established, the RQT series were obtained by adding

external copper filtration (IAEA, 2007). Eight groups of three OSLDs were irradiated using the MCN 421 x-ray tube and the corresponding air kerma values were measured with the 30 cc ionization chamber. The OSL signal of each quality was evaluated by calculating the average of three dosimeter responses and the uncertainties were obtained as the standard deviation of the mean of the responses ( $k = 1$ ).

The effective energy,  $E_{eff}$ , of each x-ray beam quality was calculated using the relations described below, which associate the measured HVLs to the aluminum linear attenuation coefficient  $\mu_{Al}(E_{eff})$ .

$$HVL = \frac{\ln(2)}{\mu_{Al}(E_{eff})} \quad (3.1)$$

Rewriting this equation, by dividing both sides per aluminum density ( $\rho_{Al}$ ), HVL and effective energy of the beam are related to the mass attenuation coefficient  $\left(\frac{\mu}{\rho}\right)$  of this element, as follows:

$$\left(\frac{\mu}{\rho}\right)_{Al} = \frac{\ln(2)}{HVL \times \rho_{Al}} \quad (3.2)$$

The HVL for each x-ray beam quality was determined with data provided by the IAEA Technical Series Report 457 (IAEA, 2007) and the aluminum density was determined with data provided by the National Institute of Standards and Technology (NIST) (1998). Therefore, with  $\rho_{Al} = 2.699 \text{ g/cm}^3$  and values of HVL, mass attenuation coefficient for each x-ray beam quality were determined.

For RQT 9 x-ray beam quality, for instance,  $HVL = 0.84 \text{ cmAl}$ . This leads to

$$\left(\frac{\mu}{\rho}\right)_{Al} = \frac{\ln 2}{0.84 \times 2.699} = 0.3057 \frac{\text{cm}^2}{\text{g}}, \quad (3.3)$$

which can be related to the effective energy of the beam considering the information provided by NIST (2011). The effective energy ( $E_{eff}$ ) can be found by identifying in NIST's database which beam energy corresponds to the mass attenuation coefficient of the aluminum determined in Equation 3.3. Therefore, the effective energy for the RQT 9 beam is considered to be approximately 56.1 keV.

Similarly, effective energy was determined for all the x-ray beam qualities. Results were normalized to the RQT 9 x-ray beam quality and then compared to the results provided by other

authors (Gasparian, Vanhavere, & Yukihiro, 2012; Malthez, Freitas, Yoshimura, & Button, 2014). Table 3.1 summarizes tube voltage (kV), external filtering, HVL and  $E_{eff}$  for each x-ray beam quality.

Table 3.1 – X-ray beam qualities RQR and RQT series used to evaluate the energy response of the dosimeters. X-ray tube voltage (kV), external copper filtration (mm Cu), nominal first HVL (mm Al) and determined effective energy are presented for each radiation quality.

Radiation Quality <sup>i</sup>	x-ray tube voltage <sup>ii</sup> [kV]	External filtration <sup>ii</sup> [mm Cu]	Nominal first HVL <sup>ii</sup> [mm Al]	Effective energy [keV]
RQR 2	40	-	1.42	25.3
RQR 4	60	-	2.19	29.7
RQR 5	70	-	2.58	31.3
RQR 6	80	-	3.01	33.2
RQR 8	100	-	3.97	37.9
RQT 8	100	0.20	6.90	49.7
<b>RQT 9<sup>iii</sup></b>	<b>120</b>	<b>0.25</b>	<b>8.40</b>	<b>56.1</b>
RQT 10	150	0.30	10.10	64.2

i. RQR series represent the beam incident on the patient in general radiography and RQT series simulate the unattenuated beam in CT procedures.

ii. Data retrieved from the IAEA Technical Series Report 457 (IAEA, 2007).

iii. Reference radiation quality usually applied in calibration of equipment for CT dosimetry. Therefore, data were normalized for this quality.

### 3. Linearity of Response

Linearity of the OSL responses to the incident air kerma was evaluated using the x-ray beam quality RQT 9 in the MCN 421 x-ray tube in distinct situations. In a first set of measurements, three groups of three unused dosimeters and the 30 cc ionization chamber were simultaneously irradiated. A fourth group was used to estimate the background irradiation. Tube voltage was fixed as 120 kV, and five different tube current-time product (mAs) values were used, so that IC reading ranged from 1 mGy to 44 mGy.

Another set of OSL linearity responses was assessed at InRad/FMUSP using a Philips 64-slice CT scanner and the 0.6 cc ionization chamber. Ionization chamber and the dosimeters were positioned in the center of the gantry on an acrylic holder attached to a support (Figure 3.10). Five groups of three unused OSLDs were irradiated along with five groups of three TLDs. These experiments used a tube voltage of 120 kV and five different values of tube current-time product ranging from 30 mAs to 400 mAs. The resulting ionization chamber readings for these

settings ranged from 3.9 mGy to 51.8 mGy. After these experiments, OSLDs were irradiated with the beta source of the Risø reader for two seconds, as previously described (Section 3.1.2), and their responses to beta radiation were used to individually normalize their responses to the x-ray. The techniques applied in each situation are summarized in Table 3.2.

Table 3.2 - Parameters used to assess OSLD linearity of responses in distinct situations. At the laboratory, the dosimeters and the ionization chamber were placed one meter away from the x-ray tube focal spot. At the hospital, the dosimeters and the ionization chamber were placed in the center of the gantry of the Philips Brilliance 64 CT scanner.

Source/ Chamber	Tube voltage (kV)	Tube current-time product (mAs)	Air Kerma (mGy)	TLD group	OSLD group
CT Scanner/ 0.6 cc	120	30	3.92±0.09	1	1
		100	13.05±0.28	2	2
		150	19.55±0.41	3	3
		200	26.01±0.56	4	4
		400	51.83±1.10	5	5
x-ray tube/ 0.6 cc	120	90	4.02±0.05	1	1
		270	12.90±0.08	2	2
		540	26.25±0.20	3	3
		1080	52.98±0.50	4	4
		2700	133.00±2.02	5	5

In another set of measurements, five groups of three OSLDs and five groups of three TLDs along with the 0.6 cc ionization chamber were positioned one meter away from the focal spot of the MCN 421 x-ray tube. These experiments used a tube voltage of 120 kV, tube current of 9 mA, and five different values of exposure time ranging from 10s to 300s. The resulting ionization chamber readings for these settings ranged from 4 mGy to 133 mGy (Table 3.2). These measurements aimed to verify the applicability of the CT standard qualities with the MCN 421 x-ray tube for irradiating OSLD or TLD to generate calibration curves. Calibration curves were constructed to be applied to evaluate organ doses due to clinical computed tomography procedures.

#### 4. Reproducibility and Reusability

Reproducibility and reusability of OSLDs responses were evaluated using the 0.6 cc ionization chamber positioned 1 meter away from the focal spot of the MCN 421 x-ray tube

and x-ray beam quality RQT 9. Dosimeters were fractionated into disks measuring 5 mm in diameter. These experiments used a tube voltage of 120 kV, tube current of 9 mA and exposure time of 50s, so that ionization chamber reading was  $20.3 \pm 0.3$  mGy. Four exposures were performed in a one-week period using the same parameters, with 72 dosimeters separated in three distinct groups of 24 dosimeters each. Each one of the three groups were analyzed with different approaches in order to choose the most precise method.

Groups were separated as follows: dosimeters from *Group 1* were bleached, read, irradiated and read again. Dosimeters from *Group 2* were bleached, irradiated and read. Dosimeters from *Group 3* were bleached, irradiated, read, irradiated with the  $^{90}\text{Sr}/^{90}\text{Y}$  beta source for two seconds and read again. This same cycle was performed for each group four times. Table 3.3 summarizes the groups and the corresponding cycles.

Table 3.3 - OSL groups considered for the reproducibility and reusability tests

<b>Group</b>	<b>Cycle</b>
<i>Group 1</i>	Bleaching, reading, irradiation, reading
<i>Group 2</i>	Bleaching, irradiation, reading
<i>Group 3</i>	Bleaching, irradiation, reading, irradiation with beta source, reading

Reproducibility test aimed to evaluate the precision of dosimeter responses under the same irradiation conditions. Reusability test aimed to verify the efficacy of the bleaching and the possibility of reusing the dosimeters in subsequent irradiations. The application of three different approaches aimed to evaluate the most accurate and precise one, by assessing the effect of normalization of OSL signal per their responses to beta radiation.

### 3.2.2. Selection of CT Scanning Protocols

The protocol selection was performed with the analysis of a patient database from InRad (APPENDIX B). The information extracted from PACS/RIS presented the most applied protocols for pediatric patients performing head and thorax CT. A total of 450 pediatric patients, from 0 to 15 years old, who performed thorax or head CT examinations were analyzed from March to April, 2016, by using a retrospective database from 2014 and 2015. For 0 to 1 year old patients, database from 2012 to 2016 were assessed. This study was essential to investigate the variety of all CT studies performed in the partner institution in order to choose the protocols to be applied in the experimental measurements with both adult and anthropomorphic

phantoms, aiming to better approximate these measurements with standard clinical examinations. Using such information and irradiating both phantom with similar protocols, it was possible to compare the absorbed doses to the target organs received by adult and pediatric patients when performing standard routine examinations. In the present study, eye lenses, thyroid, lungs and liver were the target organs. Such organs were chosen because of their high radiosensitivity (ICRP, 2000) and the protocols selected.

### 3.2.3. Organ Volumes Determination for Adult and Pediatric Phantoms

Both phantoms used in this study are sectioned in 25 mm slices and they were designed for dosimetry purposes. Each slice has drilled holes for holding different types of dosimeters. In order to estimate the organ doses due to computed tomography procedures, the methods applied are similar to the developed by Huda & Sandison (1984) and by Golikov & Nikitin (1989). Huda & Sandison state that the organ risk due to ionizing radiation,  $R_T$ , is defined as

$$R_T = R \sum f_i(\text{organ}) \times D_i \quad (3.4)$$

where  $R$  is the organ risk per unit dose,  $f_i$  is the fraction of the total mass of the organ inside a slice  $i$  and  $D_i$  is the mean absorbed dose by the fraction of this organ inside the slice  $i$ . In Equation 3.4 the sum is performed over all the slices.

Similarly, Golikov & Nikitin state that in order to evaluate the mean organ dose to a target organ, it is necessary to combine the anatomical data of the phantom with the measured dose distribution within the organ (Golikov & Nikitin, 1989). The mean dose to an organ can be calculated by

$$D = \sum_i f_i \times D_i \quad (3.5)$$

where  $D$  is the dose to the organ,  $f_i$  is the fraction of the total mass of the organ inside a slice  $i$  and  $D_i$  is the mean absorbed dose to the fraction of this organ inside the slice  $i$ .

Therefore, the determination of the fraction of the total mass of the organs of interest inside each slice of the phantom is the first step to evaluate the organ doses in these objects.

### 3.2.3.1. The RANDO Phantom

The organ mass fractions of the RANDO Phantom,  $f_i$ , used in this work, were determined and published by Huda & Sandison (1984) and Golikov & Nikitin (1989).

According to Huda & Sandison, small sized organs, such as the thyroid, result in a uniform dose distribution and, therefore,  $f_i$  in Equation 3.4 and 3.5 reduces to unity. This simplifies the estimate of the mean thyroid dose, which can be performed simply by placing dosimeters in the location of the organ (Huda & Sandison, 1984).

The lungs, however, are located within slices 10 to 20 and the  $f_i$  values, where  $i$  ranges from 10 to 20, were determined by the authors with radiograph images from each slice. The authors measured the fractional masses inside the slices and the results are presented in Section 4.3.1 (Huda & Sandison, 1984).

Similarly, Golikov & Nikitin performed the analysis to other organs of the RANDO phantom, such as the liver. In that work, the authors used an anatomical atlas so that they could define the organ contours in the radiographic images of the phantom and, then, determine the volumes of the organs inside each slice. Since each organ considered is a soft-tissue organ, the organ volumes are similar to their masses and the values of  $f_i$  were approximated to the organ volumes inside each slice (Golikov & Nikitin, 1989). In addition, these authors defined a system to localize the organs and place the dosimeters inside them, since the location and shape of these organs are not explicitly shown in the phantom sections. For the liver, which is the organ of interest in the present study, the values of  $f_i$  determined are presented in Section 4.3.1. The system for localizing a fraction of this organ inside one slice is also demonstrated in Section 4.3.1 and was adopted to localize the liver in all slices in the present study.

### 3.2.3.2. The CIRS ATOM Model 705 Phantom

To estimate the organ mass fractions of the CIRS ATOM 705 pediatric phantom, two approaches were adopted. Due to the soft-tissue nature of the organs as stated by Golikov & Nikitin (1989), volume fractions were determined as the values of  $f_i$ . The lung volume fractions were estimated based on the CT images of the phantom and a segmentation technique. The liver location and volume fractions per slice were estimated using a commercial software. The thyroid location was obtained from the study developed by Inkoom and collaborators (2015).

#### 1. Determination of organ volumes by a segmentation technique

DICOM images from the entire thoracic region of the pediatric phantom were analyzed. The lung tissue is inside the physical slices 9-15 of the phantom (CIRS, 2013) and there were about 20 CT images per physical slice of the phantom. Analyses were performed with the software Matlab®2015 and Origin®2016 (Giansante, Sawamura, Tomal, & Costa, 2016).

In order to assess the dimensions of the thoracic region of the phantom, a thresholding algorithm was applied to the CT images. This algorithm creates binary partitions in the images that are based on the attenuation values of the structures on CT images, determining threshold values that group together all elements inside a proper attenuation value interval (Mansoor et al., 2015). In the present work, this algorithm was developed using the software Matlab®2015 and was used in order to separate the lung tissue from the other tissues in the image. Figure 3.11 demonstrates the effect of this method in an image.

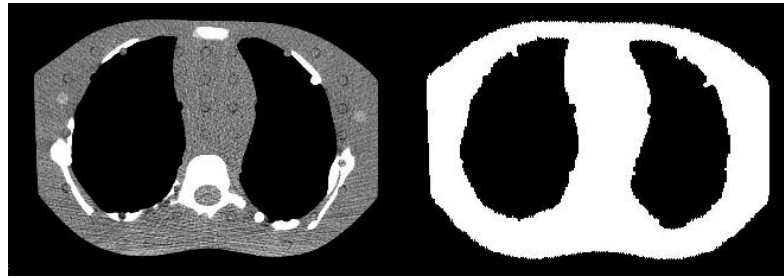


Figure 3.11 – Example of the application of the thresholding algorithm to a CT image of the CIRS ATOM pediatric phantom. The lung tissue is represented in black and all the other structures are grouped in the white pixels.

The threshold level used to group the pixels of the lung tissue into the same group was determined visually for each CT image. With this procedure, it was possible to estimate the area (in pixels) of the lungs and, then, the volume of the lungs inside each CT image,  $V_i$ , according to

$$V_i = A_i \times p^2 \times t \quad (3.6)$$

where  $A_i$  is the area (in pixels) of the lungs inside each CT image,  $p$  is the length of the pixel in millimeters and  $t$  is the thickness of the CT image. These quantities are available in the DICOM header of each image. In this work,  $p = 0.6465 \text{ mm}$  and  $t = 1.3 \text{ mm}$ . Uncertainties on this method were estimated considering the uncertainties on the visual determination of the threshold level

and on the values of  $p$  (1.1%) and  $t$  (4%)<sup>h</sup> (APPENDIX A). Therefore, it was possible to calculate the fraction of the total lung volume,  $f_i$ , inside each physical slice.

## 2. Computer program

The liver mass fractions of this phantom were estimated considering the images of patients undergoing CT examinations that had a similar anatomy to the phantom. In addition, in order to place the dosimeters inside of this organ, it was necessary to localize this organ inside the physical slices of the phantom. Inkoom et al. (2015) evaluated the location of radiosensitive organs inside four models of the CIRS ATOM dosimetry phantoms along with practical data for dosimeters placement. This study and the analysis performed by a radiologist from the partner institution<sup>i</sup> were combined and it was possible to define the location and to estimate the mass fractions of the liver inside the phantom slices.

CT images from five patients who performed abdomen CT were analyzed with the software iSite Radiology (Philips, Germany). The images corresponding to the abdominal scans of the patients were sectioned in 25 mm intervals to have the same length of the phantom, in a similar approach as performed by Inkoom et al. (2015), to cover the entire abdominal region. As a consequence, the liver was within a 125 mm region for each patient, which corresponds to 5 slices of the physical phantom.

The volume of the liver inside each section, the total volume and the fraction  $f_i$  per slice were determined for each patient. The average of  $f_i$  obtained for the five patients was adopted as an approximate estimative of the liver volume fractions for the phantom and these quantities were used to estimate the absorbed dose by the liver. Uncertainties were considered as the standard deviation of the mean of the fractions from all patients ( $k = 1$ ).

### 3.2.4. Phantom Irradiations

The CIRS ATOM phantom was irradiated with three different protocols and the RANDO phantom was irradiated with two protocols. All the irradiations were performed with the 64-slice CT scanner Philips Brilliance 64 (Philips, Germany) of the InRad/FMUSP. OSL/TL dosimeter groups were placed in each organ according to each protocol applied. Groups of three TLDs and three OSLDs were used to estimate the background radiation in

---

<sup>h</sup> Courtesy: Daniel Vicente Vieira (IFUSP).

<sup>i</sup> Dr. Marcio Sawamura is a radiologist from the Institute of Radiology of the School of Medicine of the University of São Paulo (InRad/FMUSP) and collaborated with the present work.

every measurement. Figure 3.12 presents the displacement of the dosimeters on the eye lenses, in the thyroid and in the lung portion of the slice 13 for the pediatric phantom as an example.

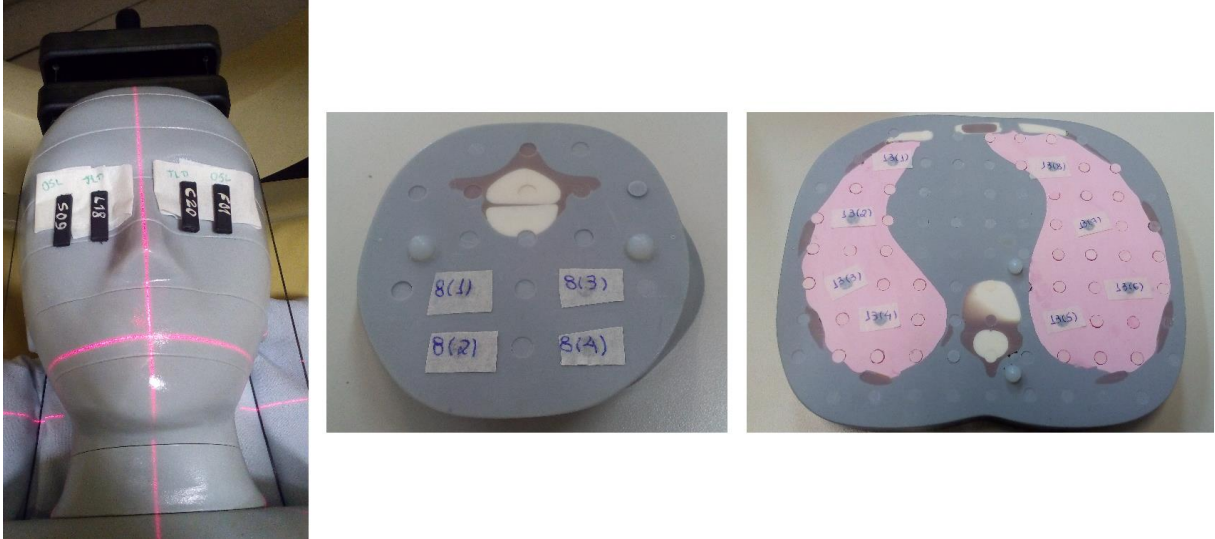


Figure 3.12 - Left: OSL and TL dosimeters placed on the eye lenses of the pediatric anthropomorphic phantom. This picture also demonstrates the laser system used to perform the alignment of the phantom in the isocenter of the gantry. Center: The 8<sup>th</sup> slice of the anthropomorphic phantom with the dosimeters placed in the location of the thyroid. Right: The 13<sup>th</sup> slice of the phantom with the 8 groups of dosimeters placed inside the lungs of the phantom.

Similarly, Figure 3.13 presents the displacement of dosimeter groups in the slices 9 (thyroid), 11 (lungs) and 20 (liver) of the adult phantom as an example.



Figure 3.13 - Left: OSL and TL dosimeters placed in the thyroid of the adult anthropomorphic phantom, located inside the 9<sup>th</sup> slice. Center: The 11<sup>th</sup> slice of the anthropomorphic phantom with the dosimeters placed inside the lungs. Right: The 20<sup>th</sup> slice of the phantom with the dosimeters placed inside the liver.

#### 3.2.4.1. The CIRS ATOM Model 705 Phantom

The first irradiation of this work was performed using the 5-year old CIRS ATOM phantom. The protocol applied in this study was selected among the ones performed by pediatric patients during 2014-2016, in the age range 2-5 years old, at the Philips Brilliance 64 CT scanner dedicated to routine examinations. It is the “Thorax for Children” (in Portuguese: *Tórax Infantil*) CT protocol, which is a standard chest protocol applied in children in this age

range. Sets of 36 groups of 5 TLDs and 4 OSLDs were placed inside the slices of the phantom as described in Table 3.4. Table 3.4 also presents the volume fractions ( $f_i$ ) of the organs of interest inside each slice, as previously discussed and presented in Section 4.3.2. For the thyroid,  $f_8$  reduces to unity.

The phantom was positioned in the isocenter of the CT scanner and the alignment was performed with the laser system of the equipment, as it can be seen in Figure 3.12. The phantom was irradiated approximately from the middle of its neck (slice 8) until the middle of its abdomen, so that scan range was 22 cm.

The second set of measurements performed was a thorax, abdomen and pelvis study. The protocol used was the “Thorax, abdomen and pelvis (3 phases)” (in Portuguese: *Tórax, abdomen e pelve trifásico*), which was the most applied chest, abdomen and pelvis protocol for children in this age range, although it is a standard adult protocol defined in the CT scanner. Although three phases were performed in this protocol, it is important to note that this examination does not correspond to a clinical situation performed in the routine of the hospital. In such situation, the majority of the thorax, abdomen and pelvis protocol was applied in a one phase only, and the AEC was always applied. In the experimental measurement with the phantom, sets of 56 dosimeter holders with 2 TLDs and 2 OSLDs each were distributed inside the lungs, liver and thyroid of the phantom. The distribution of these groups inside each slice along with the organ mass fraction ( $f_i$ ) is presented in Table 3.4. The liver contribution of slice 19 was added to slice 18 and dosimeters were placed from slice 15 to slice 18.

The phantom was irradiated from the neck to the pelvis, starting in slice 8, with a scan range of 46.5 cm, covering the entire thoracic and abdominal regions. Acquisition parameters were the same in the three phases of the examination.

The third set of measurements was a Head and Neck examination. The protocol used was the “Head 3D”, which was usually applied in children in this age range, despite being a standard adult protocol. One holder with 3 TLDs and one holder with 3 OSLDs were placed per eye lenses of the phantom and four dosimeter holders with 2 TLDs and 2 OSLDs were placed in the thyroid. The distribution of dosimeter holders inside the organs of the phantom is presented in Table 3.4.

The phantom was irradiated from the top of its head until its neck (slices 0 to 8), with a scan range of 23.1 cm, covering the eye lenses and the thyroid of the phantom. It is important to note, however, that this was adopted only to verify the effect of the radiation dose when the thyroid is directly irradiated by the primary beam of the CT scanner. This result was, then,

compared to the one obtained when the dose to this organ was only due to the scattered radiation in a similar irradiation with the adult phantom. During a typical Head examination, the neck of the patient is not irradiated.

Table 3.4 - Displacement of dosimeter groups inside the slices of the CIRS ATOM pediatric anthropomorphic phantom along with the organ mass fraction inside each slice for all protocols.

Slice ( <i>i</i> )	Organ	$f_i$	Thorax for children	Thorax, Abdomen and Pelvis (3 phases)	Head 3D
			Number of TL/OSL groups	Number of TL/OSL groups	Number of TL/OSL groups
	Eye lenses (right)	0.50			2
	Eye lenses (left)	0.50			2
8	Thyroid	1.00	4	4	4
9		0.02	2	2	
10		0.14	4	4	
11	Lungs	0.19	6	6	
12		0.22	6	6	
13		0.23	8	8	
14		0.17	4	6	
15		0.03	2	2	
15		0.14		2	
16	Liver	0.35		7	
17		0.30		5	
18 (18+19)		0.22		4	

Parameters used for all protocols are listed in Table 3.5, along with the  $CTDI_{vol}$  and DLP values displayed by the scanner. In this table,  $N$  is the number of detector rows,  $T$  is the detector width, tube current-time product,  $mAs$ , is defined as the product of the tube current ( $mA$ ) and the tube rotation time ( $s$ ) and  $mAs_{eff}$  is the effective tube current-time product ( $mAs$ ) divided by the pitch ( $p$ ).

Table 3.5 – CT acquisition parameters used in the three protocols applied to the CIRS ATOM pediatric anthropomorphic phantom.

	<b>Thorax for children</b>	<b>Thorax, Abdomen and Pelvis (3 phases)</b>	<b>Head 3D</b>
<b>Tube Voltage (kV)</b>	120	120	120
<b>Tube current (mA)</b>	121	61	119
<b>Rotation time (s)</b>	0.45	0.75	0.75
<b>Tube current-time product (mAs)</b>	55	39	299
<b>Effective tube current-time product (mAs<sub>eff</sub>)</b>	59.7	33.3	1003
<b>Pitch</b>	0.922	1.172	0.298
<b>N × T(mm)</b>	64 × 0.625	64 × 0.625	64 × 0.625
<b>Collimation (mm)</b>	40	40	40
<b>Scan Range (mm)</b>	220	465	231
<b>CTDI<sub>vol</sub> (mGy)</b>	7	2.6	38.7
<b>DLP (mGy.cm)</b>	196.3	138.0	1103

#### 3.2.4.2. The RANDO Phantom irradiation

The first protocol applied to this phantom was the same protocol applied in the measurement with the CIRS ATOM phantom, “Thorax, abdomen and pelvis (3 phases)”, which is a standard adult protocol, in order to compare the results obtained with the application of the same protocol in pediatric patients. All three phases were performed with the same parameters, which were extracted from the patient data collected at the PACS/RIS system of the hospital corresponding to adult patients who performed this examination in 2015. As previously described, in a clinical routine examination the 3 contrast phases are only applied in the abdomen region, and not in the thoracic and pelvic regions of the patient. In addition, although the examinations were performed with tube current modulation (TCM), tube current (mA) was fixed in this measurement to allow comparisons with the results obtained with Monte Carlo simulations. Therefore, in order to estimate and select a proper fixed tube current, this value was calculated by averaging all tube current of the three phases of one clinical examination. The distribution of the 66 dosimeter holders with 2 TLDs and 2 OSLDs each inside each slice of the phantom, along with the organ mass fractions ( $f_i$ ) per slice, are presented in Table 3.6. In this phantom,  $f_9$  reduces to unit because the thyroid is located inside the 9<sup>th</sup> slice. The lung contribution of the 10<sup>th</sup> slice was added to slice 11.

The phantom was irradiated three times with the same acquisition parameters, from slice 11 to slice 35, corresponding to 68.0 cm of scan range that covers the entire thoracic and abdominal region.

The second protocol applied in this measurement was a head protocol (“Head/3D”). One holder with 3 TLDs and one holder with 3 OSLDs were placed per eye lens of the phantom and two holders with 2 TLDs and 2 OSLDs were placed in the thyroid. Table 3.6 presents the distribution of the dosimeter holders inside the organs of the phantom. This phantom was irradiated from the beginning until the end of its head, from slice 0 to slice 6, corresponding to 18.0 cm of scan range that covers the eye lenses. Parameters used in all set of measurements for this phantom are presented in Table 3.7.

Table 3.6 - Displacement of dosimeter groups inside the slices of the of the RANDO phantom along with the organ mass fraction inside each slice, as determined by Huda & Sandison (1984) and Golikov & Nikitin (1989), for all protocols.

Slice ( <i>i</i> )	Organ	$f_i$	Thorax, abdomen and pelvis	Head
			Number of TL/OSL groups	Number of TL/OSL groups
	Eye	0.50		2
	Eye	0.50		2
9	Thyroid	1.00	2	2
11 (10+11)		0.06	2	
12		0.09	4	
13		0.11	4	
14		0.14	6	
15		0.14	6	
16	Lungs	0.13	4	
17		0.13	4	
18		0.11	4	
19		0.07	4	
20		0.02	2	
19		0.15	2	
20		0.29	6	
21	Liver	0.27	6	
22		0.17	5	
23		0.09	3	
24		0.03	2	

Table 3.7 - CT acquisition parameters used in the protocols applied to the RANDO anthropomorphic phantom.

	<b>Thorax, Abdomen and Pelvis (3 phases)</b>	<b>Head 3D</b>
<b>Tube Voltage (kV)</b>	120	120
<b>Tube current (mA)</b>	156	119
<b>Rotation time (s)</b>	0.75	0.75
<b>Tube current-time product (mAs)</b>	100	299
<b>Effective tube current-time product (mAs<sub>eff</sub>)</b>	85.3	1003
<b>Pitch</b>	1.172	0.298
<b>N × T(mm)</b>	64 × 0.625	64 × 0.625
<b>Collimation (mm)</b>	40	40
<b>Scan Range (mm)</b>	680	180
<b>CTDI<sub>vol</sub> (mGy)</b>	6.5	38.7
<b>DLP (mGy.cm)</b>	494.5	860

### 3.2.5. Organ Doses Evaluation

TL and OSL dosimeters were placed in the dosimeter holders and distributed inside the target organs of the anthropomorphic phantoms. After performing the irradiations with the 64-slice Philips Brilliance 64 CT scanner, dosimeters were read with the Risø TL/OSL reader model DA-20 (DTU Nutech. Inc., Roskilde, Denmark) (Sections 3.1.2 and 3.1.3). In every set of measurements, a group of dosimeters was maintained outside the CT scanner room to quantify the background radiation, which was subtracted from the irradiated dosimeter signals.

In order to convert the TL and the OSL signals to each organ absorbed dose, the following procedure was applied. First, in every set of measurements a calibration curve was constructed for each type of dosimeter using the 64-slice CT scanner Philips Brilliance 64, five groups of three TLDs, five groups of three OSLDs and a 0.6 cc ionization chamber model 10X5-0.6 (Radcal Corporation, USA). This procedure was performed in order to convert the reading of the dosimeters into air kerma. Tube voltage was fixed at 120 kV, which was the standard tube voltage of the protocols applied to the phantoms.

After converting the reading of the dosimeters into air kerma ( $K_{air}$ ), the mean value of  $K_{air}$  was calculated for each slice  $i$  of the phantom according to Equation 3.7. In this equation,  $G$  is the total number of dosimeter groups inside the slice  $i$  and  $\sigma_n^2$  is the variance of the dosimeter values from all the dosimeters placed in a group  $n$  (Martins, 2015; Martins, Nersissian, & Costa, 2015; Vuolo, 2002).

$$K_{AIR}^i = \frac{\sum_{n=1}^G (K_{AIR}^n / \sigma_n^2)}{\sum_{n=1}^G (1 / \sigma_n^2)} \quad (3.7)$$

Then,  $K_{AIR}^i$  needs to be converted to organ average absorbed dose in the organ slice  $i$ ,  $D_i$ , according to Equation 3.8 (Gonzaga, Mourão, Magalhães, & da Silva, 2014; Martins, 2015; Okuno & Yoshimura, 2010).

$$D_i = K_{AIR}^i \frac{(\mu_{en}/\rho)_{Organ}}{(\mu_{en}/\rho)_{Air}} \quad (3.8)$$

In the Equation 3.8,  $(\mu_{en}/\rho)_{Organ}$  and  $(\mu_{en}/\rho)_{Air}$  are the mass-energy absorption coefficients for the target organ and air, respectively, which depends on the effective energy of the radiation beam quality. For the RQT 9 x-ray beam quality, the effective energy was determined with Equations 3.1-3.3 ( $E_{eff}(RQT9) = 56.1 \text{ keV}$ ).

In order to calculate the mass-energy absorption coefficient for the organs and the air, it was used the composition of each tissue and the air along with the information provided by the NIST database (Hubbell & Seltzer, 2004). This database provides the values of mass attenuation coefficient,  $(\frac{\mu}{\rho})$ , and the mass-energy absorption coefficient,  $(\frac{\mu_{en}}{\rho})$ , as a function of photon energy for 92 elements. Each compound or mixture coefficients can be found as weighted sums over the corresponding coefficients for the elements (ICRU, 1989). Then, in order to determine the coefficients corresponding to the RQT 9 x-ray beam quality effective energy, a cubic spline interpolation was applied with a Matlab®2015 routine, which considers data available at NIST database and the weighted elements provided by the user. The composition of tissues and air was extracted from the ICRU Report 44 (1989). Results obtained for the mass-energy absorption coefficient for each compound are presented in Table 3.8.

Table 3.8 – Mass-energy absorption coefficient obtained for each compound and applied in order to estimate the organ doses (effective energy of 56.1 keV).

	<b>Eye lenses</b>	<b>Liver</b>	<b>Lung tissue</b>	<b>Thyroid</b>	<b>Air (sea level)</b>
$(\frac{\mu_{en}}{\rho})$	0.0336	0.0364	0.0365	0.0402	0.0339

Finally, the mean absorbed doses to the liver and the lungs can be obtained by summing up the contributions of these organ doses in all  $i$  slices,  $D_i$ , according to Equation 3.9 (Golikov

& Nikitin, 1989). For small organs such as the thyroid,  $f_i$  reduces to unity since the entire organ is inside one slice of the phantom. For the eye lenses, dose is calculated simply by averaging the doses to both right and left eyes. Uncertainties in these values were determined considering the standard deviation of the mean of the dosimeters inside each group ( $G$ ), uncertainties in the air kerma calculated with the calibration curve and in the estimative of the values of  $f_i$  (for the CIRS ATOM phantom). Confidence level considered is 68.3% ( $k = 1$ ).

$$D = \sum_i f_i \times D_i \quad (3.9)$$

### 3.2.6. Comparison of patient data with international DRL

A pediatric patient database from InRad was analyzed in the present work (APPENDIX B). Besides useful for selecting the protocols to be applied in the experimental measurements (Section 3.2.2), the assessment of a statistically significant number of patients from the institution was helpful to identify the most common practices performed in the routine and, as a consequence, identify possible non-adequate ones. All patient information was extracted from this database, including patient and protocol data, such as: age, weight, acquisition parameters,  $CTDI_{vol}$  and DLP. The latter two values were used in comparison with international Diagnostic Reference Levels (DRL) as a tool to evaluate doses indexes related to general clinical practices.

$CTDI_{vol}$  values were analyzed in terms of each sequence/phase and DLP values were analyzed for the whole exam. For each age group, mean and median values were determined and compared with international DRLs derived from three surveys: the United Kingdom survey (Shrimpton, Hillier, Lewis, & Dunn, 2005; Shrimpton, Hillier, Meeson, & Golding, 2014), an European survey (European Society of Radiology, 2015) and an International survey (Vassileva et al., 2015). The latter survey was evaluated with data from 32 countries.

## 4. RESULTS

### 4.1. OSLD CHARACTERIZATION

#### 1. Batch Homogeneity

OSL responses to the x-ray irradiation presented an approximate Gaussian behavior (Figure 4.1). A group of 330 dosimeters from the 452 irradiated disks, corresponding to 73% of the initial batch, presented OSL signals within the interval of 4.7% from the average. Statistical tests were performed to verify the Gaussian behavior of the responses (APPENDIX C).

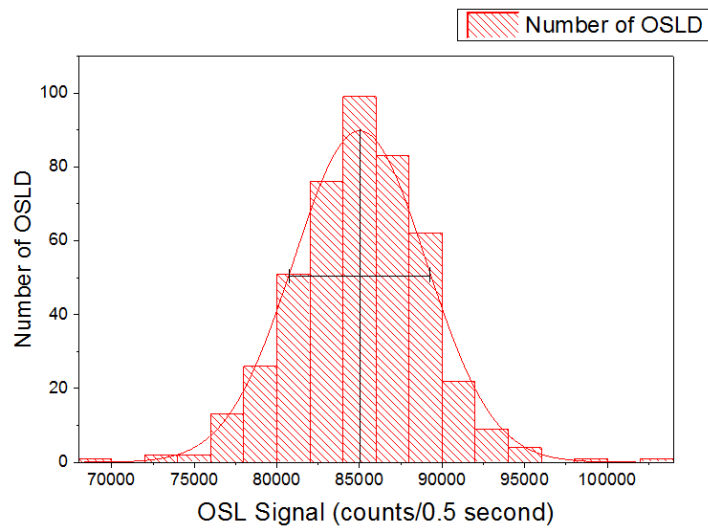


Figure 4.1 - Distribution of the OSLD responses. 452 unused dosimeters were irradiated at the same time with the same technique. Standard deviation corresponded to 5% of the average.

#### 2. Energy Response

Dosimeters presented an energy-dependent response (Figure 4.2). Results obtained in this study were compared to the ones obtained by Gasparian et al. (2012) and by Malthez et al. (2014). These authors performed a similar analysis with the same kind of OSLD. In order to compare the results of this study to the results obtained by the aforementioned authors, data of their work, provided by them, were normalized to the results of this study and are presented in Figure 4.2.

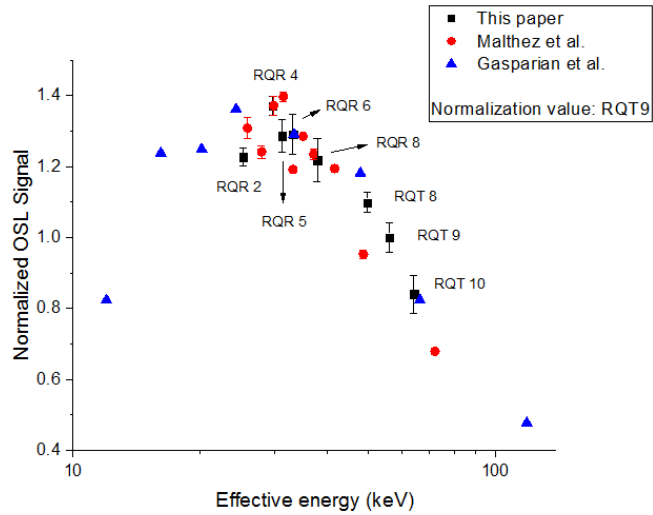


Figure 4.2 - Energy responses obtained for 8 different x-ray beam qualities. The mean OSL signal obtained for each quality was normalized to the mean OSL signal obtained for the RQT 9 x-ray beam quality. The other two symbols correspond to the energy responses for the  $\text{Al}_2\text{O}_3:\text{C}$  Luxel dosimeters obtained in distinct works. These data were normalized to the data obtained in this work for comparison and presented similar energy-dependent response.

### 3. Linearity of Response

The results of the OSL signal dependence to the air kerma, using the MCN 421 x-ray tube and the 30 cc ionization chamber, are presented in Figure 4.3. The  $R^2$ -coefficient was 0.9998, indicating that the OSL responses were linear with air kerma in this range of values.

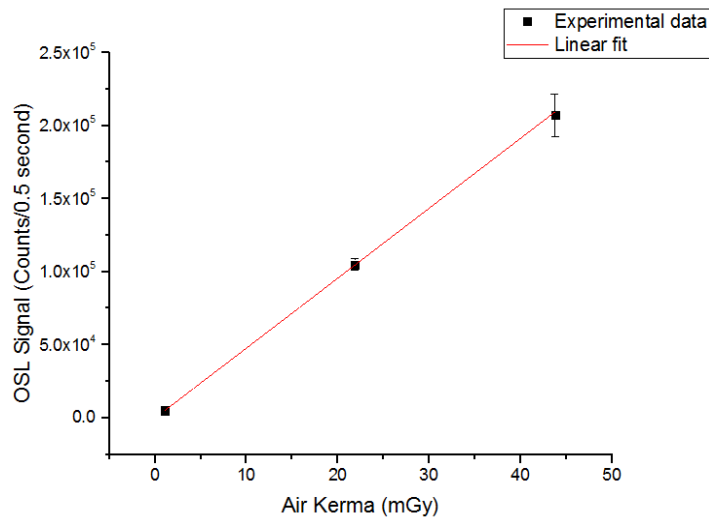


Figure 4.3 - Example of the linearity of the OSL response to the air kerma measured by a 30 cc ionization chamber and the MCN 421 x-ray tube with RQT 9 quality.

Similar behavior was found when the 0.6 cc ionization chamber was used in the MCN 421 x-ray tube and the Philips Brilliance 64 CT scanner together with TLDs and OSLDs. However, the slope of the curve obtained with the x-ray tube was 10% higher than the one

obtained with the CT scanner for the TLDs and 8% higher for the OSLDs (Figure 4.4). Results obtained for the linearity evaluation are summarized in Table 4.1 for both TLD and OSLD.

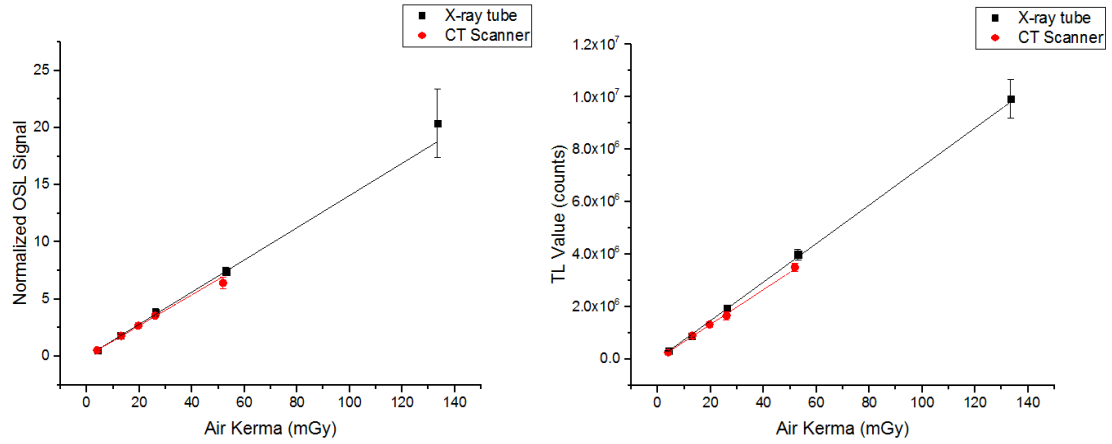


Figure 4.4 - Comparison of the linearity responses of the OSLDs (left) and TLDs (right) to the air kerma measured by a 0.6 cc ionization chamber in the MCN 421 x-ray tube and in the CT scanner. After extracting the OSL signal, each OSLD was irradiated with beta radiation in the Risø reader and their responses to beta radiation were used to normalize the OSL signal. TL value is given by the integral of the TL curve from 0°C to 350°C.

Table 4.1 - Linearity response parameters obtained for distinct situations.

Source	Ionization Chamber (IC)	Dosimeter	Distance source-IC/Dosimeter [m]	Slope [counts/mGy]	R <sup>2</sup>
x-ray tube	30 cc	OSLD	5	$(4.78 \pm 0.02) \times 10^2$	0.9999
x-ray tube	0.6 cc	OSLD	1	$0.141 \pm 0.002^i$	0.9986
CT scanner	0.6 cc	OSLD	Center of the gantry	$0.135 \pm 0.002^i$	0.9990
x-ray tube	0.6 cc	TLD	1	$(73.5 \pm 1.8) \times 10^3$	0.9992
CT scanner	0.6 cc	TLD	Center of the gantry	$(66.2 \pm 0.9) \times 10^3$	0.9975

i. OSL signal normalized to beta radiation

Considering the linearity obtained with this analysis, calibration curves (air kerma × dosimeter response) applied to evaluate organ doses in-phantom were constructed with the same CT scanner used in the measurements with the phantoms. One calibration curve per set of measurements was constructed and they are described in Section 4.4.

#### 4. Reproducibility and Reusability

Figure 4.5 presents the results of the reproducibility test for Groups 1, 2 and 3 as described in Table 3.3. After each exposure under the same conditions, mean, standard deviation and CV for each group were recorded. OSL signals from each group were normalized so that their CV could be comparable. This study indicated a variation among irradiations from 3% to 5% for Group 1, from 4% to 5% for Group 2 and from 1% to 2% for Group 3. Figure 4.5 highlights these quantities, showing a significantly decrease on the uncertainties when the OSL signals were normalized by their responses using beta radiation.

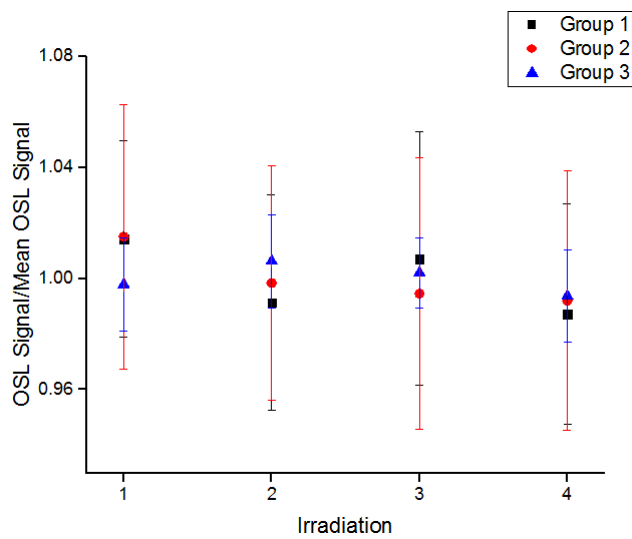


Figure 4.5 - Reproducibility test for the three groups. Results were normalized to highlight the standard deviation ( $k=1$ ) of the measurements inside each group. It is possible to notice that the variations are significantly lower when OSL signals were normalized to the dosimeters responses to beta radiation.

During the process of irradiating and erasing the 24 dosimeters from the three groups, each dosimeter was identified and their signal was individually recorded along the readings to assess reusability. After performing 4 cycles (Table 3.3), CV values varied from 1% to 4% for dosimeters from Groups 1 and 2 and from 1% to 2% for dosimeters from Group 3. CV values per dosimeter and groups are presented in Figure 4.6. Data presented in Figure 4.5 and Figure 4.6 are shown in APPENDIX D.

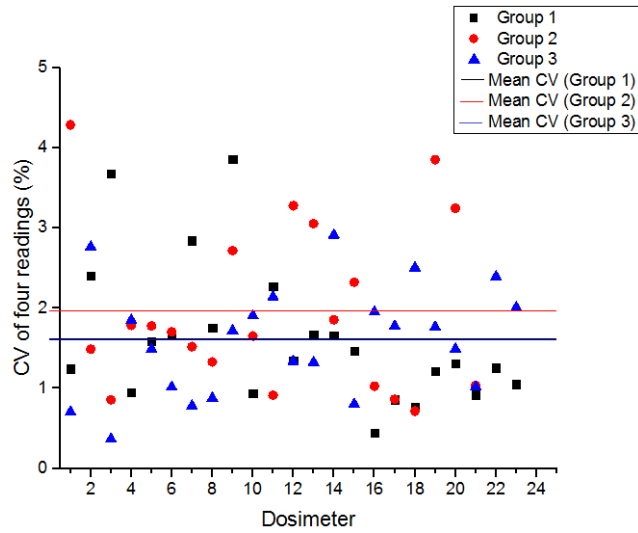


Figure 4.6 – Reusability test performed with dosimeters from the three groups. CV of four readings per dosimeter are presented. Horizontal lines indicate the mean CVs of each group.

Dosimeter responses from three groups are presented in box plots per irradiation in Figure 4.7. The absence of outliers in dosimeter responses from Group 3 highlights the efficacy of individually normalizing the OSL signals per their responses to beta radiation. Dosimeter responses from Groups 1 and 2 presented outliers in all readings.

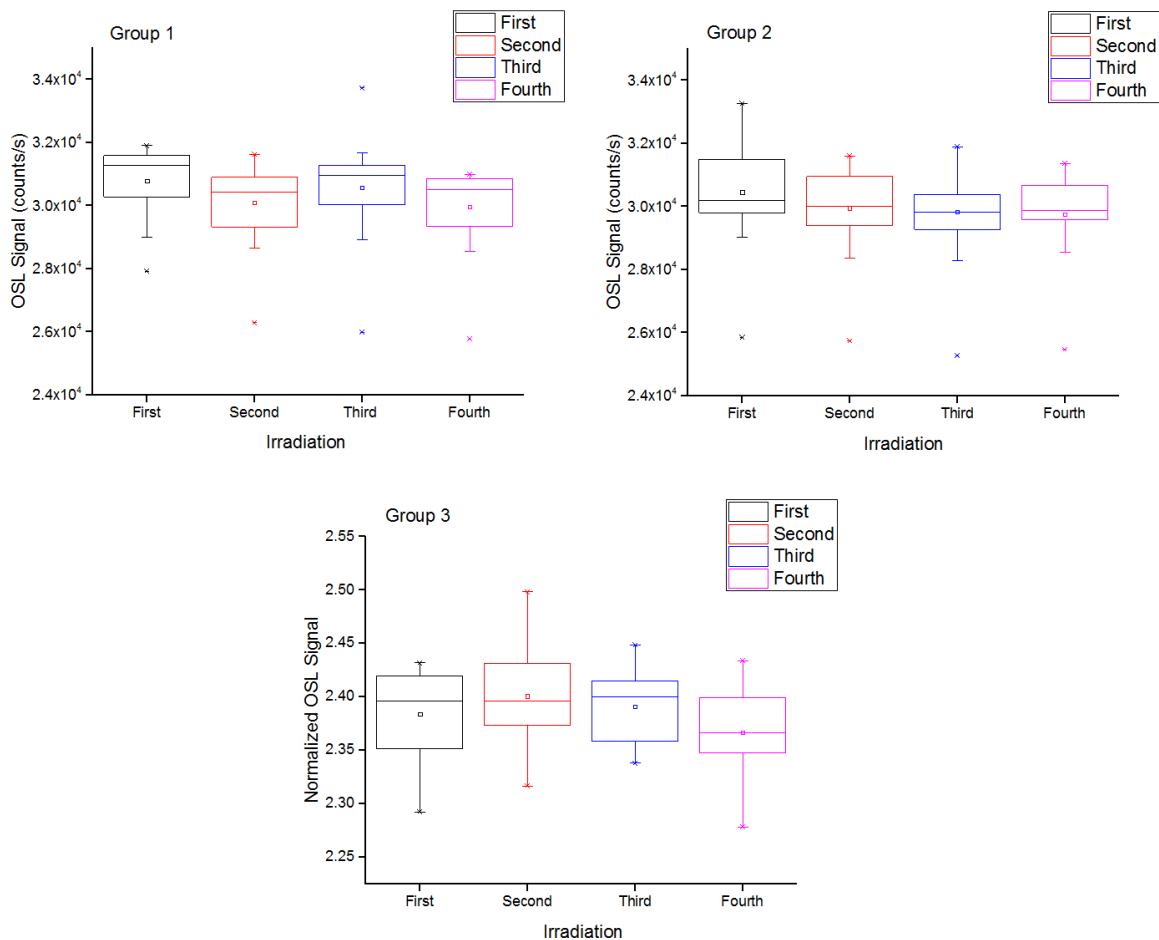


Figure 4.7 – Dosimeter responses per irradiation for groups 1 and 2 and normalized OSL signal for group 3. For each data set, whiskers present the variation range (minimum and maximum values), box contains 50% of data (75% - 25%), the horizontal line inside the box represents the median value of the responses and the square represents the mean value of the data. Groups 1 and 2 presented outliers.

## 4.2. SELECTION OF CT SCANNING PROTOCOLS

An evaluation of the CT examinations was conducted at InRad in order to identify the most frequent CT studies performed at this Institution in the years 2014, 2015 and 2016. During 2015, for instance, more than 50 modalities of CT studies, performed at the partner hospital in about 84,000 patients, were identified. From this large number, only about 3,300 patients were pediatric patients in the age range 0-15 years old. Figure 4.8 presents the ten most applied procedures in these patients, where one can notice that head CT examinations correspond to 42% of the total examinations and thorax CT is the 5<sup>th</sup> most applied procedure, corresponding to 5% of the total examinations. Similar trend was found for the years 2014 and 2016 (Figure 4.8).

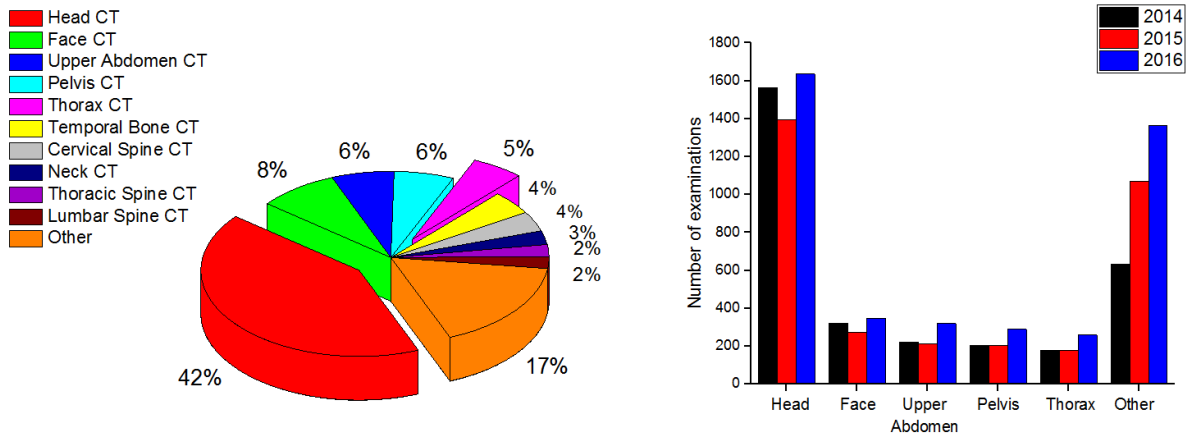


Figure 4.8 – Left: ten most applied CT examinations performed in pediatric patients at the Institute of Radiology of the School of Medicine of the University of São Paulo (InRad/FMUSP) in 2015. Head CT corresponds to 42% of the total examinations and Thorax CT is the 5<sup>th</sup> most applied protocol, corresponding to 5% of the total examinations. Right: Five most applied CT procedures during 2014-2016.

Considering adult patients, Head CT was the most applied examination in 2015, corresponding to 22% of the total, and Thorax CT was the 4<sup>th</sup> most applied, corresponding to 12%. Ten most applied adult CT studies performed at the Institute of Radiology of the School of Medicine of the University of São Paulo are presented in Figure 4.9. Similar trend was found in 2014 and 2016.

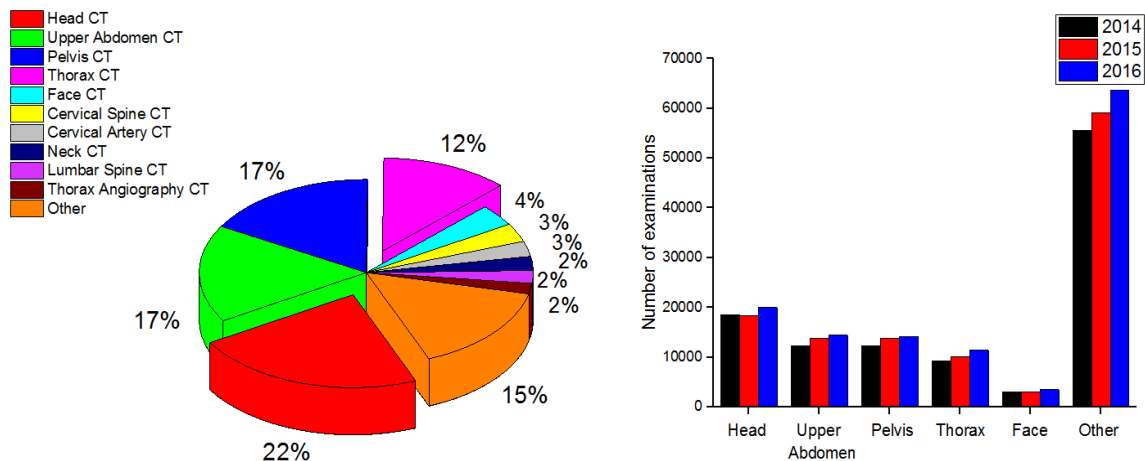


Figure 4.9 – Left: ten most applied CT examinations performed in adult patients at the Institute of Radiology of the School of Medicine of the University of São Paulo (InRad/FMUSP) in 2015. Head CT corresponds to 22% of the total examinations and Thorax CT is the 4<sup>th</sup> most applied protocol, corresponding to 12% of the total examinations. Right: five most applied CT procedures during 2014-2016.

### 4.3. ORGAN VOLUMES DETERMINATION FOR ADULT AND PEDIATRIC PHANTOMS

#### 4.3.1. The RANDO Phantom

The fractional volumes of the organs of interest inside each slice of the phantom, used in the present work, were determined by Huda & Sandison (1984) and by Golikov & Nikitin (1989), as it was described in Section 3.2.3.1. For the thyroid,  $f_i$  reduces to unity and it is located inside the 9<sup>th</sup> slice of the phantom. For the lungs and liver, results are presented in Table 4.2.

Table 4.2 - Lung and liver mass fraction,  $f_i$ , inside each slice  $i$  of the adult anthropomorphic RANDO phantom (Golikov & Nikitin, 1989; Huda & Sandison, 1984).

Slice ( $i$ )	Organ	$f_i$
10		0.01
11		0.05
12		0.09
13		0.11
14	Lungs	0.14
15		0.14
16		0.13
17		0.13
18		0.11
19		0.07
20		0.02
19	Liver	0.15
20		0.29
21		0.27
22		0.17
23		0.09
24		0.03

Note: Lung mass fractions reprinted from Huda & Sandison (1984). Liver mass fractions reprinted from Golikov & Nikitin (1989).

In addition, the system developed by Golikov & Nikitin (1989) for localizing the liver inside one slice is demonstrated in Figure 4.10. These authors present the location of the liver by using this system from slice 19 to slice 24 along with the liver mass fraction.

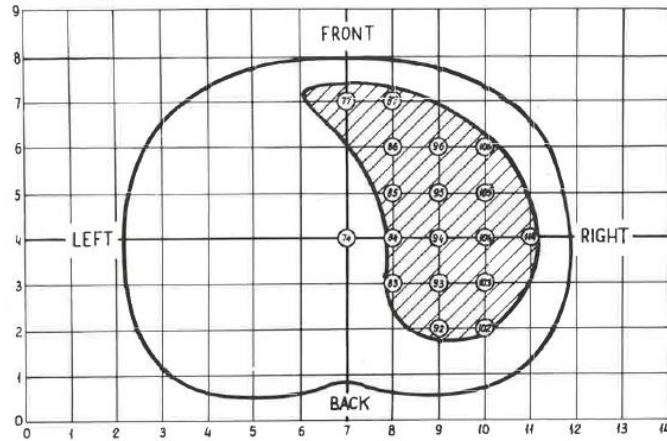


Figure 4.10 - Organ and dosimeter holes localization as proposed by Golikov & Nikitin (1989). Note: Reprinted from Golikov & Nikitin (1989).

#### 4.3.2. The CIRS ATOM Model 705 Phantom

The fractional volumes of the organs of interest inside each slice of the phantom, used in the present work, were determined using a threshold algorithm (in case of the lungs) (Giansante et al., 2016) and the software iSite Radiology (in case of the liver), as it was described in Section 3.2.3.2. For the thyroid,  $f_i$  reduces to unity and it is located inside the 8<sup>th</sup> slice of the phantom (Inkoom et al., 2015).

Since there is no information about the location of the liver inside the phantom, it was determined by analyzing patient data information and the study developed by Inkoom et al. (2015). In this study, the abdominal region of each patient was separated in 25 mm intervals. The liver of each patient was within a 125 mm region, starting approximately in the level of the hemi-diaphragm (Inkoom et al., 2015) and corresponding to 5 physical phantom slices. In the study conducted by Inkoom et al., these authors found the liver to be inside the slices 15-19. Therefore, the volume per 25 mm interval per patient is presented in Table 4.3.

Table 4.3 – Liver volume per 25 mm interval ( $\text{cm}^3$ ) obtained for five patients with the software iSite Radiology (Philips, Germany). These quantities were used as an approximate estimative of the fractions of this organ inside each slice of the anthropomorphic physical phantom. Each interval corresponds to a 25 mm section of the patient containing the liver, corresponding to the 5 physical phantom slices that contains the liver according to Inkoom et al. (2015).

<b>Volume (<math>\text{cm}^3</math>)</b>					
	<b>Patient 1 (3 years old)</b>	<b>Patient 2 (3 years old)</b>	<b>Patient 3 (4 years old)</b>	<b>Patient 4 (5 years old)</b>	<b>Patient 5 (5 years old)</b>
<b>Interval 1</b>	36.0	85.0	127.0	97.0	94.0
<b>Interval 2</b>	188.7	224.5	215.4	237.0	252.7
<b>Interval 3</b>	168.8	199.0	179.6	196.1	191.2
<b>Interval 4</b>	100.5	93.8	73.3	134.1	96.6
<b>Interval 5</b>	31.0	36.7	24.0	80.5	20.9
<b>Total</b>	525.0	639.0	619.3	744.7	655.4

The quantities presented in Table 4.3 were used to evaluate the fraction of the volume of the liver inside each interval per patient. The average of the fractions per interval were adopted as the liver volume fractions of the phantom.

Results obtained for lung and liver fractions per slice for the CIRS ATOM model 705 anthropomorphic phantom, along with the uncertainties, are presented in Table 4.4. The contribution of the liver volume in the 5<sup>th</sup> interval was added to the 4<sup>th</sup> interval to perform the liver doses evaluation.

Table 4.4 – Lung and liver mass fraction,  $f_i$ , inside each slice  $i$  of the CIRS ATOM pediatric anthropomorphic phantom estimated with a threshold algorithm (lung) and with the iSite Radiology software along with their uncertainties. Confidence level considered is 68.3% ( $k = 1$ ).

<b>Slice (<math>i</math>)</b>	<b>Organ</b>	<b><math>f_i</math></b>
9	Lungs	0.021±0.003
10		0.137±0.025
11		0.198±0.018
12		0.217±0.015
13		0.228±0.013
14		0.172±0.021
15		0.027±0.002
15	Liver	0.136±0.025
16		0.352±0.012
17		0.296±0.011
18		0.216±0.021

#### 4.4. ORGAN DOSES EVALUATION

Organ doses were evaluated in pediatric and adult anthropomorphic phantoms, according to each protocol and to the methodology described. The linearity of the TLD responses to the air kerma was evaluated by Martins (2015), and the linearity of the OSLD responses to the air kerma was evaluated in this study (see Section 4.1). Therefore, dosimeters were calibrated free-in-air and calibration curves were constructed in order to convert the OSLD and TLD readings to air kerma and, then, to organ doses, as described in Section 3.2.5. One calibration curve per kind of dosimeter was constructed in all set of measurements. The OSLD signals considered are the OSL responses to x-ray normalized to their responses to beta radiation. Calibration curves for this dosimeter were constructed by considering the normalized signal in every measurement.

##### 4.4.1. Thorax

The first protocol studied was the *Thorax for Children*, as previously described, and it was applied to the pediatric phantom. A set of 180 TLDs and 144 OSLDs were distributed in 36 dosimeter holders that were used to estimate absorbed organ doses due to this protocol. Doses to the lungs and thyroid were evaluated, since these organs were irradiated by the primary beam of the CT scanner. Results are presented in Table 4.5 along with other dosimetric quantities ( $CTDI_{vol}$ , DLP, organ dose/mAs, organ dose/mAs<sub>eff</sub>, and organ dose/ $CTDI_{vol}$ ). Table 4.5 also presents the calibration curves for each kind of dosimeter.

Table 4.5 – Calibration curves, organ doses and dosimetric quantities for the Thorax for children protocol applied to the CIRS ATOM pediatric phantom.

<b>Thorax for children</b>			
<b>Calibration curves</b>	$K_{air}[mGy] = (1.513 \pm 0.023) \times 10^{-5}(TL \text{ value})$		
	$K_{air}[mGy] = (7.43 \pm 0.15) \times (OSL \text{ signal})$		
<b>CT scanner dosimetric quantities</b>			
	CTDI <sub>vol</sub> (mGy)	7.0	
	DLP (mGy.cm)	196.3	
<b>Measured quantities</b>			
<b>Organ</b>	<b>Dosimetric Quantity</b>	<b>Dosimeter type</b>	
		<b>TLD</b>	<b>OSLD</b>
<b>Thyroid</b>	Organ Dose (mGy)	6.79±0.08	7.26±0.19
	Organ Dose/mAs (mGy/mAs)	0.123±0.002	0.132±0.003
	Organ Dose/mAs <sub>eff</sub> (mGy/mAs <sub>eff</sub> )	0.114±0.001	0.122±0.003
	Organ Dose/CTDI <sub>vol</sub> (mGy/mGy)	0.969±0.012	1.038±0.027
<b>Lungs</b>	Organ Dose (mGy)	6.10±0.30	6.00±0.30
	Organ Dose/mAs (mGy/mAs)	0.111±0.005	0.109±0.005
	Organ Dose/mAs <sub>eff</sub> (mGy/mAs <sub>eff</sub> )	0.102±0.004	0.100±0.004
	Organ Dose/CTDI <sub>vol</sub> (mGy/mGy)	0.870±0.040	0.850±0.040

#### 4.4.2. Thorax, abdomen and pelvis

The second protocol studied was the *Thorax, abdomen and pelvis (3 phases)* and it was applied to both phantoms (Section 3.2.4). Sets of 112 TLDs and 112 OSLDs were distributed in 56 dosimeter holders that were used to estimate organ doses due to this protocol in the pediatric phantom and 132 TLDs and 132 OSLDs were distributed in 66 dosimeter holders to estimate doses in the adult phantom. Calibration curves, doses to the lungs, liver and thyroid were evaluated for both phantoms. Results are presented in Table 4.6 along with other dosimetric quantities (CTDI<sub>vol</sub>, DLP, organ dose/mAs, organ dose/mAs<sub>eff</sub> and organ dose/CTDI<sub>vol</sub>). CTDI<sub>vol</sub> and DLP are presented for one phase and organ doses are presented for the three phases of the examination.

Table 4.6 – Calibration curves, organ doses and dosimetric quantities for the Thorax, abdomen and pelvis protocol applied to the RANDO adult phantom and to the CIRS ATOM pediatric phantom. Although 3 phases were performed with the same parameters, usually only one phase is applied for adult and pediatric phantoms. When more than one phase is applied, it is only for the abdominal region of the patient. Moreover, in a clinical examination TCM is commonly applied.

<b>Thorax, abdomen and pelvis (3 phases)</b>					
$K_{air}[mGy] = (1.356 \pm 0.025) \times 10^{-5}(TL \text{ value})$					
<b>Calibration curves</b>					
$K_{air}[mGy] = (6.70 \pm 0.04) \times (OSL \text{ signal})$					
		<b>The RANDO Phantom</b>		<b>The CIRS ATOM Phantom</b>	
<b>CT scanner dosimetric quantities</b>		CTDI <sub>vol</sub> (mGy)	6.5	CTDI <sub>vol</sub> (mGy)	2.6
		DLP (mGy.cm)	494.5	DLP (mGy.cm)	138.0
<b>Measured quantities</b>					
<b>Organ</b>	<b>Dosimetric Quantity</b>	<b>Dosimeter type</b>		<b>Dosimeter type</b>	
		<b>TLD</b>	<b>OSLD</b>	<b>TLD</b>	<b>OSLD</b>
	Organ Dose (mGy)	11.70±0.50	12.13±0.33	17.43±0.07	15.74±0.28
	Organ Dose/mAs (mGy/mAs)	0.117±0.005	0.121±0.003	0.447±0.002	0.404±0.007
	<b>Thyroid</b> Organ Dose/mAs <sub>eff</sub> (mGy/mAs <sub>eff</sub> )	0.137±0.006	0.142±0.004	0.523±0.002	0.473±0.009
	Organ Dose/CTDI <sub>vol</sub> (mGy/mGy)	1.800±0.070	1.870±0.050	6.700±0.030	6.060±0.110
	Organ Dose (mGy)	24.11±0.110	24.33±0.150	13.01±0.55	12.60±0.50
	Organ Dose/mAs (mGy/mAs)	0.241±0.001	0.243±0.002	0.334±0.014	0.323±0.014
	<b>Lungs</b> Organ Dose/mAs <sub>eff</sub> (mGy/mAs <sub>eff</sub> )	0.283±0.001	0.285±0.002	0.391±0.017	0.378±0.016
	Organ Dose/CTDI <sub>vol</sub> (mGy/mGy)	3.708±0.016	3.743±0.024	5.000±0.210	4.840±0.210
	Organ Dose (mGy)	26.86±0.18	26.26±0.21	13.00±0.50	13.50±0.60
	Organ Dose/mAs (mGy/mAs)	0.269±0.002	0.263±0.002	0.335±0.014	0.346±0.015
	<b>Liver</b> Organ Dose/mAs <sub>eff</sub> (mGy/mAs <sub>eff</sub> )	0.315±0.002	0.308±0.003	0.392±0.017	0.406±0.017
	Organ Dose/CTDI <sub>vol</sub> (mGy/mGy)	4.132±0.027	4.041±0.033	5.020±0.210	5.200±0.220

#### 4.4.3. Head/Head and Neck

The third protocol studied was the *Head (3D)* as previously described, and it was applied to both phantoms. A set of 14 TLDs and 14 OSLDs were distributed in 8 dosimeter holders that

were used to estimate absorbed organ doses due to this protocol in the pediatric phantom and 10 TLDs and 10 OSLDs were distributed in 6 dosimeter holders to estimate doses in the adult phantom. Doses to the eye lenses and thyroid were evaluated for both phantoms. Head and neck CT was performed in the CIRS ATOM phantom and head CT was performed in the RANDO phantom. Results are presented in Table 4.7 along with other dosimetric quantities ( $CTDI_{vol}$ , DLP organ dose/mAs, organ dose/mAs<sub>eff</sub> and organ dose/ $CTDI_{vol}$ ).

Table 4.7 - Calibration curves, organ doses and dosimetric quantities for the Head/Head and Neck protocol applied to the RANDO adult phantom and to the CIRS ATOM pediatric phantom.

<b>Head 3D</b>					
<b>Calibration curves</b>		$K_{air}[mGy] = (1.39 \pm 0.03) \times 10^{-5}(TL \text{ value})$			
		$K_{air}[mGy] = (7.57 \pm 0.12) \times (OSL \text{ signal})$			
<b>CT scanner dosimetric quantities</b>		<b>The RANDO Phantom</b>		<b>The CIRS ATOM Phantom</b>	
		$CTDI_{vol}$ (mGy)	38.7	$CTDI_{vol}$ (mGy)	38.7
		DLP (mGy. cm)	860.0	DLP (mGy. cm)	1103.0
<b>Measured quantities</b>					
<b>Organ</b>	<b>Dosimetric Quantity</b>	<b>Dosimeter type</b>		<b>Dosimeter type</b>	
		<b>TLD</b>	<b>OSLD</b>	<b>TLD</b>	<b>OSLD</b>
	Organ Dose (mGy)	5.32±0.150	6.80±0.20	40.65±0.76	43.04±0.65
	Organ Dose/mAs (mGy/mAs)	0.028±0.001	0.023±0.001	0.136±0.003	0.144±0.002
<b>Thyroid</b>	Organ Dose/mAs <sub>eff</sub> (mGy/mAs <sub>eff</sub> )	0.005±0.001	0.007±0.001	0.041±0.001	0.043±0.001
	Organ Dose/ $CTDI_{vol}$ (mGy/mGy)	0.137±0.004	0.176±0.005	1.050±0.020	1.112±0.017
	Organ Dose (mGy)	26.10±1.40	26.39±0.91	28.70±3.00	32.69±0.28
	Organ Dose/mAs (mGy/mAs)	0.087±0.005	0.088±0.003	0.096±0.010	0.109±0.001
<b>Eye Lenses</b>	Organ Dose/mAs <sub>eff</sub> (mGy/mAs <sub>eff</sub> )	0.026±0.001	0.026±0.001	0.029±0.003	0.033±0.001
	Organ Dose/ $CTDI_{vol}$ (mGy/mGy)	0.680±0.040	0.680±0.030	0.742±0.077	0.845±0.007

#### 4.5. COMPARISON OF PEDIATRIC PATIENT DATA WITH INTERNATIONAL DRL

##### 1. Head CT

Data from 20 pediatric patients per age range were assessed. These patients performed Head CT in the Philips Brilliance 64 CT scanner dedicated to emergency during 2014-2016. Median values of  $CTDI_{vol}$  for each phase and DLP for the whole examination per age range are presented in Table 4.8, along with DRL from three international surveys (European Society of Radiology, 2015; Shrimpton et al., 2014; Vassileva et al., 2015).  $CTDI_{vol}$  are displayed for a 16-cm phantom. Median values were used rather than mean as the representative values for each age group due to the presence of outliers.

Europe survey was performed by considering weight group instead of age (European Society of Radiology, 2015). The authors present a table with approximate equivalence of weight and age groups for the purpose of comparing age-based DRL with weight-based DRL. Values for the second age group, however, are considered for patients from 1 to 4 years old instead of 1 to 5 years old. Similarly, the third age group in that work corresponds to patients from 4 to 10 years old. The second age group corresponds to early adolescents, from 10 to 14 years old.

Table 4.8 –  $CTDI_{vol}$  and DLP median values for Head CT examinations obtained with patient data collected in the present work. DRL from three different surveys are presented for comparison.

Age group (y)	$CTDI_{vol}$ , mGy				DLP, mGy cm			
	This work	Vassileva et al. (2015)	Europe (2015)	UK (2014) <sup>i</sup>	This work	Vassileva et al. (2015)	Europe (2015)	UK (2014) <sup>i</sup>
0 - < 1	25	26	25	25	478	440	300	350
1 - < 5	26	36	25	40	564	540	370	650
5 - < 10	35	43	38	60	554	690	505	860
10 - < 16	43	53	53	-	652	840	700	-

i. Pediatric DRL are only established for the first three age ranges presented (0 - < 1 y, 1 - < 5 y, 5 - < 10 y) in the UK survey.

Data collected from all patients are presented in box plots in Figure 4.11 per age range for both  $CTDI_{vol}$  (mGy) and DLP (mGy.cm).

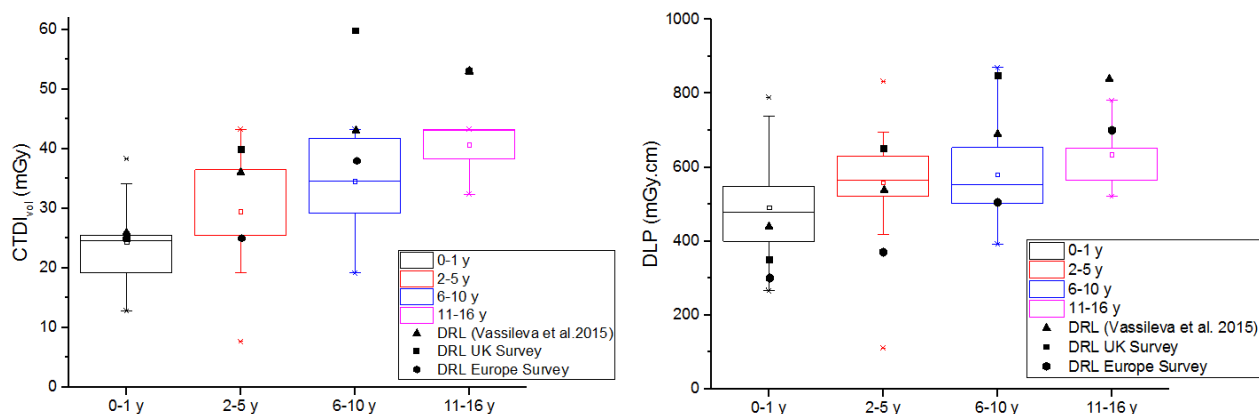


Figure 4.11 – Box plots for  $CTDI_{vol}$  and DLP obtained from patient data collected from 2014 to 2016 for Head CT performed at InRad. For each data set, whiskers present the variation range (minimum and maximum values), box contains 50% of data (75% - 25%), the horizontal line inside the box represents the median value and the square represents the mean value of the data. International DRL from three surveys are also presented.  $CTDI_{vol}$  for 0-1 y age range and DLP values for 0-1 y and 2-5 y age ranges present outliers. On the horizontal axes, age ranges are presented.

## 2. Thorax CT

Fourteen patients were assessed in the age range 0 - < 1 year old, seventeen in the age range 1 - < 5 years old, six in the age range 5 - < 10 years old and fifteen in the age range 10 - < 16 years old. These patients performed Thorax CT in the Philips Brilliance 64 CT scanner dedicated to routine examinations during 2014-2016. Median values of  $CTDI_{vol}$  for each phase and DLP for the whole examination per age range are presented in Table 4.9, along with DRL from three international surveys (European Society of Radiology, 2015; Shrimpton et al., 2005; Shrimpton et al., 2014; Vassileva et al., 2015).  $CTDI_{vol}$  are displayed for a 32-cm phantom in the three surveys. In the present work, however,  $CTDI_{vol}$  values for patients in the age range 0 - < 1 year old were displayed in terms of a 16-cm phantom. To compare these values with the international surveys, a correction factor of 0.52 was applied to each  $CTDI_{vol}$  and DLP recorded in this age range, according to a test performed by the Quality Control group of IFUSP in this equipment<sup>j</sup>. Thorax, abdomen and pelvis procedures were excluded from this analysis because such protocol requires specific values of DRL.

<sup>j</sup> Courtesy: Denise Y. Nersissian (IFUSP)

Table 4.9 - CTDI<sub>vol</sub> and DLP median values for Thorax CT examinations obtained with patient data collected in the present work. DRL from three different surveys are presented for comparison.

Age group (y)	CTDI <sub>vol</sub> , mGy				DLP, mGy cm			
	This work	Vassileva et al. (2015)	Europe (2015)	UK (2014) <sup>i</sup>	This work	Vassileva et al. (2015)	Europe (2015)	UK (2014) <sup>i</sup>
0 - < 1	2.8	5.2	2.7	6.0	69	130	45	100
1 - < 5	2.9	6.0	3.3	6.5	77	140	80	115
5 - < 10	4.5	6.8	5.6	10.0	154	170	115	185
10 - < 16	4.6	7.3	5.7	-	186	300	180	-

i. Pediatric DRL are only established for the first three age ranges presented (0 - < 1 y, 1 - < 5 y, 5 - < 10 y) in the UK survey.

Data collected from all patients are presented in box plots in Figure 4.12 per age range for both CTDI<sub>vol</sub> (mGy) and DLP (mGy.cm).

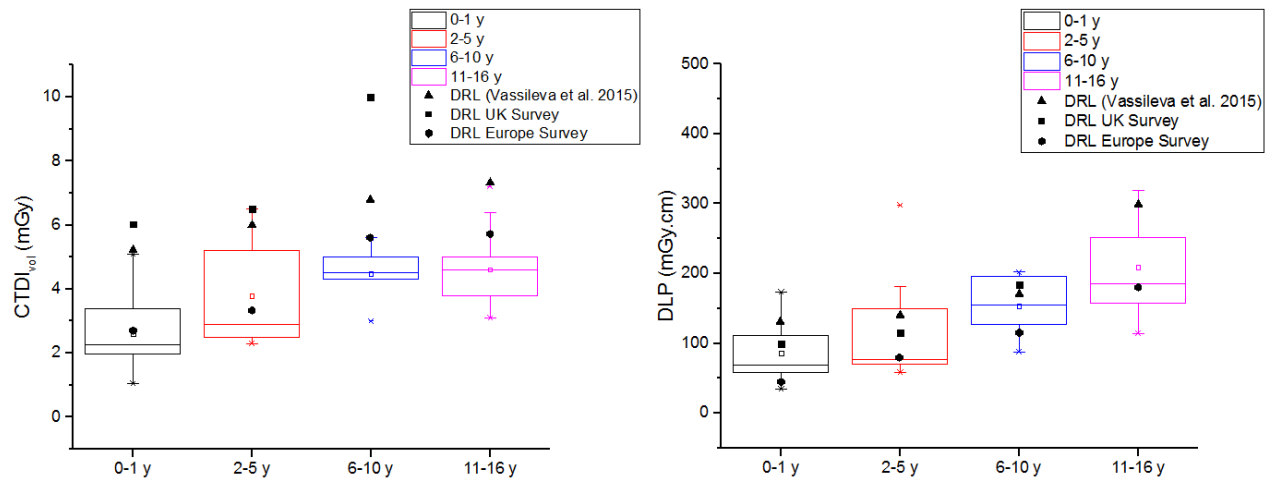


Figure 4.12 – Box plots for CTDI<sub>vol</sub> and DLP obtained from patient data collected from 2014 to 2016 for Thorax CT performed at InRad. For each data set, whiskers present the variation range (minimum and maximum values), box contains 50% of data (75% - 25%), the horizontal line inside the box represents the median value and the square represents the mean value. International DRL from three surveys are also presented. CTDI<sub>vol</sub> for 6-10 y age range and DLP values for 2-5 y age ranges present outliers. On the horizontal axes, age ranges are presented.

## 5. DISCUSSION

The main objective of the present study was the evaluation of organ absorbed doses due to clinical CT procedures conducted in a clinical institution. This study was performed by applying TL and OSL dosimeters in anthropomorphic phantoms and organ doses due to protocols routinely applied were assessed. TL dosimeters applicability for CT dose measurements was evaluated in a previous work (Martins, 2015), but OSL dosimeters were evaluated in the present study to verify their behavior when exposed to CT beams. Additionally, data from about 120 pediatric patients were collected and analyzed in terms of CT dose indexes so that pediatric patient data could also be compared with international DRLs. Protocol selection was performed after this analysis. Target organs were chosen in terms of their radiosensitivity and the protocols selected.

### 5.1. OSLD CHARACTERIZATION

The use of OSL technique has increased in several fields over the last years (Yukihara, McKeever, & Akselrod, 2014). In the literature, it is possible to find several works performed with different OSL materials in a wide range of applications. Lavoie et al. (2011), for instance, evaluated the Landauer nanoDot Al<sub>2</sub>O<sub>3</sub>:C dosimeter to verify the applicability of this system to evaluate doses from CT procedures. Al-Senan et al. (2012) evaluated thyroid doses from CT by measuring neck surface dose in 25 pediatric patients using the same Landauer nanoDot Al<sub>2</sub>O<sub>3</sub>:C. Kumar et al. (2015) evaluated the OSL response of several materials, including BaFCl:Eu, Al<sub>2</sub>O<sub>3</sub>:C and K<sub>2</sub>Ca<sub>2</sub>(SO<sub>4</sub>)<sub>3</sub> in terms of different doses and bleaching times. Recently, Ponmalar et al. (2017) performed the characterization of the Landauer nanoDots for usage in clinical radiotherapy measurements. Results reported by these authors and many others in the literature indicate that this dosimetry technique offers many advantages compared with others, such as efficiency, accuracy, linearity, and good spatial resolution.

In the present study, batch homogeneity, energy response, linearity of dose response, reproducibility, reusability, and effect of uncertainties with the normalization of OSL signals per their response to beta radiation were evaluated for the Al<sub>2</sub>O<sub>3</sub>:C OSLD Landauer Luxel™ tape (Landauer, Inc., Glenwood, USA). Results are discussed below.

#### 1. Batch Homogeneity

The homogeneity of the OSLD was tested with a batch composed of 452 disks with 3 mm diameter that were manually fractionated (Section 3.1.3). Dosimeter responses presented approximately a Gaussian behavior with average 85021 and standard deviation of 4018, which was verified by statistical tests (APPENDIX C). The standard deviation corresponded to 4.7% of the average, demonstrating that most dosimeters responded in a similar way under the same irradiation conditions. Given the possible differences in dosimeters shape, size, and uniformity due to their small size and due to the manually fractioning process, a 4.7% variation is considered small.

In the study conducted by Al-Senan & Hatab (2011), the authors evaluated the characteristics of the  $\text{Al}_2\text{O}_3:\text{C}$  Landauer nanoDot in the diagnostic energy range. Despite being produced with the same material as the Landauer Luxel<sup>TM</sup> tape used in this work, Landauer provides nanoDots in a 2-mm disk with technical specification that includes precision, accuracy and sensitivity (Landauer Inc, 2012). In the cited work, the authors assessed the homogeneity of a 47 dosimeters batch using 25, 80 and 120 kVp. The relative standard deviation of the 47 dosimeter readings in these cases was 4.4, 4.8 and 4.3%, respectively. The authors described this variation as excellent, considering a 2% variation of the irradiating beam (Al-Senan & Hatab, 2011). The uniformity of the OSL Luxel<sup>TM</sup> tape was investigated by Gasparian (2009). The author performed this analysis in OSL strips cut from the original tape irradiated using a linear accelerator with photon energy of 6 MeV. Results reported by these authors indicated that the aluminum oxide powder in the OSL strip was not homogeneously distributed. The author also states that in terms of CT dose profiles measurements, this non-uniformity did not affect the results (Gasparian, 2009). Recently, Han et al. (2016) evaluated the characteristic of a 5-mm Landauer nanoDot for a 80 kV cephalometric exposure. Homogeneity was evaluated for a 25 dosimeters batch and the authors reported a variation of 1.67%.

## 2. Energy Response

The energy response of the dosimeters to different x-ray beam qualities is presented in Figure 4.2. In CT procedures, 120 kV is the most commonly applied tube voltage for adult protocols; however, lower tube voltages such as 100 kV, 90 kV, or 80 kV are also routinely used, depending on the clinical procedure and on the anatomy of the patient, especially in pediatric CT. For each case, there is a different value of HVL, which makes the evaluation of the behavior of the dosimeters necessary under these circumstances (Lavoie et al., 2011).

Eight groups of three dosimeters were irradiated with different x-ray beam qualities using the MCN 421 x-ray tube. The OSL signal for each quality was evaluated by calculating the average of the three responses, and the uncertainties were obtained as the standard deviation of the mean response ( $k = 1$ ). Responses of the dosimeters for the RQT 8, 9, and 10 beam qualities showed an approximately linear behavior, whereas those for the RQR 2, 4, 5, 6, and 8 followed a non-uniform energy dependence, similar to those found in the literature (Al-Senan & Hatab, 2011; Gasparian et al., 2012; Malthez et al., 2014).

Data from the present study were compared with data obtained by Gasparian et al. (2012) and by Malthez et al. (2014). Gasparian et al. investigated the responses of two types of OSLDs:  $\text{Al}_2\text{O}_3:\text{C}$  single crystals of 5 mm in diameter and 0.9 mm in thickness and  $\text{Al}_2\text{O}_3:\text{C}$  Luxel dosimeters of 7 mm in diameter and 0.3 mm in thickness. In order to read the information of the dosimeters, the authors also used a Risø TL/OSL reader, with green light stimulation. The irradiations were performed at the Belgian Nuclear Research Center with gamma and x-ray fields. Malthez et al. conducted similar analysis with five different TL/OSL materials, including the Luxel OSLD cut in 7 mm of diameter and 0.3 mm in thickness. Dosimeters were read with the same Risø TL/OSL reader used in the present study. To compare the results of this study with those obtained by the aforementioned authors, data of their work, provided by them, were normalized to the results of this study for a common energy, so that results could be comparable in the same graphic (Figure 4.2). The energy-dependent response observed in the results is consistent with the expected, based on the  $\text{Al}_2\text{O}_3:\text{C}$  mass energy absorption coefficient and effective number (Gasparian et al., 2012; Malthez et al., 2014) as it was previously explained (Section 2.7). This energy dependence in diagnostic energy range can be corrected with proper calibration (Gasparian, 2009).

### 3. Linearity of Response

As expected, dosimeters presented a linear response against air kerma in this energy range. The linearity of  $\text{Al}_2\text{O}_3:\text{C}$  dosimeters with dose was tested and reported by many authors (Al-Senan & Hatab, 2011; Han et al., 2016; Lavoie et al., 2011; Nascimento, Vanhavere, Souza, & Verellen, 2016). In the present study, linearity was assessed up to 130 mGy with a 30 cc ionization chamber, a 0.6 cc ionization chamber, a constant potential x-ray tube, and a 64-slice CT scanner. This range of air kerma complies with CT procedures, but a more extensive range of characterization is needed for other clinical applications. In the investigation conducted by Gasparian (2009) with the Landauer Luxel<sup>TM</sup> tape, dosimeters presented an approximate linear

response up until 10 Gy, with a small supralinearity observed above 5 Gy. The author observed this supralinearity until 100 Gy when the initial OSL signal was analyzed. Above 100 Gy, sublinearity was observed.

The linear response of the dosimeters indicates that these curves can be applied as calibration curves to convert dosimeter readings into air kerma values. However, one should note the discrepancies between the results obtained with the x-ray tube and the CT equipment, presented in Figure 4.4, which increase the uncertainties in the calculations. These experiments aimed to evaluate the applicability of the CT standard qualities with the MCN 421 x-ray tube – in the present study, the RQT 9 beam quality – to generate calibration curves. The standard qualities, such as RQT 9, are obtained to reach a nominal HVL (8.4 mmAl) by adding an external filtration (0.25 mm Cu + RQR 9 Al filtration) as proposed by the International Atomic Energy Agency Technical Series Report 457 (TRS 457) (IAEA, 2007). If the x-ray tube and the CT scanner beam qualities were the same, one could not expect discrepancies observed in Figure 4.4. This discrepancy is more evident in the range of higher values of air kerma (from 60 mGy to 130 mGy). The sources of this discrepancy are related to differences on the x-ray beams generated by these two equipment. According to TRS 457, and as previously described, RQT series simulate the non-attenuated beam used in CT procedures. The obtained results demonstrate that it is preferable to calibrate dosimeters with the same equipment used in the measurements.

#### 4. Reproducibility and Reusability

Reproducibility was assessed by evaluating the mean, standard deviation and CV of the 24 dosimeters per group in each one of the four experiments. CV values of the 24 dosimeter responses ranged from 3 to 5% for Group 1, from 4 to 5% for Group 2 and from 1 to 2% for Group 3 after four tests, indicating that they respond in a similar way. Lavoie et al. (2011) evaluated reproducibility of 3 Landauer nanoDot by recording mean, standard deviation and CV of the three dosimeters per reading. CV values in this case ranged from 1.7 to 5.1%.

Reusability was assessed by individually evaluating the responses of each dosimeter per group. After four experiments, CV values ranged from 1% to 4% for dosimeters from Groups 1 and 2 and from 1% to 2% for dosimeters from Group 3 (Figure 4.6). Lavoie et al. (2011) evaluated reusability for 3 Landauer nanoDots in 10 experiments. In that work, CV values were 3.1, 3.3 and 3.4% for each dosimeter after 10 tests. Han et al. (2016) assessed reusability for 25 Landauer nanoDots in 5 experiments. CV reported by these authors ranged from 0.18 to 1.56%.

Reproducibility and reusability tests conducted in this study demonstrated that this kind of dosimeters can be reused in subsequent radiations for low-dose procedures. There were no relevant differences in dosimeter responses after 4 consecutive irradiations and the 8-hour bleaching process proved to be efficient. When working with higher doses, however, a more extensive characterization is needed to ensure doses are properly erased.

Individual readings of each dosimeter can present a higher variation. As a consequence, it is recommended to use more than one dosimeter per exposure and to consider the standard deviation of their readings as a component of the uncertainty for a more reliable result. In addition, the comparative evaluation between the results obtained with dosimeters from Groups 1, 2, and 3 highlights the effect of normalizing each OSL signal ( $S_{x-ray}$ ) by their signal obtained after the irradiation with a beta source ( $S_{\beta}$ ). Since the “normalized OSL signal” is considered as the ratio  $\frac{S_{x-ray}}{S_{\beta}}$  for the same dosimeter and reader, dependence with the homogeneity of the crystals in the dosimeter, caused by the manual process of fractionating the tape, or stability of the reader, for instance, are taken into account and individually corrected. When performing this analysis, the construction of calibration curves needs to be performed with the same procedure. All the tests performed with the 3 groups presented a lower uncertainty for Group 3. The maximum CV obtained in the reproducibility test (Figure 4.5) for this group was 2%, whereas for Groups 1 and 2 it was 5%. Similarly, it is better to reuse a dosimeter and normalize it by its response to beta radiation. In this case, from the 24 dosimeters analyzed in Group 3, the maximum CV in four trials was 2% (Figure 4.6). Finally, when dosimeter responses were plotted in box charts (Figure 4.7), Groups 1 and 2 presented at least one outlier, which did not happen in Group 3.

## 5.2. SELECTION OF CT SCANNING PROTOCOLS

The evaluation of the CT examinations conducted at InRad showed that more than 50 modalities of CT studies are annually performed at the partner hospital. In 2015, 84,000 patients were identified, from which about 4% were pediatric patients (from 0 to 15 years old). Similarly, 95,000 patients were identified in 2016, from which less than 5% were pediatric patients. For both adult and pediatric patients, during 2014-2016, the most applied protocol was Head CT. In pediatric patients, this procedure is followed by Face CT, Upper Abdomen CT, Pelvis CT and Thorax CT. In 2015, Head CT corresponded to 42% of the total examinations, while Thorax CT was the 5<sup>th</sup> most applied, corresponding to 5% of the total. For adult patients,

Head CT is followed by Upper Abdomen CT, Pelvis CT, Thorax CT, and Face CT. In 2015, Head CT corresponded to 22% of the total and Thorax CT corresponded to 12% of the total.

An accurate protocol selection was performed by analyzing data from pediatric patients that performed Head CT and Thorax CT at InRad from 2014-2015, as previously described (Section 3.2.2). For Head CT, 20 patients per age range were analyzed. From the 20 patients in the first age range considered (0-1 year old), 17 of them performed helical CT and a total of 5 different protocols were identified. Two of these protocols were for children, two were infant protocols and one of them was an adult protocol. The most applied protocol in this age range was an infant helical protocol, applied in 8 from the 20 patients analyzed. For the 20 protocols applied in patients in the age range 1 - < 5 years old, 12 were helical and another 5 different protocols were identified: two adult protocols, two children protocols and one infant protocol. The most applied one was a children protocol, applied in 9 from the 20 patients. The third age range (5 - < 10 years old) had 4 helical procedures and 4 different protocols: two adult protocols, one for children and one for infant. The most applied was an adult protocol, in 14 from 20 patients. The last age range (11- < 16 years old) presented 20 helical procedures and only one adult protocol.

For thorax CT patients, in the first age range (0 – < 1 year old), 3 protocols were identified: two adult protocol and one children protocol. One of the adult protocol was for thorax, abdomen and pelvis examination. From the 12 patients, 5 performed the adult protocol and 5 performed the children protocol. In the second age range (1 - < 5 years old), 4 protocols were identified: three adult protocols and one children protocol. One of the adult protocols also included thorax, abdomen and pelvis examination. The most applied one was a thorax adult protocol (8 from 20 patients). The third age range (5 - < 10 years old) had one thorax, abdomen and pelvis protocol and one adult protocol, which was performed in 6 from the 8 patients analyzed. In the last age range (10 - < 16 years old), two adult protocols were identified, from which one was thorax, abdomen and pelvis protocol. The thorax adult protocol in this age range was applied in 14 from the 18 patients analyzed.

From these analyses, three protocols were adopted in the experiments with the phantoms: a Head CT protocol, a Thorax protocol and a Thorax, abdomen and pelvis protocol. The criteria adopted to this choice consider that during such procedures, several radiosensitive organs can be directly irradiated. In a typical head CT examination, the primary beam of the CT, depending on the acquisition geometry, can irradiate directly the eye lenses. In a typical thorax CT procedure, the lungs are entirely irradiated and in a thorax, abdomen and pelvis CT,

lungs and liver are target organs. Since they are radiosensitive organs (ICRP, 2000), it is important to evaluate the radiation dose absorbed by these organs during such procedures. In addition, the protocol evaluation showed that adult protocols were applied to many pediatric patients. Therefore, it is also important to evaluate the consequences of applying such protocols in small patients.

### 5.3. ORGAN VOLUMES DETERMINATION FOR ADULT AND PEDIATRIC PHANTOMS

To evaluate organ doses in anthropomorphic phantoms by using the previously described methodology (Section 3.2.3), which is similar to the one proposed by Huda & Sandison (1984) and Golikov & Nikitin (1989), it is necessary to determine the organ mass fraction ( $f_i$ ) inside the slices of the phantoms. For the RANDO phantom, the cited authors determined these organ mass fractions, as it was described in Sections 3.2.3.1 and 4.3.1. Moreover, according to Golikov & Nikitin, the organ volumes are similar to their masses because they are considered a soft-tissue organ. As a consequence, the values of  $f_i$  were approximated to the organ volumes inside each slice and they were adopted to determine the values of  $f_i$  for the lungs and liver of the CIRS ATOM 705 pediatric phantom.

The lung tissue was located inside the slices of the phantoms and the organ volumes inside each slice for these organs were determined with a threshold algorithm (Figure 3.11). Uncertainties due to the choice of the threshold were estimated, since the threshold level was chosen visually. This phantom, however, does not present the localization of the liver. In order to determine this organ localization and its volume per slice, a study conducted by Inkoom et al. (2015) was adopted along with a collaboration of a radiologist from the partner hospital. As presented by Inkoom et al., the liver of this phantom is located inside slices 15-19. Therefore, the distribution of the livers inside these slices was adopted by considering data from 5 pediatric patients. The total volume and the organ volumes fraction ( $f_i$ ) for liver and lungs were presented in Table 4.3 and Table 4.4.

Patients were chosen according to their ages and effective diameter to best match the dimensions of the phantom. However, some issues with this methodology need to be highlighted. The total volumes of the liver range from 525.0 to 744.7 cm<sup>3</sup>. According to ICRP Publication 89 (2002) and ICRU Publication 44 (1989), the expected volume for a 5-year old reference pediatric patient is 540 cm<sup>3</sup>. Such difference might be due to the huge variations among patients from different countries but, moreover, since these patients were performing

abdomen CT, many of them presented some pathology that can cause distortions in their abdominal region. Many patients with these issues were evaluated, but data needed to be discarded. As a consequence of this analysis, the liver fractions are considered as estimates and the high uncertainties in these values are due to the large variation among all patients.

#### 5.4. ORGAN DOSES EVALUATION

Recently, organ doses evaluation has been subject of interest of many investigations. Some of the adopted approaches include Monte Carlo simulations while others consider in phantom, in vivo or post-mortem measurements with several kinds of dosimeters (Griglock et al., 2015; Long et al., 2013; Martins, 2015; Sinclair et al., 2015). Organ doses in the adult and pediatric anthropomorphic phantoms using TLDs and OSLDs for three CT protocols were evaluated in the present study, according to the previously described methodology (Section 3.2.5). Results obtained with the two kinds of dosimeters are in good agreement, showing that both are adequate for the purpose of measuring organ doses.

##### 5.4.1. *Thorax: CIRS ATOM Phantom*

The first protocol studied was the *Thorax for children* protocol using the Philips Brilliance 64 CT scanner dedicated for routine examinations at InRad. Such protocol was commonly applied in children in the age range from 2 to 5 years old.  $CTDI_{vol}$  and DLP displayed by the CT scanner in this protocol were 7 mGy and 196.3 mGy.cm for a scan length of 22 cm. The phantom was irradiated from the middle of slice 8 until the middle of its abdomen, so that thyroid and lungs were irradiated by the primary beam. As a result, doses obtained for both organs are comparable: for the thyroid, doses were estimated as  $6.79 \pm 0.08$  mGy with the TLDs and  $7.26 \pm 0.19$  mGy for the OSLDs. For the lungs, doses were estimated as  $6.1 \pm 0.3$  mGy with the TLDs and  $6.0 \pm 0.3$  mGy with the OSLDs. These results highlight the importance of choosing both the adequate scan length and the right position of the patient on the couch, otherwise the thyroid can receive as much radiation dose as the lungs.

In the study conducted by Fujii et al. (2015), the authors performed organ doses measurements in an adult anthropomorphic phantom (Kyoto Kagaku, Japan) and in a 1-year old pediatric phantom (ATOM Model 704-C, CIRS, Inc., USA). Measurements were performed with silver-activated phosphor glass dosimeter and compared with results simulated by ImpactMC (CT Imaging GmbH, Germany). Results reported by these authors were also comparable for lungs and thyroid for the 1-year old pediatric patient, indicating that probably

the thyroid was also within the scanning area. For the lungs, the dose estimated was 11.2 mGy and for the thyroid it was 11.0 mGy. The effective mAs used in the present study was 59.7 mAs<sub>eff</sub> and in the cited work it was 47 mAs<sub>eff</sub>. Considering the dosimetric quantity  $\frac{\text{organ dose}}{\text{mAs}_{\text{eff}}}$  reported in Table 4.5, in the Thorax CT protocol the thyroid dose per effective mAs was 0.114 mGy/mAs<sub>eff</sub> measured with the TLDs and 0.122 mGy/mAs<sub>eff</sub> measured with the OSLDs for the 5-year old phantom. The lung dose per effective mAs was 0.102 mGy/ mAs<sub>eff</sub> measured with the TLDs and 0.100 mGy/ mAs<sub>eff</sub> measured with the OSLDs. For the 1-year old pediatric phantom studied by Fujii et al., the thyroid dose per effective mAs was 0.234 mGy/mAs<sub>eff</sub> and the lung dose per effective mAs was 0.238 mGy/ mAs<sub>eff</sub>. In a 1-year old pediatric phantom, these organs weights approximately half of the 5-year old pediatric phantom organs, which is consistent with the values obtained for these organ doses per effective mAs.

#### 5.4.2. Thorax, abdomen and pelvis: CIRS ATOM Phantom and RANDO Phantom

The second protocol applied was the *Thorax, Abdomen and pelvis (3 phases)* using the Philips Brilliance 64 CT scanner dedicated for routine examinations at InRad. This protocol was applied to both pediatric and adult phantoms. For the pediatric phantom, CTDI<sub>vol</sub> and DLP displayed by the CT scanner were 2.6 mGy and 138 mGy.cm for a scan length of 46.5 cm. Thyroid, lungs and liver were irradiated. Because of the small size of the thyroid compared to the others, this organ absorbed dose is greater than the other organs absorbed doses. With TLDs, dose obtained for this organ was 17.43±0.07 mGy and for OSLDs, dose obtained was 15.74±0.28 mGy. For the lungs, dose obtained with the TLDs was 13.0±0.6 mGy and for OSLDs, dose obtained was 12.6±0.5 mGy. For the liver, doses were 13.0±0.5 mGy with TLDs and 13.5±0.6 mGy with OSLDs. As previously described (Section 3.2.4), a clinical examination is not performed with 3 contrast phases and TCM is always applied for both adult and pediatric patients. Some situations include a 2 or 3-contrast phase examinations of the abdomen region only. For the adult phantom, lungs and liver were directly irradiated and dose to the thyroid was due to the scattered radiation. CTDI<sub>vol</sub> and DLP displayed by the CT scanner were 6.5 mGy and 494.5 mGy.cm for a scan length of 68.0 cm. With TLDs, dose obtained for the thyroid was 11.7±0.5 mGy and for OSLDs, dose obtained was 12.1±0.3 mGy. For the lungs, dose obtained with the TLDs was 24.11±0.11 mGy and for OSLDs, dose obtained was 24.33±0.15 mGy. For the liver, doses were 26.86±0.18 mGy with TLDs and 26.26±0.21 mGy with OSLDs. These

values also correspond to doses obtained with 3 phases of examination with the same parameters.

Results obtained for both phantoms with the same irradiation protocol indicate that doses to thyroid are even higher than doses to the other organs when it is directly irradiated. For the RANDO phantom, this organ dose was due to the scattered radiation and is about the half of the value obtained for lungs and liver. In addition, when comparing the normalized dosimetric quantities for both phantoms, such as  $\frac{\text{organ dose}}{mAs_{eff}}$  for lungs and liver, it is possible to note that this quantity is higher for the pediatric phantom, which is much smaller in size and weight than the adult phantom. While the lungs of the pediatric phantom absorbed about 0.38 mGy/mAs<sub>eff</sub>, the adult phantom absorbed approximately 0.28 mGy/mAs<sub>eff</sub>. Similarly, while the liver of the pediatric phantom absorbed about 0.40 mGy/mAs<sub>eff</sub>, the adult phantom absorbed approximately 0.30 mGy/mAs<sub>eff</sub>. These results highlight the importance of choosing a pediatric-specific CT scanning protocol in order to adapt the parameters according to patient anatomy.

In the investigation performed by Griglock et al. (Griglock et al., 2015), organ doses were directly measured in CT procedures by placing Landauer OSL nanoDots inside the organs of post-mortem subjects. The authors studied five protocols in three cadavers with different body mass indexes (BMIs). The subjects were irradiated with an Aquilion ONE (Toshiba Medical Systems, Tustin, Calif) and tube current modulation was applied in all protocols. Similar trend reported by these authors were also found in the present study. Organs that were completely irradiated during a given examination received a similar dose, for instance, which happened in this study for liver and lungs of both adult and pediatric phantoms. The thyroid, however, irradiated in the pediatric phantom in the present study, presented even higher dose due to its small size when compared to the lungs and the liver. In addition, the highest absorbed doses were observed for the cadaver with the smallest BMI, but, as an unexpected result, the lowest absorbed doses were observed for the cadaver with the intermediate BMI. The authors state that it happened for a number of reasons, which include internal organ shielding. The internal organ shielding, caused by adipose and soft tissues is the reason why organs of smaller patients absorb more energy (Griglock et al., 2015).

#### 5.4.3. *Head/Head and Neck: CIRS ATOM Phantom and RANDO Phantom*

A *Head 3D* protocol was applied to both the adult and pediatric phantom in the last set of measurements to investigate doses to the eye lenses and to the thyroid. In a similar approach

as the adopted in the thorax, abdomen and pelvis protocol, the thyroid was entirely irradiated in the pediatric phantom and, in the adult phantom, dose to this organ was due to the scattered radiation. For both phantoms, acquisition parameters were the same, except for scan length and DLP. For the pediatric phantom,  $CTDI_{vol}$  and DLP displayed by the CT scanner were 38.7 mGy and 1103.0 mGy.cm for a scan length of 23.1 cm, covering head and neck of the phantom so that thyroid and eye lenses were irradiated. With TLDs, dose obtained for the thyroid was  $40.65 \pm 0.76$  mGy and for OSLDs, dose obtained was  $43.04 \pm 0.65$  mGy. Such values were even greater than the ones obtained for the eye lenses, which were  $28.70 \pm 3.00$  mGy with the TLDs and  $32.69 \pm 0.28$  mGy with OSLDs. For the adult phantom, on the other hand,  $CTDI_{vol}$  and DLP displayed by the CT scanner were 38.7 mGy and 860.0 mGy.cm for a scan length of 18.0 cm, covering the head of the phantom so that only the eye lenses were irradiated and the thyroid was outside the scanning area. With such configuration, dose obtained for the thyroid was  $5.32 \pm 0.15$  mGy with TLDs and  $6.80 \pm 0.20$  mGy with OSLDs. For the eye lenses, absorbed doses were  $26.1 \pm 1.4$  mGy measured with the TLDs and  $26.39 \pm 0.91$  mGy measured with OSLDs.

From the examinations performed at InRad and analyzed in the present study, pediatric patients performing head and neck CT was a common issue. Results reported in the present study show that doses are even higher for this organ than for the eye lenses in such examination. In addition, in comparison with the results obtained with the adult phantom, in which thyroid doses were due to scattered radiation, thyroid absorbed doses showed a very large increase.

Absorbed doses to the eye lenses is a subject of concern among the medical physicists community because of the high radiosensitivity of this organ. According to the International Commission on Radiological Protection Publication number 118 (ICRP, 2012), for instance, a study performed with rats showed that a radiation dose of 0.1 Gy is cataractogenic within one-third of the life span. This study is relevant because the rat radiation cataract model is similar to the human lens opacification. Recently, the investigation conducted by Ciarmatori (2016), for instance, aimed to assess the effect of a bismuth shielding system applied to this organ and its effect on image quality, since a head CT scan can expose it to an unnecessary radiation, even when the region of interest is far from the eyes. This study was performed by establishing a reference set up without shielding and dose reduction was assessed by placing TLD on the eye lenses of an anthropomorphic phantom. The authors suggest that such system is an alternative to implement in Head CT where the region of interest is far from the eyes, since it demonstrated up to 29% of dose reduction with no significant introduction of artifacts in images.

#### 5.4.4. Comparative evaluation between measured and simulated organ doses

Monte Carlo simulations were adopted to be compared with the results of the experimental methodology proposed in the present study. Such approach has been proved to be a reliable tool to estimate organ doses, since a variety of voxelized phantoms and representative CT scanners can be implemented (Martins, 2015). In the present work, protocol parameters previously described were simulated in the software NCICT (Lee et al., 2015) and CalDose (Kramer, Khoury, & Vieira, 2008). Results are presented along with the percent difference between experimental ( $D_{exp}$ ) and simulated values ( $D_{sim}$ ) for each kind of dosimeter per evaluated organ, which is determined as follows:

$$\Delta = \left( \frac{D_{simulated} - D_{experimental}}{D_{simulated}} \right) \times 100\% \quad (5.1)$$

NCICT combined the ICRP 89 reference pediatric and adult phantoms with several CT scanner models (Lee et al., 2015; Lee et al., 2009). NCICT presents a graphical user interface so that the user introduces the scan parameters specific to each examination (Lee et al., 2015) (Figure 5.1a). CalDose\_XCT developed adult phantoms by analyzing data from Caucasian male and female adult populations, autopsy data for organ masses and medical investigations (Cassola, Milian, Kramer, de Oliveira Lira, & Khoury, 2011). A set of 18 anthropometric adult phantoms were developed and the 176 cm tall and 79.6 kg adult male was used in the simulations performed in the present study, since this phantom has the same organ masses as the ICRP 89 (2002) reference man<sup>k</sup>. According to the authors, the 5-year old phantom was developed by modeling anatomical information from atlases and books. Organ and tissue masses match data proposed by the ICRP 89 (2002) for the reference kids (de Melo Lima et al., 2011). CalDose\_XCT is an online software with a graphic user interface (Figure 5.1b).

---

<sup>k</sup> Standing adult human phantoms based on 10th, 50th and 90th mass and height percentiles of male and female Caucasian populations: supplementary data (Cassola et al., 2011). Available at: <http://iopscience.iop.org/article/10.1088/0031-9155/56/13/002/data>

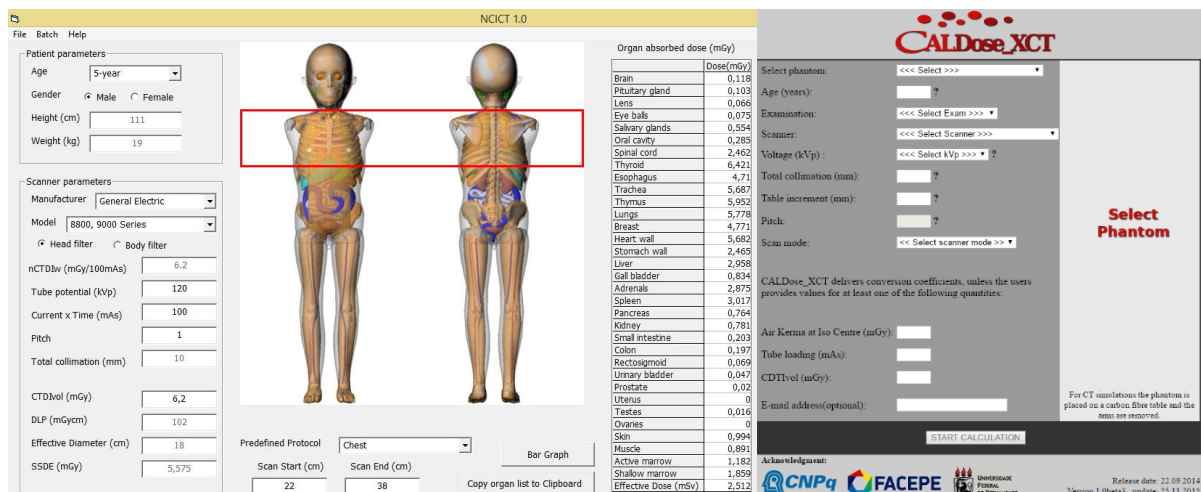


Figure 5.1 – a) NCICT (Lee et al., 2015) and b) Caldose\_XCT (Kramer et al., 2008) used to simulate organ absorbed doses and compare with experimental results.

Comparative results for all protocols adopted in the present study are discussed below.

### 1. Thorax for children

Experimental results are in good agreement with the simulations performed with the software NCICT (Table 5.1). The highest percent differences between experimental measurements with OSLDs and NCICT is 14%, obtained with OSLDs for the lungs. When comparing data with simulations performed by CalDose, percent differences are a little higher (22 and 24% for the lungs). A difference of 171% was found for the thyroid, which did not happen with simulations performed with the NCICT software. This is a consequence of the choice of the scan length of irradiation, as previously described (Section 5.4.1). With NCICT it is possible to choose the same scan length used in the experimental acquisition, while in CalDose\_XCT this scan length is determined by the software. As a consequence, it was possible to simulate an irradiation starting in the neck of the phantom, the same as performed with the physical phantom and, therefore, percent difference between the measured and simulated thyroid doses is 10% for TLD and 4% for OSLD. This protocol measurement performed with CalDose\_XCT, however, started in the beginning of the lungs (R. Kramer, personal communication, April 7<sup>th</sup>, 2017) and, as a consequence, thyroid dose was only due to scattered radiation. The increase in thyroid dose due to a direct irradiation highlights the importance of properly positioning and aligning patient on the couch, as previously discussed (Sections 5.4.1-5.4.3).

Table 5.1 - Absorbed doses (mGy) calculated for both TLD and OSLD and simulated values obtained with NCICT and CalDose for the Thorax for children protocol. Percent deviation ( $\Delta$ ) values between experimental and simulated values for the CIRS ATOM phantom are also presented.

CIRS ATOM 705								
Organ	Absorbed dose (mGy)				$\Delta$ (NCICT)		$\Delta$ (CalDose)	
	TLD	OSLD	NCICT	CalDose	TLD	OSL	TLD	OSL
Lung	6.10±0.30	6.00±0.30	6.97	7.85	12%	14%	22%	24%
Thyroid	6.79±0.08	7.26±0.19	7.54	2.68	10%	4%	<u>-154%</u>	<u>-171%</u>

## 2. Thorax, abdomen and pelvis (3 phases)

Results obtained with this protocol are similar to results presented for the *Thorax for Children* protocol. Experimental results are in good agreement with the simulations performed with the software NCICT, with the highest percent differences between experimental measurements and NCICT of 13% for the thyroid and liver of the CIRS phantom and of 22% for the thyroid of the RANDO phantom (Table 5.2). When comparing data with simulations performed by CalDose, the same issue is reported, due to the scan length of the simulation. The highest percent difference among directly irradiated organs is 14% for the liver of the CIRS phantom and 23% for the lungs of the RANDO phantom. A difference found for the thyroid of the CIRS phantom appears because this organ was directly irradiated and caused a higher dose. For the RANDO phantom, measured thyroid doses were lower than simulated doses with CalDose\_XCT, which is also a consequence of the choice of the scan length of irradiation. In this case, experimental measurement started a few centimeters below the simulation.

Table 5.2 - Absorbed doses (mGy) calculated for both TLD and OSLD and software NCICT and CalDose for the Thorax, abdomen and pelvis protocol. Percent deviation ( $\Delta$ ) values between experimental and simulated values for the CIRS ATOM phantom and for the RANDO phantom are also presented.

<b>CIRS ATOM 705</b>								
<b>Organ</b>	<b>Absorbed dose (mGy)</b>				<b><math>\Delta</math> (NCICT)</b>		<b><math>\Delta</math> (CalDose)</b>	
	<b>TLD</b>	<b>OSLD</b>	<b>NCICT</b>	<b>CalDose</b>	<b>TLD</b>	<b>OSL</b>	<b>TLD</b>	<b>OSL</b>
Lung	13.01±0.55	12.60±0.50	12.13	12.04	-7%	-4%	-8%	-5%
Liver	13.00±0.50	13.50±0.60	11.95	11.84	-9%	-13%	-10%	-14%
Thyroid	17.43±0.07	15.74±0.28	15.41	3.84	-13%	-2%	<u>-354%</u>	<u>-310%</u>

<b>The RANDO Phantom</b>								
<b>Organ</b>	<b>Absorbed dose (mGy)</b>				<b><math>\Delta</math> (NCICT)</b>		<b><math>\Delta</math> (CalDose)</b>	
	<b>TLD</b>	<b>OSLD</b>	<b>NCICT</b>	<b>CalDose</b>	<b>TLD</b>	<b>OSL</b>	<b>TLD</b>	<b>OSL</b>
Lung	24.11±0.11	24.33±0.15	23.09	31.20	-4%	-5%	23%	22%
Liver	26.86±0.18	26.26±0.21	24.60	33.21	-9%	-7%	19%	21%
Thyroid	11.70±0.50	12.13±0.33	14.80	16.62	22%	18%	<u>31%</u>	<u>27%</u>

### 3. Head (3D)

Percent differences between measured and simulated protocols are increased for the eye lenses with this protocol for both NCICT and CalDose (Table 5.3). This could be due to the choice of the scan length and to the positioning of dosimeters on the eye lenses of the phantom. In addition, Caldose\_XCT does not provide thyroid doses for such protocol.

Table 5.3 - Absorbed doses (mGy) calculated for both TLD and OSLD and software NCICT and CalDose for the Head and Head and Neck protocol. Percent deviation ( $\Delta$ ) values between experimental and simulated values for the CIRS ATOM phantom and for the RANDO phantom are also presented.

<b>CIRS ATOM 705</b>								
<b>Organ</b>	<b>Absorbed dose (mGy)</b>				<b><math>\Delta</math> (NCICT)</b>		<b><math>\Delta</math> (CalDose)</b>	
	<b>TLD</b>	<b>OSLD</b>	<b>NCICT</b>	<b>CalDose</b>	<b>TLD</b>	<b>OSL</b>	<b>TLD</b>	<b>OSL</b>
Thyroid	40.65±0.76	43.04±0.65	42.11	-	3%	-2%	-	-
Eye lenses	28.70±3.00	32.69±0.28	37.87	11.42	24%	14%	<u>-151%</u>	<u>-186%</u>

<b>The RANDO Phantom</b>								
<b>Organ</b>	<b>Absorbed dose (mGy)</b>				<b><math>\Delta</math> (NCICT)</b>		<b><math>\Delta</math> (CalDose)</b>	
	<b>TLD</b>	<b>OSLD</b>	<b>NCICT</b>	<b>CalDose</b>	<b>TLD</b>	<b>OSL</b>	<b>TLD</b>	<b>OSL</b>
Thyroid	5.32±0.15	6.80±0.20	5.80	-	-8%	-17%	-	-
Eye lenses	26.10±1.40	26.39±0.91	33.1	18.82	21%	20%	<u>37%</u>	<u>39%</u>

Generally, experimental results are in good agreement with simulated values, with the main differences occurring for simulations performed with the CalDose software and caused by the choice of the experimental scan length, which was done in order to investigate the doses to the thyroid when this organ is directly irradiated. Other aspects can be related to anatomical differences between computational and physical phantoms. Despite such differences, the experimental methodology presented in the present study proved to be adequate for such analysis.

Monte Carlo simulations to estimate organ absorbed doses has become a common subject. Fujii et al. (2015), for instance, compared the experimental results obtained with silver-activated phosphor glass dosimeter with results simulated by ImpactMC (CT Imaging GmbH, Germany) for an adult physical phantom and a 1-year old physical phantom. Percent differences reported by these authors are within  $\pm 13\%$  for organs that were within the scan range and the authors considered measured and simulated results to be in good agreement. In the study conducted by Dabin et al. (2016), the authors performed organ dose measurements in a 5-year old anthropomorphic phantom for five different CT scanners from four manufacturers. The authors measured absorbed doses to 22 organs by directly applying TLDs inside the organs of the phantom for head-to-torso acquisitions. These values were compared with the values calculated with the software NCICT. Two main results of this study can be highlighted. First, for most organs the difference between measured and simulated absorbed organ doses was within  $\pm 20\%$ , which are in good agreement to the simulation performed with the software and is very similar to results found in this study. In addition, the authors developed a voxelized phantom based on the CIRS ATOM phantom used for the experimental measurements and performed the simulations using this voxelized phantom. Percent differences in this case was within  $\pm 10.4\%$  interval, which was a great improvement. This result shows that most of the differences obtained with simulations and experiments can be associated with differences in phantom anatomies.

## 5.5. COMPARISON OF PATIENT DATA WITH INTERNATIONAL DRL

DRLs in CT have been introduced in order to follow-up patient doses, to discover bad practices, and to promote good practices and, as a consequence, to reduce patient doses. In Computed Tomography procedures, radiation dose delivered to pediatric patients is especially a subject of concern because of their higher sensitivity to radiation and longer remaining life expectancy. Despite the concern about pediatric radiation dose, large-scale national or multi-

national surveys of patient doses in pediatric CT are limited and most of them did not established DRLs. Besides, most of them were performed by collecting data from developed countries with well-established practices in patient dosimetry, radiation protection and medical physicists support (European Society of Radiology, 2015; Vassileva et al., 2015).

DRLs are a useful tool to verify whether radiation dose delivered to patients are in accordance with the ALARA principle. Since there is no pediatric DRL established in Brazil, CTDI and DLP obtained from patient data collected were analyzed and compared with three important DRL surveys in the present study.

In the survey conducted by Vassileva et al. (2015), data from 32 countries were collected, with a total of 6115 patient data collected in four age groups (< 1 y, > 1 - 5 y, > 5 - 10 y and >10 - 15 y). Statistical analysis was performed and international DRLs were proposed from these data by rounding the 75<sup>th</sup> percentile values of distribution of median values from all CT equipment. DRLs were established for DLP by considering the whole exam (single phase or multi-phase) and, in multi-phases examination, DRLs for  $CTDI_{vol}$  were established by calculating the mean  $CTDI_{vol}$  value. For Head CT, DRLs are based on a 16-cm phantom and for Thorax CT they are based on a 32-cm phantom. This study was proposed by the authors as a guide for optimization, especially for developing countries.

DRLs proposed by the European Society of Radiology (2015) (EDRLs) were established by considering national DRL (NDRL) existing within Europe. They were based on the median (50<sup>th</sup> percentile) value of the distribution of the NDRLs, which represent the 75<sup>th</sup> percentile. This document also works as a guide for optimization, although the authors recommend that NDRLs are established for each country based on an adequate national survey. In addition, DRLs in this document were established by considering one-phase examinations only. For Head CT, DRLs are based on a 16-cm phantom and for body CT they are based on a 32-cm phantom.

NDRLs were first proposed by the UK in 2003 and provided reference values for several examinations, for both adult and pediatric patients. In these surveys, DRLs represent the 75<sup>th</sup> percentile values. The review proposed in 2005 served to update the first data collection and to review previously published values. DRLs were established for DLP by considering all phases reported for each standard protocol and  $CTDI_{vol}$  per sequence (Shrimpton et al., 2005). DRLs for Thorax CT are established in this survey relative to a 32-cm phantom. The latest

review was performed in 2011<sup>1</sup>. This report presents NDRLs for adults and children based on the 75<sup>th</sup> percentile values and DRL values for Head CT were extracted from this survey. According to the authors, there was not enough Thorax CT data to include in the 2011 review (Shrimpton et al., 2014).

The comparison of median CTDI<sub>vol</sub> and DLP values from patient data collected at InRad are presented in Section 4.5. Considering Head CT, the median value of DLP calculated exceeds all DRLs for the first age range (0 – 1 y), the International and European DRLs for the second age range (1 – 5 y) and the European DRLs in the third age range (5 – 10 y). In terms of CTDI<sub>vol</sub> the median value only exceeds the European DRL for the second age range (Figure 4.11 and Table 4.8). Considering Thorax CT, the median value of DLP calculated only exceeds the European DRLs for three age groups: 0 – 1 y, 5 < 10 y and 10 < 16 y. In terms of CTDI<sub>vol</sub> the median value only exceeds the European DRLs for the first age group (0 – 1 y) (Figure 4.12 and Table 4.9).

However, care should be taken when comparing local data with international values of DRL. First, some of examinations collected at InRad included a two-phase examination, which was only considered in the international survey conducted by Vassileva (2015). In addition, age grouping in the present study was the same as the one proposed by Vassileva, but it was different for the two other surveys: in the UK survey, age groups were considered up until 10 years old and in the European survey, a weight-based grouping was performed. The authors proposed an approximate corresponding age, which is a little different from the present study. In that work, the authors recommend that weight should be used as a parameter for patient grouping in all body examinations and age should be used in head examinations (European Society of Radiology, 2015). Additionally, this document state that the median value of a quantity should be determined for at least 10 patients. For the third age range in Thorax CT (5 – 10 y), median values were calculated considering only 6 patients. Finally, the large variation of patient size and weight between various countries must be taken into account. As a consequence, international DRLs should only be used as guides for optimization until appropriate national surveys are conducted (European Society of Radiology, 2015).

Recently, there are several publications with recommendations for children-specific protocols and they include guidelines for optimization of many CT scanner parameters (Heier

---

<sup>1</sup> Available at: <<https://www.gov.uk/government/publications/diagnostic-radiology-national-diagnostic-reference-levels-ndrls/national-diagnostic-reference-levels-ndrls>>.

& Pinto, 2017; Strauss, 2014a; Strauss et al., 2010). Such documents must be considered and taken into account by the clinical staff when performing pediatric CT examinations.

## 6. CONCLUSIONS

The present study employed an experimental approach to evaluate organ doses in pediatric and adult anthropomorphic phantoms by using thermoluminescent and optically stimulated luminescent dosimeters. Several analyses were performed in order to establish the best way to achieve the main results in this investigation and the methodology proved to be efficient.

The first step was to investigate the characteristics of the Al<sub>2</sub>O<sub>3</sub>:C Luxel OSLD tape from Landauer, Inc. to measure organ doses due to CT procedures. Various tests were performed and dosimeters presented homogeneity, linearity with the incident air kerma, reproducibility, reusability and an energy-dependent response to distinct effective energies. In addition, normalization of the OSL responses to their responses beta radiation proved to be efficient in decreasing uncertainties related to differences in dosimeters shape, size and uniformity caused by the manual processing of fractionating the tape and, also, by non-stability of the reader. Some advantages of the OSL technique over the TL technique found by other authors were also identified in the present study (Bøtter-Jensen et al., 2003; uz Zaman, Fatima, Naqvi, Parveen, & Sajjad, 2016; Yoshimura & Yukihiro, 2006). Since the readout of the TL materials is a thermal process, it demands a reliable and reproducible heating system. Additionally, the high sensitivity of the OSL allows multiple reading while maintaining the precision.

As a second step, pediatric patient data were collected and evaluated from two CT scanners of the Institute of Radiology of the School of Medicine of the University of São Paulo. Data collected from RIS/PACS were useful to identify non-adequate practices by comparing CTDI<sub>vol</sub> and DLP with international DRLs. Some issues were found in this data collection, such as the fact that some protocols exceeded DRLs and the absence of dose report. Such issues indicate the need of implementing tools to optimize these procedures.

The methodology applied to acquire the volume fractions of the organs of the CIRS ATOM phantom proved to be efficient, but it should be done carefully and treated as an estimate, since one has to deal with the fact that patients subjected to CT examinations may have some pathology in the anatomy of interest. Despite the differences found in the volumes of the five patients analyzed, liver doses calculated were in a very good agreement with results found with two different Monte Carlo simulations.

Organ doses measured with the described methodology proved to be successful. Organ doses found with TLD and OSLD were in good agreement with published studies and Monte Carlo simulations, with main differences related to the scan length of the acquisition and the anatomy of the voxelized phantoms and no significant differences among dosimeters were found. Organ doses results also draw attention to the importance of properly positioning and aligning patients in the couch before starting the examination, otherwise doses can increase more than a 100%.

Finally, some examples and recommendations for future investigations are presented.

- Evaluation of other organ doses, such as kidneys, stomach, spleen, should be considered according to their radiosensitivity and to their irradiation due to routine protocols.
- Analysis of CT protocols for different anatomical regions and applying different types of Tube Current Modulation.
- Assessment of organ doses due to CT protocols especially developed for pediatric patients, according to Image Gently (2014) and Latin Safe (2015) guidelines.
- Evaluation of tools to optimize pediatric protocols, especially based on pediatric data collected in the present study.

As previously discussed, organ doses evaluation is an important step to quantify the radiation doses absorbed by patients due to clinical procedures, since the established doses indexes do not take into account patient size and anatomy. Two important tests were performed in the present study representing one step towards the optimization: the comparison of data from a representative group of patient with international DRLs can identify non-adequate practices and the evaluation of organ doses based on clinical protocols provides reliable information to understand the consequences of a given procedure to a clinical patient.

## REFERENCES

- AAPM. (2008). The Measurement, Reporting, and Management of Radiation Dose in CT. AAPM Task Group 23 (AAPM Report 96). *College Park, MD: American Association of Physicists in Medicine.*
- AAPM. (2010). Comprehensive methodology for the evaluation of radiation dose in x-ray computed tomography. AAPM Task Group 111 (AAPM Report 111). *College Park, MD: American Association of Physicists in Medicine.*
- AAPM. (2011a). AAPM CT lexicon (version 1.3). *College Park, MD: American Association of Physicists in Medicine.*
- AAPM. (2011b). Size-specific dose estimates (SSDE) in pediatric and adult body CT examinations. AAPM Task Group 204 (AAPM Report 204). *College Park, MD: American Association of Physicists in Medicine.*
- Aitken, M. J. (1998). *Introduction to optical dating: the dating of Quaternary sediments by the use of photon-stimulated luminescence*: Clarendon Press.
- Akselrod, M. S., Bøtter-Jensen, L., & McKeever, S. W. S. (2006). Optically stimulated luminescence and its use in medical dosimetry. *Radiation Measurements, 41*, S78-S99. doi:10.1016/j.radmeas.2007.01.004
- Akselrod, M. S., Kortov, V. S., Kravetsky, D. J., & Gotlib, V. I. (1990). Highly Sensitive Thermoluminescent Anion-Defect  $\alpha$ -Al<sub>2</sub>O<sub>3</sub>:C Single Crystal Detectors. *Radiation Protection Dosimetry, 33*(1-4), 119-122. doi:10.1093/oxfordjournals.rpd.a080771
- Al-Senan, R. M., & Hatab, M. R. (2011). Characteristics of an OSLD in the diagnostic energy range. *Medical physics, 38*(7), 4396-4405. doi:10.1118/1.3602456
- Al-Senan, R. M., Mueller, D. L., & Hatab, M. R. (2012). Estimating thyroid dose in pediatric CT exams from surface dose measurement. *Physics in medicine and biology, 57*(13), 4211. doi:10.1088/0031-9155/57/13/4211
- Amis, E. S. (2011). CT Radiation Dose: Trending in the Right Direction. *Radiology, 261*(1), 5-8. doi:10.1148/radiol.11111319
- Araújo, E. C. A. (2008). *Estudo e aplicação do algoritmo FDK para a reconstrução de imagens tomográficas multi-cortes*. (Master's dissertation), Universidade de São Paulo, São Paulo, SP, Brazil. Retrieved from <http://www.teses.usp.br/teses/disponiveis/43/43134/tde-10032009-132445/pt-br.php>
- Archer, B. R., Glaze, S., North, L. B., & Bushong, S. C. (1977). Dosimeter placement in the Rando phantom. *Medical physics, 4*(4), 315-318. doi:10.1118/1.594320
- Boone, J. M. (2007). The trouble with CTDI<sub>100</sub>. *Medical Physics, 34*(4), 1364-1371. doi:10.1118/1.2713240
- Bos, A. J. J. (2001). High sensitivity thermoluminescence dosimetry. *Nuclear Instruments and Methods in Physics Research Section B: Beam Interactions with Materials and Atoms, 184*(1-2), 3-28. doi:10.1016/S0168-583X(01)00717-0
- Bos, A. J. J. (2006). Theory of thermoluminescence. *Radiation measurements, 41*, S45-S56. doi:10.1016/j.radmeas.2007.01.003
- Brenner, D. J., & Hall, E. J. (2007). Computed Tomography - An Increasing Source of Radiation Exposure. *New England Journal of Medicine, 357*(22), 2277-2284. doi:10.1056/NEJMra072149
- Bunge, R. E., & Herman, C. L. (1987). Usage of diagnostic imaging procedures: a nationwide hospital study. *Radiology, 163*(2), 569-573. doi:10.1148/radiology.163.2.3550886

- Bushberg, J. T., Seibert, J. A., Leidholdt Jr, E. M., & Boone, J. M. (2011). *The Essential Physics of Medical Imaging* (3<sup>rd</sup> ed.): Lippincott Williams & Wilkins.
- Bushong, S. C. (2013). *Radiologic Science for Technologists: Physics, Biology, and Protection*: Elsevier Health Sciences.
- Buzug, T. M. (2008). *Computed Tomography: From Photon Statistics to Modern Cone-Beam CT*: Springer Science & Business Media.
- Bøtter-Jensen, L., McKeever, S. W. S., & Wintle, A. G. (2003). *Optically stimulated luminescence dosimetry*: Elsevier.
- Cassola, V. F., Milian, F. M., Kramer, R., de Oliveira Lira, C. A. B., & Khoury, H. J. (2011). Standing adult human phantoms based on 10th, 50th and 90th mass and height percentiles of male and female Caucasian populations. *Physics in medicine and biology*, 56(13), 3749. doi:10.1088/0031-9155/56/13/002
- Chambers, J. M. (1983). *Graphical methods for data analysis*.
- Ciarmatori, A., Nocetti, L., Mistretta, G., Zambelli, G., & Costi, T. (2016). Reducing absorbed dose to eye lenses in head CT examinations: the effect of bismuth shielding. *Australasian Physical & Engineering Sciences in Medicine*, 39(2), 583-589. doi:10.1007/s13246-016-0445-y
- CIRS. (2013). The ATOM Dosimetry Verification Phantoms Brochure (Computerized Imaging Reference Systems, Inc.). Retrieved from [http://www.cirsinc.com/file/Products/701\\_706/701%20706%20ATOM%20PB%20110615.pdf](http://www.cirsinc.com/file/Products/701_706/701%20706%20ATOM%20PB%20110615.pdf)
- Costa, P. R. (2014). Computer Tomography Phantom Applications. In *The Phantoms of Medical and Health Physics* (pp. 123-142): Springer.
- Costa, P. R., & Araújo, E. C. A. (2010). Aplicação do algoritmo FDK para a reconstrução de imagens tomográficas multicortes. *Revista Brasileira de Engenharia Biomédica*, 26(2), 105-120. doi:10.4322/rbeb.2012.084
- Costa, P. R., Yoshimura, E. M., Nersissian, D. Y., & Melo, C. S. (2016). Correlation between effective dose and radiological risk: general concepts. *Radiologia Brasileira*, 49(3), 176-181. doi:10.1590/0100-3984.2014.0097
- Dabin, J., Mencarelli, A., McMillan, D., Romanyukha, A., Struelens, L., & Lee, C. (2016). Validation of calculation algorithms for organ doses in CT by measurements on a 5 year old paediatric phantom. *Physics in medicine and biology*, 61(11), 4168-4182. doi:10.1088/0031-9155/61/11/4168
- Daniels, F., Boyd, C. A., & Saunders, D. F. (1953). Thermoluminescence as a Research Tool. *Science*, 117(3040), 343-349. doi:10.1126/science.117.3040.343
- de Melo Lima, V. J., Cassola, V. F., Kramer, R., de Oliveira Lira, C. A. B., Khoury, H. J., & Vieira, J. W. (2011). Development of 5-and 10-year-old pediatric phantoms based on polygon mesh surfaces. *Medical physics*, 38(8), 4723-4736. doi:10.1118/1.3615623
- Dehm, C., & Reinsberger, H. (2012). STRATON X-ray tube. Retrieved from [https://health.siemens.com/ct\\_applications/somatomsessions/index.php/straton-x-ray-tube/](https://health.siemens.com/ct_applications/somatomsessions/index.php/straton-x-ray-tube/)
- DeMaio, D. N. (2010). *Mosby's Exam Review for Computed Tomography*: Elsevier Health Sciences.
- Dodge, C. T., Tamm, E. P., Cody, D. D., Liu, X., Jensen, C. T., Wei, W., . . . Rong, X. J. (2016). Performance evaluation of iterative reconstruction algorithms for achieving CT radiation dose reduction — a phantom study. *Journal of Applied Clinical Medical Physics*, 17(2), 511-531. doi:10.1120/jacmp.v17i2.5709

- DTU Nutech. (2015). Guide to the Risø TL/OSL Reader. Retrieved from <http://www.usu.edu/geo/luminlab/Reader.pdf>
- European Society of Radiology. (2015). European Guidelines on DRLs for Paediatric Imaging. Retrieved from <https://www.sirm.org/download/2011>
- Fosbinder, R., & Orth, D. (2011). *Essentials of radiologic science*: Lippincott Williams & Wilkins.
- Franck, C., Vandevoorde, C., Goethals, I., Smeets, P., Achten, E., Verstraete, K., . . . Bacher, K. (2016). The role of Size-Specific Dose Estimate (SSDE) in patient-specific organ dose and cancer risk estimation in paediatric chest and abdominopelvic CT examinations. *European Radiology*, 26(8), 2646-2655. doi:10.1007/s00330-015-4091-7
- Fujii, K., Nomura, K., Muramatsu, Y., Takahashi, K., Obara, S., Akahane, K., & Satake, M. (2015). Evaluation of organ doses in adult and paediatric CT examinations based on Monte Carlo simulations and in-phantom dosimetry. *Radiation protection dosimetry*, 165(1-4), 166-171. doi:10.1093/rpd/ncv074
- Furetta, C. (2008). *Questions and answers on thermoluminescence (TL) and optically stimulated luminescence (OSL)*: World Scientific.
- Furetta, C. (2010). *Handbook of thermoluminescence*: World Scientific.
- Gasparian, P. B. R. (2009). *Methodological developments for application of optically stimulated luminescence (OSL) in medical dosimetry*. (Master's dissertation), Oklahoma State University, Oklahoma, USA. Retrieved from [http://digital.library.okstate.edu/etd/Gasparian\\_okstate\\_0664M\\_10491.pdf](http://digital.library.okstate.edu/etd/Gasparian_okstate_0664M_10491.pdf)
- Gasparian, P. B. R., Vanhavere, F., & Yukihiro, E. G. (2012). Evaluating the influence of experimental conditions on the photon energy response of Al<sub>2</sub>O<sub>3</sub>:C Optically Stimulated Luminescence detectors. *Radiation Measurements*, 47(4), 243-249. doi:10.1016/j.radmeas.2012.01.012
- Gharbi, S., Labidi, S., Mars, M., Chelli, M., & Ladeb, F. (2017). Effective Dose and Size Specific Dose Estimation with and without Tube Current Modulation for Thoracic Computed Tomography Examinations: A Phantom Study. *World Academy of Science, Engineering and Technology, International Journal of Medical, Health, Biomedical, Bioengineering and Pharmaceutical Engineering*, 11(3), 55-59.
- Giansante, L., Sawamura, M. M., Tomal, A., & Costa, P. R. (2016). *Aplicação de Métodos de Segmentação de Imagens para Mapeamento dos Órgãos de um Phantom Antropomórfico Pediátrico*. Paper presented at the Jornada Paulista de Radiologia, São Paulo, SP, Brazil.
- Golikov, V., & Nikitin, V. (1989). Estimation of the mean organ doses and the effective dose equivalent from Rando phantom measurements. *Health physics*, 56(1), 111-115.
- Gonzaga, N., Mourão, A., Magalhães, M., & da Silva, T. (2014). Organ equivalent doses of patients undergoing chest computed tomography: Measurements with TL dosimeters in an anthropomorphic phantom. *Applied Radiation and Isotopes*, 83, 242-244. doi:10.1016/j.apradiso.2013.07.017
- Griglock, T. M., Sinclair, L., Mench, A., Cormack, B., Bidari, S., Rill, L., & Arreola, M. (2015). Determining Organ Doses from CT with Direct Measurements in Postmortem Subjects: Part 1—Methodology and Validation. *Radiology*, 277(2), 463-470. doi:10.1148/radiol.2015140968
- Han, S. C., Kim, K. B., Jung, H., Ji, Y., & Park, S. (2016). Assessment of Diagnostic Multileaf Collimator for Cephalometric Exposure Reduction using Optically Stimulated Luminescent Dosimeters. *Radiation protection dosimetry*, 174(1), 102-108. doi:10.1093/rpd/ncw080
- Heier, L. A., & Pinto, S. N. (2017). Image Gently: Minimizing Radiation Exposure in Children. In *Common Neurosurgical Conditions in the Pediatric Practice* (pp. 279-297): Springer New York.

- Hsieh, J. (2009). *Computed tomography: principles, design, artifacts, and recent advances* (2<sup>nd</sup> ed. Vol. 114): SPIE Press.
- Hubbell, J., & Seltzer, S. (2004). Tables of X-ray mass attenuation coefficients and mass energy-absorption coefficients (version 1.4). *National Institute of Standards and Technology, Gaithersburg, MD, USA*.
- Huda, W., & Sandison, G. A. (1984). Estimation of mean organ doses in diagnostic radiology from Rando phantom measurements. *Health Physics*, 47(3), 463.
- Huntley, D. J., Godfrey-Smith, D. I., & Thewalt, M. L. W. (1985). Optical dating of sediments. *Nature*, 313(5998), 105-107.
- IAEA. (2007). *Dosimetry in Diagnostic Radiology: An International Code of Practice*. Vienna: International Atomic Energy Agency (Technical Report Series No.457).
- IAEA. (2013). Coordinated Research Projects-About Us. Retrieved from <http://cra.iaea.org/cra/about-us.html>
- IAEA. (2014). *Dosimetry in Diagnostic Radiology for Paediatric Patients*. Vienna: International Atomic Energy Agency (IAEA Human Health Series No. 24).
- ICRP. (2000). Managing Patient Dose in Computed Tomography. ICRP Publication 87. *Ann. ICRP*, 30(4).
- ICRP. (2002). Basic Anatomical and Physiological Data for Use in Radiological Protection Reference Values. ICRP Publication 89. *Ann. ICRP*, 32(3-4).
- ICRP. (2007). The 2007 Recommendations of the International Commission on Radiological Protection. ICRP publication 103. *Ann. ICRP*, 37(2-4).
- ICRP. (2010). Conversion coefficients for radiological protection quantities for external radiation exposures. ICRP Publication 116. *Ann. ICRP*, 40(2-5).
- ICRP. (2012). ICRP Statement on Tissue Reactions / Early and Late Effects of Radiation in Normal Tissues and Organs – Threshold Doses for Tissue Reactions in a Radiation Protection Context. ICRP Publication 118. *Ann. ICRP*, 41(1/2).
- ICRU. (1989). *Tissue Substitutes in Radiation Dosimetry and Measurement (ICRU Report No. 44)*: International Commission on Radiation Units and Measurements.
- IEC. (2005). Medical diagnostic X-ray equipment - Radiation conditions for use in the determination of characteristics (1994 Standard IECs No. 61267). *International Electrotechnical Committee*.
- Image Gently. (2014). Image Gently and CT Scans. Retrieved from <http://www.imagegently.org/Procedures/Computed-Tomography>
- IMPACT. (2001). CT Scanner Acceptance Testing. Retrieved from <http://www.impactscan.org/download/acceptancetesting.pdf>
- Inkoom, S., Raissaki, M., Perisinakis, K., Maris, T. G., & Damilakis, J. (2015). Location of radiosensitive organs inside pediatric anthropomorphic phantoms: Data required for dosimetry. *Physica Medica*, 31(8), 882-888. doi:10.1016/j.ejmp.2015.06.005
- International Marketing Ventures. (2015). 2015 CT Benchmark Report. Retrieved from [http://www.imvinfo.com/user/documents/content\\_documents/receive\\_info/2015\\_12\\_24\\_12\\_16\\_15\\_727\\_IMV\\_CT\\_2015\\_Benchmark.pdf](http://www.imvinfo.com/user/documents/content_documents/receive_info/2015_12_24_12_16_15_727_IMV_CT_2015_Benchmark.pdf)
- Jessen, K. A., Panzer, W., Shrimpton, P. C., Bongartz, G., Geleijns, J., Golding, S., . . . Tosi, G. (2000). EUR 16262: European guidelines on quality criteria for computed tomography. *Luxembourg: Office for Official Publications of the European Communities*.

- Kalender, W. A. (2011). *Computed tomography: fundamentals, system technology, image quality, applications*: John Wiley & Sons.
- Kalender, W. A. (2014). Dose in x-ray computed tomography. *Physics in Medicine and Biology*, 59(3), R129-R150. doi:10.1088/0031-9155/59/3/r129
- Kalra, M. K., Naz, N., Rizzo, S. M. R., & Blake, M. A. (2005). Computed Tomography Radiation Dose Optimization: Scanning Protocols and Clinical Applications of Automatic Exposure Control. *Current Problems in Diagnostic Radiology*, 34(5), 171-181. doi:10.1067/j.cpradiol.2005.06.002
- Karmazyn, B., Ai, H., Klahr, P., Ouyang, F., & Jennings, S. G. (2016). How accurate is size-specific dose estimate in pediatric body CT examinations? *Pediatric radiology*, 46(9), 1234-1240. doi:10.1007/s00247-016-3604-0
- Kramer, R., Khoury, H. J., & Vieira, J. W. (2008). CALDose\_X—a software tool for the assessment of organ and tissue absorbed doses, effective dose and cancer risks in diagnostic radiology. *Physics in medicine and biology*, 53(22), 6437.
- Kumar, P., Bahl, S., Sahare, P. D., Kumar, S., & Singh, M. (2015). Optically stimulated luminescence (OSL) response of Al<sub>2</sub>O<sub>3</sub>:C, BaFCl:Eu and K<sub>2</sub>Ca<sub>2</sub>(SO<sub>4</sub>)<sub>3</sub>:Eu phosphors. *Radiation protection dosimetry*, 167(4), 453-460. doi:10.1093/rpd/ncu371
- Landauer Inc. (2012). InLight® Complete Dosimetry System Solution (Technical Specification). Retrieved from [http://www.landauer.com/uploadedFiles/InLight\\_nanoDot\\_FN.pdf](http://www.landauer.com/uploadedFiles/InLight_nanoDot_FN.pdf)
- Latin Safe. (2015). Latin Safe pediatria. Retrieved from <http://www.latinsafe.org/>
- Lavoie, L., Ghita, M., Brateman, L., & Arreola, M. (2011). Characterization of a commercially-available, optically-stimulated luminescent dosimetry system for use in computed tomography. *Health physics*, 101(3), 299-310. doi:10.1097/HP.0b013e31820f8e0e
- Lee, C., Kim, K. P., Bolch, W. E., Moroz, B. E., & Folio, L. (2015). NCICT: a computational solution to estimate organ doses for pediatric and adult patients undergoing CT scans. *Journal of Radiological Protection*, 35(4), 891-909. doi:10.1088/0952-4746/35/4/891
- Lee, C., Lodwick, D., Hurtado, J., Pafundi, D., Williams, J. L., & Bolch, W. E. (2009). The UF family of reference hybrid phantoms for computational radiation dosimetry. *Physics in medicine and biology*, 55(2), 339-363. doi:10.1088/0031-9155/55/2/002
- Leitz, W., Axelsson, B., & Szendro, G. (1995). Computed Tomography Dose Assessment - A Practical Approach. *Radiation Protection Dosimetry*, 57(1-4), 377-380. doi:10.1093/oxfordjournals.rpd.a082564
- Leng, S., Shiung, M., Duan, X., Yu, L., Zhang, Y., & McCollough, C. H. (2015). Size-specific Dose Estimates for Chest, Abdominal, and Pelvic CT: Effect of Inpatient Variability in Water-equivalent Diameter. *Radiology*, 276(1), 184-190. doi:10.1148/radiol.15142160
- Lewis, M. (2004). CT Dosimetry: ImPACT spreadsheet for calculating organ & effective doses from CT exams. Retrieved from <http://www.impactscan.org/slides/ctdosimetrydenmark/>
- Lira, D., Padole, A., Kalra, M. K., & Singh, S. (2015). Tube potential and CT radiation dose optimization. *American Journal of Roentgenology*, 204(1), W4-W10. doi:10.2214/AJR.14.13281
- Long, D. J., Lee, C., Tien, C., Fisher, R., Hoerner, M. R., Hintenlang, D., & Bolch, W. E. (2013). Monte Carlo simulations of adult and pediatric computed tomography exams: validation studies of organ doses with physical phantoms. *Medical physics*, 40(1). doi:10.1118/1.4771934

- Lopez Gonzales, A. H., Tomal, A., & Costa, P. R. (2015). Evaluation of characteristic-to-total spectrum ratio: Comparison between experimental and a semi-empirical model. *Applied Radiation and Isotopes*, *100*, 27-31. doi:10.1016/j.apradiso.2015.01.011
- Malthez, A. L., Freitas, M. B., Yoshimura, E. M., & Button, V. L. (2014). Experimental photon energy response of different dosimetric materials for a dual detector system combining thermoluminescence and optically stimulated luminescence. *Radiation Measurements*, *71*, 133-138. doi:10.1016/j.radmeas.2014.07.018
- Mansoor, A., Bagci, U., Foster, B., Xu, Z., Papadakis, G. Z., Folio, L. R., . . . Mollura, D. J. (2015). Segmentation and image analysis of abnormal lungs at CT: current approaches, challenges, and future trends. *Radiographics*, *35*(4), 1056-1076. doi:10.1148/rg.2015140232
- Martin, C. J., & Sookpeng, S. (2016). Setting up computed tomography automatic tube current modulation systems. *Journal of Radiological Protection*, *36*(3), R74-R95. doi:10.1088/0952-4746/36/3/r74
- Martins, J. C. (2015). *Lung dose estimates for computed tomography procedures*. (Master's dissertation), Universidade de São Paulo, São Paulo, SP, Brazil. Retrieved from <http://www.teses.usp.br/teses/disponiveis/43/43134/tde-16052016-082136/pt-br.php>
- Martins, J. C., Nersissian, D. Y., & Costa, P. R. (2015). *Lung Dose Estimation for a Total Body Computed Tomography Protocol*. Paper presented at the World Congress on Medical Physics and Biomedical Engineering, June 7-12, 2015, Toronto, Canada.
- Mayo-Smith, W. W., Hara, A. K., Mahesh, M., Sahani, D. V., & Pavlicek, W. (2014). How I Do It: Managing Radiation Dose in CT. *Radiology*, *273*(3), 657-672. doi:10.1148/radiol.14132328
- McCollough, C. H., Leng, S. A., Yu, L. F., Cody, D. D., Boone, J. M., & McNitt-Gray, M. F. (2011). CT Dose Index and Patient Dose: They Are Not the Same Thing. *Radiology*, *259*(2), 311-316. doi:10.1148/radiol.11101800
- McKeever, S. W. S. (1988). *Thermoluminescence of solids* (Vol. 3): Cambridge University Press.
- Ministério da Saúde (Brasil). (2016). DATASUS (TABNET). Retrieved from <http://www2.datasus.gov.br/DATASUS/index.php?area=02>
- Mobit, P., Agyingi, E., & Sandison, G. (2006). Comparison of the energy-response factor of LiF and Al<sub>2</sub>O<sub>3</sub> in radiotherapy beams. *Radiation Protection Dosimetry*, *119*(1-4), 497-499. doi:10.1093/rpd/nci676
- Nascimento, L. d. F., Vanhavere, F., Souza, R., & Verellen, D. (2016). Al<sub>2</sub>O<sub>3</sub>:C Optically Stimulated Luminescence droplets: Characterization and applications in medical beams. *Radiation Measurements*, *94*, 41-48. doi:<http://www.teses.usp.br/teses/disponiveis/43/43134/tde-16052016-082136/pt-br.php>
- NHS England. (2014). NHS Imaging and Radiodiagnostic activity - 2013/14 Release. Retrieved from <https://www.england.nhs.uk/statistics/wp-content/uploads/sites/2/2013/04/KH12-release-2013-14.pdf>
- NIST. (1998). XCOM: Photon Cross Sections Database. Retrieved from <https://www.nist.gov/pml/xcom-photon-cross-sections-database>
- NIST. (2011). NIST x-ray Photoelectron Spectroscopy Database (version 3.5). In: National Institute of Standards and Technology.
- Okuno, E., & Yoshimura, E. M. (2010). *Física das radiações*: Oficina de Textos.
- Perks, C. A., Yahnke, C., & Million, M. (2008). *Medical dosimetry using Optically Stimulated Luminescence dots and microStar readers*. Paper presented at the 12th International Congress of the International Radiation Protection Association.

- Philips. (2004-2017). Philips Brilliance 64 CT Scanner. Retrieved from <http://www.philipsctscanner.com/ct-scanner/philips-brilliance-64-ct-scanner/>
- Ponmalar, R., Manickam, R., Ganesh, K. M., Saminathan, S., Raman, A., & Godson, H. F. (2017). Dosimetric characterization of optically stimulated luminescence dosimeter with therapeutic photon beams for use in clinical radiotherapy measurements [Ahead of print]. *Journal of Cancer Research and Therapeutics*.
- Radcal. (2013). 10x5 Series Ion Chambers - Technical Specifications. Retrieved from [http://perlamar.ie/wp-content/uploads/pdf/radcal/Ion\\_Chambers\\_Misc\\_Meters/Radcal\\_10x5\\_Series\\_Ion\\_Chambers.pdf](http://perlamar.ie/wp-content/uploads/pdf/radcal/Ion_Chambers_Misc_Meters/Radcal_10x5_Series_Ion_Chambers.pdf)
- Radiology Support Devices. (2014). The Alderson Radiation Therapy Phantom. Retrieved from [http://www.rsdphantoms.com/rt\\_art.htm](http://www.rsdphantoms.com/rt_art.htm)
- Radon, J. (1917). On determination of functions by their integral values along certain multiplicities. *Ber. der Sachische Akademie der Wissenschaften Leipzig, (Germany)*, 69, 262-277.
- Rehani, M. M. (2015). Radiation effects and risks: overview and a new risk perception index. *Radiation Protection Dosimetry*, 165(1-4), 7-9. doi:10.1093/rpd/ncv117
- Reina, T. R. (2014). *Avaliação de sistemas de controle automático de exposição em tomografia computadorizada*. (Master's dissertation), Universidade de São Paulo, São Paulo, SP, Brazil.
- Schardt, P., Deuringer, J., Freudenberger, J., Hell, E., Knüpfer, W., Mattern, D., & Schild, M. (2004). New x-ray tube performance in computed tomography by introducing the rotating envelope tube technology. *Medical physics*, 31(9), 2699-2706. doi:10.1118/1.1783552
- Seeram, E. (2015). *Computed tomography: physical principles, clinical applications, and quality control*: Elsevier Health Sciences.
- Shope, T. B., Gagne, R. M., & Johnson, G. C. (1981). A method for describing the doses delivered by transmission x-ray computed tomography. *Medical Physics*, 8(4), 488-495. doi:10.1118/1.594995
- Shrimpton, P. C., Hillier, M. C., Lewis, M. A., & Dunn, M. (2005). *Doses from computed tomography (CT) examinations in the UK-2003 review*: National Radiological Protection Board (NRPB).
- Shrimpton, P. C., Hillier, M. C., Meeson, S., & Golding, S. J. (2014). *Doses from computed tomography (CT) examinations in the UK-2011 review*: Public Health England (PHE).
- Sinclair, L., Griglock, T. M., Mench, A., Lamoureux, R., Cormack, B., Bidari, S., . . . Arreola, M. (2015). Determining Organ Doses from CT with Direct Measurements in Postmortem Subjects: Part 2—Correlations with Patient-specific Parameters. *Radiology*, 277(2), 471-476. doi:10.1148/radiol.2015140971
- Stamm, G., & Nagel, H. D. (2002). CT-Expo - A novel program for dose evaluation in CT. *RoFo: Fortschritte auf dem Gebiete der Rontgenstrahlen und der Nuklearmedizin*, 174(12), 1570-1576. doi:10.1055/s-2002-35937
- Strauss, K. J. (2014a). Developing patient-specific dose protocols for a CT scanner and exam using diagnostic reference levels. *Pediatric Radiology*, 44(3), 479-488. doi:10.1007/s00247-014-3088-8
- Strauss, K. J. (2014b). Dose indices: everybody wants a number. *Pediatric Radiology*, 44(3), 450-459. doi:10.1007/s00247-014-3104-z
- Strauss, K. J., Goske, M. J., Kaste, S. C., Bulas, D., Frush, D. P., Butler, P., . . . Applegate, K. E. (2010). Image gently: ten steps you can take to optimize image quality and lower CT dose for pediatric patients. *American Journal of Roentgenology*, 194(4), 868-873. doi:10.2214/AJR.09.4091

- Söderberg, M., & Gunnarsson, M. (2010). Automatic exposure control in computed tomography—an evaluation of systems from different manufacturers. *Acta Radiologica*, 51(6), 625-634. doi:10.3109/02841851003698206
- The Phantom Laboratory. (2012). RAN 100 and RAN 110 Datasheet Brochure. Retrieved from <http://phantomlab.client-proof.com/products/rando.php>
- Turbell, H. (2001). *Cone-beam reconstruction using filtered backprojection*. (Doctoral thesis), Linköping University Electronic Press, Linköping, Sweden.
- Ulzheimer, S., & Flohr, T. (2009). Multislice CT: current technology and future developments. In *Multislice CT* (pp. 3-23): Springer.
- uz Zaman, M., Fatima, N., Naqvi, M., Parveen, R., & Sajjad, Z. (2016). Radiation dosimetry: from thermoluminescence dosimeter (TLD) to optically stimulated luminescence dosimeter (OSLD). *Pakistan Journal of Radiology*, 21(3), 107-109.
- Vassileva, J., Rehani, M., Kostova-Lefterova, D., Al-Naemi, H. M., Al Suwaidi, J. S., Arandjic, D., . . . Aguilar, J. G. (2015). A study to establish international diagnostic reference levels for paediatric computed tomography. *Radiation protection dosimetry*, 165(1-4), 70-80. doi:10.1093/rpd/ncv116
- Vuolo, J. (2002). *Fundamentos da teoria de erros*. (2<sup>nd</sup> ed.): Edgard Blücher Ltda.
- Winslow, J. F., Hyer, D. E., Fisher, R. F., Tien, C. J., & Hintenlang, D. E. (2009). Construction of anthropomorphic phantoms for use in dosimetry studies. *Journal of Applied Clinical Medical Physics*, 10(3).
- World Health Organization, & IAEA. (2013). Bonn call-for-action: joint position statement by IAEA and WHO. In. Geneva: World Health Organization.
- Xu, X. G., & Eckerman, K. F. (2009). *Handbook of anatomical models for radiation dosimetry*: Taylor & Francis.
- Yoshimura, E. M., & Yukihiro, E. G. (2006). Optically stimulated luminescence: searching for new dosimetric materials. *Nuclear Instruments and Methods in Physics Research Section B: Beam Interactions with Materials and Atoms*, 250(1), 337-341. doi:10.1016/j.nimb.2006.04.134
- Yukihiro, E. G., & McKeever, S. W. S. (2008). Optically stimulated luminescence (OSL) dosimetry in medicine. *Physics in Medicine and Biology*, 53(20), R351-379. doi:10.1088/0031-9155/53/20/R01
- Yukihiro, E. G., & McKeever, S. W. S. (2011). *Optically stimulated luminescence: fundamentals and applications*: John Wiley & Sons.
- Yukihiro, E. G., McKeever, S. W. S., & Akselrod, M. S. (2014). State of art: Optically stimulated luminescence dosimetry – Frontiers of future research. *Radiation Measurements*, 71, 15-24. doi:10.1016/j.radmeas.2014.03.023
- Zhang, D., Li, X. H., Gao, Y. M., Xu, X. G., & Liu, B. (2013). A method to acquire CT organ dose map using OSL dosimeters and ATOM anthropomorphic phantoms. *Medical Physics*, 40(8), 9. doi:10.1118/1.4816299

## APPENDIX A

This section describes the determination of the uncertainties associated with  $f_i$  determined for the lungs of the CIRS ATOM.

Consider  $f_i = \frac{V_i}{V_T}$ , where  $V_i$  is the volume of the lungs inside slice  $i$  and  $V_T$  is the total volume of the lungs, determined as  $V_T = \sum_{i=9}^{15} V_i$ . In addition, as described in Section 3.2.3, each physical slice  $i$  of the phantom corresponded to 20 CT images. In those images,  $p$  is the length of the pixel in millimeters and  $t$  is the thickness of the CT image. In this study,  $p = 0.6465 \text{ mm}$  and  $t = 1.3 \text{ mm}$ . Uncertainties on these quantities are 1.1% for  $p$  and 4% for  $t$ . The volume of the lungs per physical slice of the phantom is calculated as demonstrated in Section 3.2.3. The uncertainty on these values were determined by propagation of the uncertainties due to  $p$ ,  $t$  and  $A_i$ , which was visually determined and was related to the pixels of the border between lung tissue and other tissues.

However, since the total volume of the lungs is given by the sum over all individual slice volumes, uncertainties on values of  $f_i$  were propagated and included a co-variance term (Vuolo, 2002). Therefore, Equation A.1 describes the uncertainties of  $f_i$ :

$$\frac{\sigma_{f_i}^2}{f_i^2} = \left(\frac{\sigma_{V_i}}{V_i}\right)^2 + \left(\frac{\sigma_{V_T}}{V_T}\right)^2 - \frac{2\sigma_{V_i}\sigma_{V_T}}{V_i V_T} \quad (\text{A.1})$$

## APPENDIX B

### THE IAEA COORDINATED RESEARCH PROJECT (CRP) ON “EVALUATION AND OPTIMIZATION OF PEDIATRIC IMAGING” (E2.40.20)

The International Atomic Energy Agency’s (IAEA’s) Coordinated Research Activities aim to join scientists from developing and developed countries to exchange knowledge and ideas for their mutual benefit. Most of these activities are accomplished with the Coordinated Research Projects (CRPs), which put together about 15 medical and scientific institutes from all over the world to focus on common interest issues (IAEA, 2013). The present Master degree research project is part of the IAEA Coordinated Research Project (CRP) on “Evaluation and Optimization of Pediatric Imaging” (E2.40.20) under contract 19047. The main goal is to reduce the radiation exposure on children by optimizing standard protocols and applying advanced image processing techniques and imaging systems.

The present CRP has been developed in a partnership between the Radiation Dosimetry and Medical Physics Group of the Institute of Physics of the University of São Paulo (IFUSP) and the Institute of Radiology of the School of Medicine of the University of São Paulo (InRad/FMUSP). A group of IFUSP professionals has been performing the quality assurance (QA) and quality control (QC) at InRad since 2001. All the procedures are performed according to the methods proposed by the IAEA (2014).<sup>m</sup>

#### *1. Objectives and Activities*

The following diagnostic modalities have been studied in the present project: radiography, fluoroscopy and computed tomography. The objectives related to CT procedures were developed in this Master’s project and are listed below.

- Data collection of thorax and head CT procedures applied in pediatric patients, considering four age ranges: 0-1 year old, 1-5 years old, 5-10 years old and 10-16 years old, in the CT equipment of InRad/FMUSP, using the Picture Archiving and Communication System/Radiology Information System (PACS/RIS) data and DICOM header information.

---

<sup>m</sup> The execution of the present project was previously authorized by the ethical committee of the Institute of Radiology of the School of Medicine of the University of São Paulo. This institution provides the researchers with the access to clinical examinations and patient data, which are maintained confidential.

- Quantitative and qualitative evaluation of patient and protocol data collected per age range
- Evaluation of lung doses due to the standard CT procedures applied to pediatric patients at InRad/FMUSP.

Data collection was performed for two of the five CT equipment available in the Institution. Most of the pediatric thorax CT exams were performed in a Philips Brilliance 64 dedicated for routine examinations while most of the pediatric head CT exams were performed in a Philips Brilliance 64 dedicated for emergency. The relevant information from the DICOM header of the images was extracted using a computer routine in Matlab®2015 (Mathworks, Co).

A quantitative and qualitative evaluation of the patient data collected in each age range was performed. However, some aspects of these data acquisition have to be highlighted. The first one is the fact that part of the cohort has no information concerning the CTDI and the DLP, since the dose report was not recorded after the examination. It was a common issue especially for Thorax CT patients, in which about 50% of data collected did not present dose report. Another aspect is that since the partner hospital is not a pediatric hospital, there is a small number of pediatric patients performing thorax CT per year, even though this is the 5<sup>th</sup> most applied protocol. In 2015, as previously mentioned, about 170 pediatric patients from the 3,300 pediatric patients in that institution performed thorax CT, including all age ranges and five CT equipment. As a consequence, this examination requires prospective data to improve the analysis.

Another important result emerging from this analysis is related to the tube voltage applied in the examinations. From the 80 patients analyzed for Head CT examinations, only one procedure was performed with 80 kV. Similarly, from the 58 patients analyzed for Thorax CT examinations, one procedure was performed with 80 kV. However, with the advent of modern reconstruction techniques, children with less than 50 kg can be scanned with 80 kV and children up to 80 kg can be scanned with 100 kV (Lira, Padole, Kalra, & Singh, 2015) with no loss in image quality. Many authors state that reducing tube voltage is an efficient way of reducing radiation dose in children with no significant loss in diagnostic information (IAEA, 2014; Lira et al., 2015).

## APPENDIX C

Several statistical tests were performed to show that the distribution of dosimeter responses follow approximately a Normal distribution. All the tests were performed with the software Wolfram Mathematica® 10.0 and some of them are described below.

The first test performed was a graphical test, so-called a Q-Q plot (Chambers, 1983). This tool is a plot of quantiles of some data against the quantiles of a certain statistical distribution. In the present work the purpose was to compare the distribution of the dosimeter responses data to a theoretical Normal distribution. To do so, the 452 dosimeter responses were plotted against a Normal distribution with the same mean and standard deviation of the responses. The Normal distribution is plotted as dashed lines and the experimental data are plotted as dots. If the dots follow the dashed lines, it means the data is Normally distributed (Figure C.1).

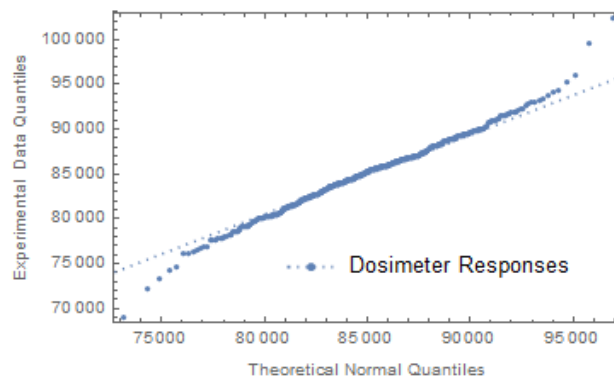


Figure C. 1 – Left: Q-Q Plot to compare the distribution of the OSLD responses to a theoretical Normal distribution with mean and standard deviation equal of the responses. The linearity of the dots suggests that the data is Normally distributed. Right: Q-Q Plot to compare the distribution of 452 simulated data to a theoretical Normal distribution.

The responses were tested against a Normal distribution with mean and standard deviation of the OSL responses ( $85021 \pm 4018$ ). Significance level ( $\alpha$ ) considered was 5% ( $\alpha = 0.05$ ), the null hypothesis ( $H_0$ ) is that the responses follow a Normal distribution and this hypothesis is rejected if the *p-value* of the statistic test is smaller than the significance level ( $p < \alpha$ ). As an example, the *p-value* obtained for four statistical tests are presented in Table C. 1.

Table C. 1 - Statistical tests and p-values obtained to verify the null hypothesis that the dosimeter responses follow a Normal distribution.

<b>Statistical test</b>	<b><i>p-value</i></b>
Anderson-Darling	0.47
Cramér-von Mises	0.42
Mardia Skewness	0.89
Pearson $\chi^2$	0.61

The results presented in Table C. 1 indicate that the null hypothesis that the data is distributed according to a Normal distribution with mean 85021 and standard deviation 4018 at the 5% level is not rejected.

## APPENDIX D

Data used to assess reproducibility and reusability of the three dosimeter Groups.

Measured OSL signal (counts/s)													
Group 1							Group 2						
Measurement	1	2	3	4	Mean	CV of four measurements	Measurement	1	2	3	4	Mean	CV of four measurements
<b>Dosimeter 1</b>	29527	29351	30062	29229	29542	1%	<b>Dosimeter 1</b>	29037	28365	30382	27446	28808	4%
<b>Dosimeter 2</b>	30373	29154	29782	28759	29517	2%	<b>Dosimeter 2</b>	29776	29229	28842	28874	29180	1%
<b>Dosimeter 3</b>	27925	26288	25992	25781	26497	4%	<b>Dosimeter 3</b>	31537	31605	31767	31132	31510	1%
<b>Dosimeter 4</b>	29196	28716	29326	28915	29038	1%	<b>Dosimeter 4</b>	31622	30946	30543	30386	30874	2%
<b>Dosimeter 5</b>	30687	30488	30712	29683	30393	2%	<b>Dosimeter 5</b>	31485	31034	30256	31358	31033	2%
<b>Dosimeter 6</b>	29614	28644	28910	28539	28927	2%	<b>Dosimeter 6</b>	30346	30268	29275	29667	29889	2%
<b>Dosimeter 7</b>	31880	30087	30044	30351	30591	3%	<b>Dosimeter 7</b>	29975	29385	29005	29867	29558	2%
<b>Dosimeter 8</b>	30625	29641	30086	29443	29949	2%	<b>Dosimeter 8</b>	30443	29603	29816	29606	29867	1%
<b>Dosimeter 9</b>	31583	31391	33727	30974	31919	4%	<b>Dosimeter 9</b>	33259	31511	31892	31340	32001	3%
<b>Dosimeter 10</b>	28994	29306	29646	29172	29280	1%	<b>Dosimeter 10</b>	31111	31010	29990	30656	30692	2%
<b>Dosimeter 11</b>	31680	30389	31592	30444	31026	2%	<b>Dosimeter 11</b>	29528	29251	28931	29022	29183	1%
<b>Dosimeter 12</b>	31729	30744	31237	30992	31176	1%	<b>Dosimeter 12</b>	31878	30905	30076	29588	30612	3%
<b>Dosimeter 13</b>	31271	30325	31441	30686	30931	2%	<b>Dosimeter 13</b>	31403	31106	29483	29877	30467	3%
<b>Dosimeter 14</b>	31632	30540	30964	30546	30921	2%	<b>Dosimeter 14</b>	31178	30259	29959	30026	30356	2%
<b>Dosimeter 15</b>	31901	31145	31273	30804	31281	1%	<b>Dosimeter 15</b>	29804	29149	28295	28551	28950	2%
<b>Dosimeter 16</b>	30950	30880	31141	30825	30949	0%	<b>Dosimeter 16</b>	25855	25747	25276	25475	25588	1%
<b>Dosimeter 17</b>	31126	30614	31073	30674	30872	1%	<b>Dosimeter 17</b>	30189	29701	29619	29947	29864	1%
<b>Dosimeter 18</b>	31416	31104	30926	30903	31087	1%	<b>Dosimeter 18</b>	30127	30070	29746	29716	29915	1%
<b>Dosimeter 19</b>	31350	30470	31143	30966	30982	1%	<b>Dosimeter 19</b>	29448	29619	31800	31268	30534	4%
<b>Dosimeter 20</b>	31496	31324	31301	30577	31175	1%	<b>Dosimeter 20</b>	29986	29697	31785	31238	30677	3%
<b>Dosimeter 21</b>	31482	30900	31362	30969	31178	1%	<b>Dosimeter 21</b>	30063	30405	29724	29788	29995	1%
<b>Dosimeter 22</b>	30282	29855	30200	29457	29949	1%							
<b>Dosimeter 23</b>	31309	31618	31659	30947	31383	1%							
<b>CV of 23 dosimeters</b>	3%	4%	5%	4%			<b>CV of 21 dosimeters</b>	5%	4%	5%	4%		

Normalized OSL signal						
Group 3						
Measurement	1	2	3	4	Mean	CV of four measurements
<b>Dosimeter 1</b>	2.338	2.317	2.345	2.356	2.339	1%
<b>Dosimeter 2</b>	2.432	2.452	2.432	2.307	2.406	3%
<b>Dosimeter 3</b>	2.417	2.417	2.400	2.419	2.413	0%
<b>Dosimeter 4</b>	2.430	2.331	2.408	2.367	2.384	2%
<b>Dosimeter 5</b>	2.420	2.373	2.360	2.434	2.397	1%
<b>Dosimeter 6</b>	2.427	2.370	2.394	2.412	2.401	1%
<b>Dosimeter 7</b>	2.396	2.387	2.358	2.400	2.385	1%
<b>Dosimeter 8</b>	2.402	2.376	2.425	2.389	2.398	1%
<b>Dosimeter 9</b>	2.400	2.365	2.448	2.359	2.393	2%
<b>Dosimeter 10</b>	2.430	2.440	2.370	2.346	2.396	2%
<b>Dosimeter 11</b>	2.393	2.374	2.349	2.278	2.349	2%
<b>Dosimeter 12</b>	2.398	2.431	2.357	2.376	2.391	1%
<b>Dosimeter 13</b>	2.377	2.437	2.369	2.411	2.398	1%
<b>Dosimeter 14</b>	2.337	2.498	2.404	2.368	2.402	3%
<b>Dosimeter 15</b>	2.374	2.359	2.400	2.361	2.373	1%
<b>Dosimeter 16</b>	2.359	2.472	2.415	2.398	2.411	2%
<b>Dosimeter 17</b>	2.345	2.382	2.443	2.417	2.397	2%
<b>Dosimeter 18</b>	2.427	2.383	2.414	2.295	2.380	3%
<b>Dosimeter 19</b>	2.351	2.396	2.415	2.323	2.371	2%
<b>Dosimeter 20</b>	2.411	2.427	2.376	2.348	2.390	1%
<b>Dosimeter 21</b>	2.359	2.396	2.338	2.368	2.365	1%
<b>Dosimeter 22</b>	2.316	2.422	2.434	2.349	2.380	2%
<b>Dosimeter 23</b>	2.292	2.407	2.343	2.353	2.349	2%
<b>CV of 23 dosimeters</b>	2%	2%	1%	2%		